Vortex bursting near a free surface

Promode R. Bandyopadhyay†

Naval Undersea Warfare Center, Newport, RI 02841, USA

When the cross-section is reduced, a vortex displays spiralling and elasticity, bursting when the external velocity drops. How are these properties affected near a free surface? To answer, a visualization experiment in water is considered where an oscillating obstruction is pitched orthogonally to a rolling oscillation expending minimum energy. We show that short aerated vortices in adverse pressure gradient and shear remain stable during stretching, bursting into bubbles when relaxed after maximum stretching. A vertical aerated double helix (DH) root vortex of contra-rotating vortex tubes is produced near a Rossby number of 0.20. The vortex approaches an inclination of 45° to the vertical, where stretching intensifies the vorticity to the maximum extent. Vortex inclinations up to 45° are stable and unstable thereafter. Vortex bursting commences only when the inclination crosses 45° by the slightest amount. When relaxed, oscillations are produced, breaking the vortex into arrays of bubbles, sometimes precisely at 45° inclination. The bubble diameter, modelled by equating the effects of the centrifugal force (CF) on the vortex core pressure, to surface tension scales with the inverse of the square of the rotational velocity. When a high CF is withdrawn, the bursting DH aerated vortex cone is crushed due to surface tension. A root vortex and a coiled-up trailing edge vortex together form a compact Hill's vortex when the highest CF is relieved, bursting into bubbles spectacularly scattered in the unstable sector. The DH vortex breakup is the connection point of vortices in proximity. At high CF, the DH has stacks of Taylor air tubes at 45° to the external flow bursting when relaxed. Kelvin waves abound when bursting.

Key words: vortex breakdown, capillary waves, elastic waves

---

1. Introduction

Rotating flows are fundamentally important in fluid mechanics because of their wide prevalence – from turbomachinery to planetary systems. Commonly, an isolated single vortex is studied. Compelling spiralling effects emerge when the cross-section of the vortex narrows. Due to their elasticity, functioning here as a restoring mechanism, a vortex can sustain waves. When the external velocity falls below a certain level, a catastrophic increase in the vortex diameter occurs, a phenomenon known as vortex breakdown or bursting (Batchelor 1967). Given the effect of such bursting on the

† Present address: 153 Chases Ln., Middletown, RI 02842, USA. Email address for correspondence: promode.r.bandyopadhyay@gmail.com

stability of delta-wing aircraft, they have been extensively studied (Werle 1984). The literature on bursting is extensive and a summary is given in the next subsection. Instead, we consider a special new case of the bursting of an aerated vortex near a free surface that exhibits a range of impressive properties not previously reported. The vortex experiment simulates the air–sea interaction affecting the exchange of thermal energy.

Considerations of an irrotational line vortex and experience show that in the vortices shed from the side edges of the delta wings of an aircraft, changes in the structure may occur when $2\Omega a/U_1 = 1$ if the external field is decelerated. Here, Ω is the rigid body angular velocity, a is the vortex radius and U_1 is the axial velocity of the vortex (Batchelor 1967, p. 553). The vortex whose bursting is the subject of the present work is formed at the sharp trailing edge of a foil and the above bursting criterion may apply.

By using a nearly self-regulating periodic foil obstruction near a free surface, a short-length vortex is produced in a water tank. The vortex bursts in every cycle when the obstruction is relieved. To clarify, the root vortex formed does not rotate freely. The capillary-scale aerated tubes formed out of the free surface waves curving into the funnel while also drawing in air, and the double helix (DH) contra-rotating vortex tubes formed at the trailing edge root, are all twisted together like a torsional spring over a duration of 1/4th the time period of oscillation at both 1 Hz and 1.25 Hz, into what we have called the root vortex. All aerated tubes are stretched during this time. After that, the input pitch torque is withdrawn, relaxing the tubes, when the vortex bursts into bubbles. We examine the conditions of bursting and bubble formation.

To understand the coiling and uncoiling of the aerated root vortex described above, we draw an analogy between the spatio-temporal vorticity form of the compressible Navier–Stokes equation and the temporal equation of vibration of a vertical mechanical system such as a spring, mass and damper system. Consider the compressible vorticity equation without any external body force written as

$$\nabla^2\omega - (1/\nu)(u \cdot \nabla)\omega + (1/\nu)(\omega \cdot \nabla)u = -(1/(\nu\rho^2))\nabla\rho \times \nabla p + (1/\nu)\partial\omega/\partial t. \quad (1.1)$$

Here, ω is the vorticity, p is the pressure, ρ is the density and ν is the kinematic viscosity. The vibration equation is given by

$$m\ddot{x} + C\dot{x} + kx = mg + F(t), \quad (1.2)$$

where the dots represent the time derivatives, m is the mass, x is the vertical displacement about a neutral position, C is the damping constant, k is the spring constant, g is the acceleration due to gravity, t is the time and $F(t)$ is an external force perturbation to the mass applied in the vertical direction. The vorticity equation may be directly compared with the vibration equation because the forms are similar. The negative pressure–density compressibility term on the right-hand side of the vorticity equation is a buoyancy effect and is similar to the mg term in the vibration equation. The negative term on the left-hand side is a damping term and the third term includes the spring constant. The last term is similar to $F(t)$. The vorticity equation is also a vibration equation and the formation of resonant coiled aerated vortex structures with spring-like properties should be expected. Supporting the analogy, the efficient flapping foil force of hovering has five Fourier coefficients (Beal & Bandyopadhyay 2007) and the damped natural oscillation of an unloaded low-friction foil in a hemispherical motor apparatus also has five peaks (Bandyopadhyay 2019).

Suddenly vanishing inertia forces and spatial variations in an aerated vortex after maximum vorticity stretching give

$$\partial\omega/\partial t = (1/(\rho^2))\nabla\rho \times \nabla p, \tag{1.3}$$

where viscosity ν is absent. The ensuing violent oscillations in ω of the vortex tubes can cause disintegration into bubbles scattering far and wide when greater elastic energy represented by the cross-product is compressed in with increasing centrifugal forces. This hypothesis of vortex bursting mechanism is explored here.

Physically separated from the DH of contra-rotating vortex tubes at the root near the surface, co-rotating vortex tubes spiral around one other in the rolled up foil-tip boundary layer in the area deeper below. Both co- and contra-rotating vortex tubes grow and burst in adverse pressure gradients. Their bursting mechanism is compared for independent verification.

The wave oscillation frequency of $f = 1$ Hz, imparted by a single flapping foil (figure 1), is the lowest frequency when the root vortices first form. Using six of such flapping foils, we have built underwater platforms with precision manoeuvrability (Menozzi *et al.* 2008; Bandyopadhyay 2016). Using six of our foils underwater, we could lift a bunch of washers (weighing 100 g in air) in steps of 10 cm from the floor (Bandyopadhyay *et al.* 2011). What this means is, the six foils could introduce orthogonal waves in increments of 0.25 N. The development of initial condition dependence in the lateral direction is restricted in the apparatus reducing the number of dimensions and improving flow stability. In water, for aerated vortices, gravity functions as a restoring force. Because the foil pitch bias angle $\theta_{bias} = 0°$ (see equations in § 2.1), the dimension in yaw is zero. Both parametric measurements and downhill simplex methodology have led to the convergence in the hydrodynamic efficiency. Measurements have shown that the foil parameters can produce thrust close to zero in some phase of the oscillation, but do not produce drag at any instant of time (figure 8 in Bandyopadhyay 2015). The energy consumption is therefore minimal (Bandyopadhyay, Beal & Menozzi 2008*a*). Hence, the flow parameters are limiting in chaos, energy consumption and force production, and yet the transitional aerated vortices are produced. The apparatus produces an energy-optimized case of orthogonal wave–wave interaction.

The stability of an aerated vortex near a free surface, when the input torque is minimal and the stretching is a maximum, is visualized. The aerated vortex lies near the free surface. It entrains air from the atmosphere. The curved air–water interface of the core is sharp and acts as a mirror, helping visualization. We explore the successive stages of bursting in the aerated root vortex, in the air-jacketed foil boundary layer and in the rolled-up vorticity of the foil-tip flow. The bursting mechanisms are examined in the context of Saffman's (1990) modelling of vortex breaking and the cavitation visualization by Tsoy *et al.* (2018) of the Kelvin modes in a long slender vortex tube in a swirling diffuser flow. We examine the relationship of stretching and sudden relaxation of aerated tubes to bubble formation. The conditions of vortex bursting are sought. The organized motions are identified. They are also presented in Movies 1 to 4 available at https://doi.org/10.1017/jfm.2019.1075 and listed in table 1.

1.1. *Literature*

Vortex bursting was discovered by Peckham & Atkinson (1957). The early understanding of vortex bursting was based on visual observations which lacked measurements. Analysis had insufficient treatment of the wave properties. In present
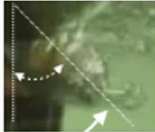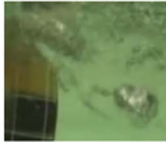
P. R. Bandyopadhyay
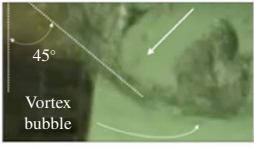
Aerated vortex organization and waves		Aerated large root vortex, vortex breaking and jetting	
	Double helix aerated vortex vorticity has cancelled where the double helix arms of opposite vorticity cross $f = 1$ Hz		Aerated vortex cone with horizontal swirling jet at apex angle shown is $45°$ $f = 1$ Hz
	Double helix root vortex $f = 1$ Hz		Vortex breaking $f = 1$ Hz
	Double helix root vortex $f = 1$ Hz		Reconnected vortex $f = 1$ Hz
	Double helix root vortex: cylindrical and conical $f = 1.25$ Hz		Twisting Taylor air tubes at $45°$; abrupt reductions in vortex diameter: Kelvin mode $m = 0$ $f = 1.25$ Hz
	Vortex spiral in foil tip single Kelvin wave: $m = 1$ $f = 1.25$ Hz		Root vortex with Taylor air tubes $f = 1.25$ Hz
	Aerated vortex cone Kelvin mode $m = 1$ $f = 1$ Hz		Vortex rod: Aerated swirling jet of uniform diameter $f = 1$ Hz
	Aerated vortex congregation at breakup point along axes of maximum stretching		

TABLE 1. Summary of the organized aerated vortex motions of the root vortex and those at the rolled up foil-tip flow. They represent the uniform and conical vorticity spirals of pitch f of Kelvin mode $m = 1$, retarded compared to upstream.
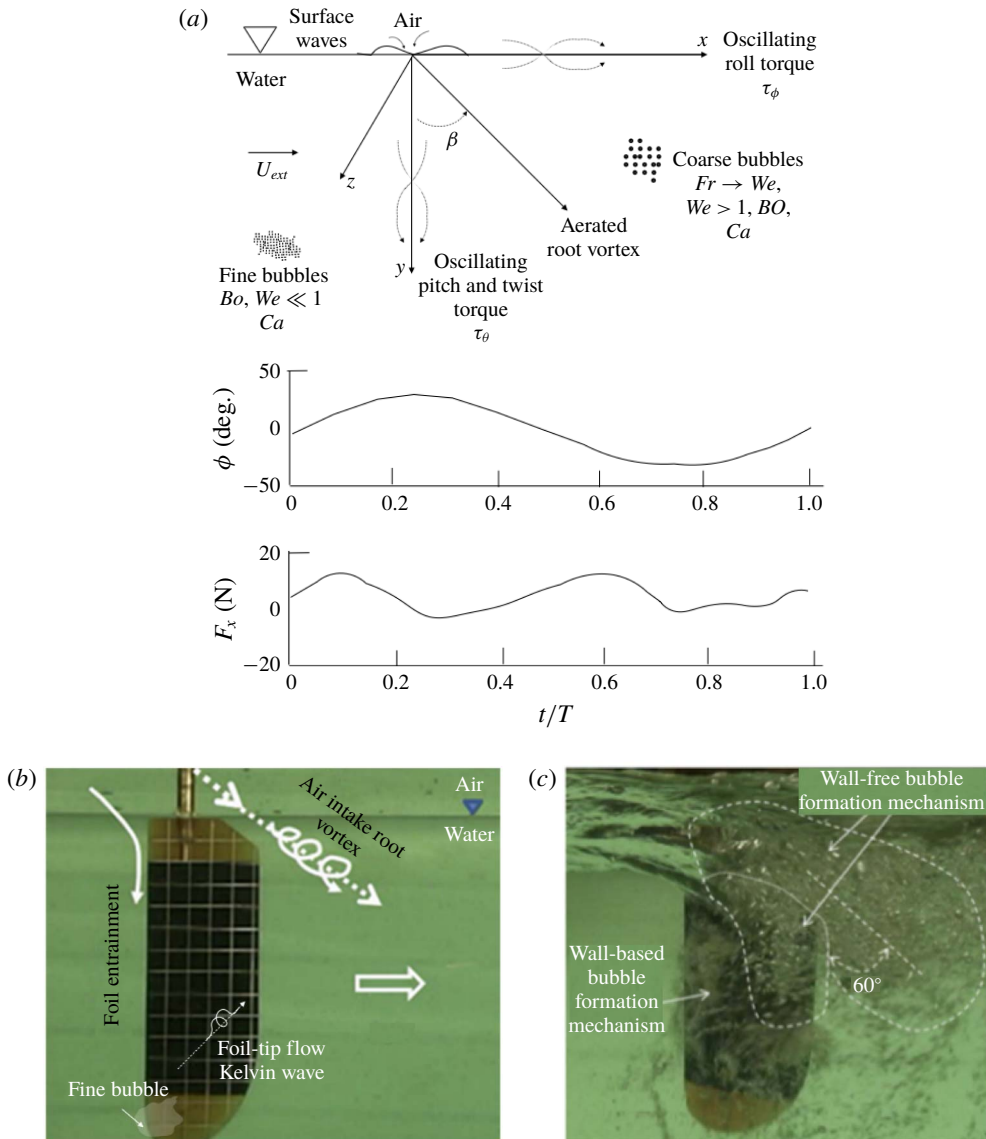
FIGURE 1. For caption see next page.

days, theories and direct numerical and large eddy simulations provide details of the instability and the vortex structures. However, in aerated vortex flows, surface tension, pressure effects and a fine-bubble-scale grid resolution of the air–water interface are required. These improvements would reveal the mechanisms of how the maximal stretching of an aerated vortex tube leads to the formation of bubbles when relieved and produces the acoustic radiation from the vibrating air–water interfaces. The simulation of the formation of fine bubbles near a solid surface boundary layer remains the most challenging due to the high order of nonlinear effects which require an extraordinary numerical accuracy in the calculations of the interacting gradients. In a significant progress of visualization techniques, Tricoche *et al.* (2004) have given a numerical parametric topology tracking method for identifying the streamlines and

FIGURE 1. (cntd). Wave interaction apparatus and surface condition of first oscillation cycle: definition sketch (*a* top); time trace of roll angle (ϕ) and force (F_x) in the forward direction (*a* bottom); photograph of foil in water (*b*) with foil root at water surface level; image (*c*) of distinct, autonomous formation of coarse and fine bubbles after vortex has burst; (*d,e*) radiating capillary waves (*d*, inset is enlarged view) growing into standing waves in the funnel (*e*) during the first foil oscillation cycle when foil pitching has been added to rolling. The sketch in (*a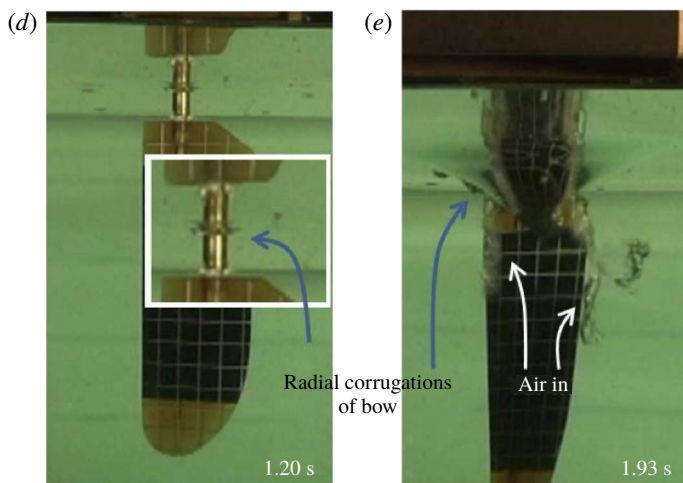* top) defines the oscillatory roll torque (amplitude τ_{ϕ_o}), sum of oscillating pitch and twist torque amplitudes (τ_{θ_o}), induced flow amplitude ($\tau_{\phi_o} \times \tau_{\theta_o}$), air intake vortex torque amplitude (($\cos \phi_o \sin \theta_o)(\tau_{\phi_o} \times \tau_{\theta_o})$), coarse bubbles where ($Fr \to We$; Bo; $We > 1$), foil capillary effects (fine bubbles) where ($Ca \sim 1$; Bo), $We \ll 1$; see text for symbols.

iso-surfaces in the interior of the seemingly cluttered region of a burst vortex. This work brings rigour to the strength of the intuitive context of visualization.

Due to its relevance in finiteness and end effects, it is useful to consider the behaviour of a vortex in a tornado chamber (Trapp 2000). The free surface in the present work can be treated like a wall. This is equivalent to the Earth's surface in the case of a tornado analogy. The transition of a vortex flow from laminar to turbulent can be delineated by the swirl ratio S which is the ratio of the azimuthal (V_θ) to the axial (V_a) velocity. Rossby number Ro is defined as $Ro = U_{ext}/V_{\theta max}$, the ratio of the external (U_{ext}) to the maximum azimuthal ($V_{\theta max}$) velocities. For low values of S, a laminar single celled vortex is formed that has air passing through it. At moderate values of S, the vortex becomes intense, as well as turbulent and the air flow becomes a jet originating at the boundary. The jet terminates at a stagnation point beyond which the vortex suddenly expands. With further increase in S the vortex breakdown point moves earlier.

Early reviews of the theory of vortex breakdown, primarily in the context of aerodynamics, appear in Benjamin (1962), Hill (1977), Leibovich (1978, 1984) and Lugt (1989). They introduced the mechanism of a vortex supporting critical centrifugal waves. A supercritical condition is reached since the jet velocity can be $\geqslant 3$ times the axial velocity outside the core. As a result, centrifugal waves cannot travel upstream. After the breakdown, the velocity is subcritical and waves can travel both up and downstream. For breakdown, the vortex needs to be supercritical and the swirl ratio S should be moderate to high. The supercritical condition (the formation of

an axial jet) can be achieved by the boundary layer where due to friction centrifugal force is reduced, but the force of radial pressure gradient remains the same. The imbalance causes a strong inflow towards the vortex axis which eventually turns axial in order to satisfy continuity. Saffman (1990) refined these models later in terms of vortex breaking. The present work gives evidence of the critical role played by the vortex breaking. It also shows the presence of Kelvin instabilities filling the time gap between the vortex breaking and the initiation of the terminal bursting.

In a cyclonic gas–liquid separator that controls the centrifugal forces near the boundary layers of the end walls, the vortex with the separated gas core has been found to transition from a straight to a spiralling configuration depending on the aspect ratio of the cylinder (the ratio of the length to the diameter) and the swirl velocity (Bandyopadhyay & Gad-El-Hak 1996).

Marine propeller blades are highly skewed to lower the cavitation induced vibration. However, they also produce tip vortex cavitation which implodes and rebounds causing two high amplitude high frequency pressure fluctuations and stern vibration. The tip vortex can burst if the momentum deficit of the blade wake is high enough. The tip vortex cavitation is found to burst when the time derivative of the vortex strength exceeds a certain level (Konno *et al.* 2002).

Recent videography of the underside of plunging breaking waves show how air is entrained via tornado-like vortical tubes that wrap around the wave (the spanwise tube of air). High resolution numerical simulation has vividly reproduced these longitudinal arrays of secondary vortex structures (Lubin & Glockner 2015). Surface tension and the history effects of previous plunging waves are so far not included. The mouth of the vortex is open to the surface and the other end is open to the tube. The shear in the saddle region stretches the aerated vortex structures. The streamwise vortex structures have an upstream slant of $50°$. This slope is very close to the direction of principal strain, namely $45°$. These arrays of aerated secondary vortex structures bear some similarity to the Taylor air tubes of the present work.

Near a free surface, small bubbles bursting produce high-speed liquid jets which subsequently break up producing droplets (Boulton-Stone & Blake 1993). The bursting of secondary air tubes in plunging waves has been photographed (Kway, Lo & Chan 1998).

Vortex breakdown has been ascribed to the genesis of tornadoes and waterspouts near the ground in the mid-section of the funnel near the parent cloud (Lugt 1989). In a mesocyclone, whether such observations pertain to vortex breakdown has been debated although a vertical adverse pressure gradient is present and the mesocyclone vortex is susceptible to instability. Numerically, the phenomenon is attributed to the formation of a two-celled vortex, but in the absence of a vortex breakdown This circumstance is due to the boundary layer vorticity tilting effects whereby the low level vertical vorticity exceeds that at the mid-level. Therefore, the claim of vortex breakdown in a mesocyclone is not well founded, indicating the need for caution and further work (Trapp 2000).

Considering the vast gallery of visualizations of spiralling vortex flow bursting in Sarpkaya (1971), Faler & Leibovich (1977), Phillips (1985), Pauley & Snow (1988), Khoo *et al.* (1997), Fiedler (2009), Nolan (2012), Smits & Lim (2012) and Rotunno (2013), we conclude that the visualization of the winding and unwinding of aerated double helix vortices, and of their bursting into bubbles, particularly where the two arms have opposite sense of rotation, has not yet been carried out. The aerated vortex flows summarized in table 1 do not appear in any of these citations, making them newly found.

Rotunno ([2013](#)) concludes by pointing out that vortex bursting in a chamber and in a numerical box are sensitive to boundary effects which, however, are of secondary importance in natural mesocyclones; the effects of a cool air boundary is also ignored. For these reasons of boundary effects and the presence of multi-phase, it is useful to separate vortex flows and their bursting in oceanography, delta wing aerodynamics, natural mesocyclones and those in a pipe or chamber.

Vortex flows in a chamber simulate natural mesoscale cyclones perhaps superficially (Rotunno [2013](#)), and have sometimes been optimistically called unconfined (Khoo *et al.* [1997](#)), and yet both Reynolds number Re $(Re = V_o r_o / \nu = \Gamma / (2\pi\nu))$ and swirl number S $(S = r_o \Gamma / Q)$ have been defined in terms of the chamber radius r_o and Q, the volume flow rate in the chamber; here, Γ is circulation and ν is kinematic viscosity.

To understand the strong effects of the boundaries in vortex flows, consider these examples. The aerated double helix in the present work is contra-rotating; and the conical vortices cone down with depth but in all other examples they flare out downstream. The aerated contra-rotating double helix in the present work originates from the realignment of the vorticity of the same horseshoe vortex ahead of the foil stem – an obstacle – and not due to the instability of the inner circulation as in 'tornados' (Nolan [2012](#)). Due to the presence of the free surface, the large effects of the pressure–density compressibility term in the vorticity equation ([1.1](#)) in the present aerated vortices is the most important difference compared to the non-aerated vortices reported earlier.

Unlike in most studies on vortex bursting, the present aerated vortices burst and produce bubbles. When the inertia forces and spatial variations are suddenly brought to zero in an aerated vortex after maximum stretching at $\beta = 45°$, the left-hand terms in ([1.1](#)) vanish, giving equation ([1.3](#)). Viscosity ν is no longer important. If centrifugal forces increase, the pressure density cross-product will multiply causing greater violent oscillations of vorticity ω in the vortex tubes. The entire tube would oscillate and disintegration into spectacular bubble scattering can occur. These expectations are met in the present work but not in the vortices that are not aerated.

In Nolan ([2012](#)), Rotunno ([2013](#)) and Fiedler ([2009](#)), several co-rotating and non-aerated vortices first form as disparate satellites, not generated as a double helix, which then interact to spiral together as double or multi-helix, but they do not burst. The viscous core can become unstable and generate multiple vortices wrapping together (Nolan [2012](#)).

Phillips ([1985](#)) has reported the visualization of the 'massive disruption' of unaerated single and double helices, whose rotational sense can match or oppose that of the outer flow. His flow parameters are transitional: Re of <750 and $1.5 < S < 3$. His figure 5 shows evidence of the external introduction of vorticity perturbations from two oppositely located dye ports. We tentatively suggest that, similar to figures 5 and 17 in Rotunno ([2013](#)), satellite single vortices from the dye ports are wrapping around each other about the stagnation point of the burst region; the signs of the vortices are unknown. The boundary effects in the present work are grossly different from other studies cited and differences between the aerated versus non-aerated vortex flows and bursting into bubbles should be expected.

The vortex breakdown literature relevant to combustion of 1955–2000 has been reviewed with a primary focus on bubble-type breakdown (Luca-Negro & O'Doherty [2001](#)) (not to be confused with air bubbles in water). The measurements and numerical simulation results which have become available only recently show some degree of maturity of the subject.

Direct numerical and large eddy simulations have shown that if a vortex core radius increases locally, a pressure wave is initiated, which travels along the vortex axis to the region where the radius is lower. Behind the wave, the axial velocity increases so that sufficient swirl triggers a helical instability. When such pressure waves intersect, the structure of the vortex core abruptly changes (Moet *et al.* 2005). This is known as vortex bursting. In the present work these results bear relevance to the foil-tip flow.

In order to enhance lift forces, delta wings are used as leading edge extensions in fighter aircraft. In common Reynolds numbers (*Re*), bursting of the leading edge vortex is of the spiralling type and not of the bubble type as in the confines of pipe flows. Vortex bursting is sometimes treated as a hydraulic jump. The core of the leading edge vortex acts as a waveguide where the inflow longitudinal waves can amplify to a critical spiral and burst. A continuously unsteady pitching up or down delta wing can have significant hysteretic effects on the leading edge suction lift (meaning more increase or decrease). This effect is due to the delayed or leading movements of the vortex burst axial location compared to those of the steady levels in the angle of attack (Heron & Myose 2009).

Axisymmetric vortex bursting has been attributed to the development of a negative component of azimuthal vorticity due to the stretching and tilting of the axial vorticity (Brown & Lopez 1990). Visual evidence from the present work will re-examine this statement more directly by invoking Batchelor's (1967) vortex analysis in a pressure gradient.

A vortex with a helical core tumbles, that is, it translates while rotating slowly (Joukowsky 1912; Fuentes 2018). The velocity field in a helical vortex is composed of three parts: first, due to the circulation Γ around the vortex; second, due to its curvature; and third, due to the far off portions of the vortex (Boersma & Wood 1999). The presence of an axial flow turns a rectilinear vortex into a helical vortex which then brings in the latter two components of self-induction. The last component is different compared to that of a ring vortex. In a bathtub vortex starting from a quiescent condition and draining from the bottom of a vessel, the direction of rotation can become altered by the vorticity of the circumferential component of the bottom-wall boundary layer (Sibulkin 1962).

The statistical laws of turbulence may be the properties of specific kinds of elementary coherent vortex structures. The vortices are coherent in the sense that they maintain a given spatio-temporal phase relationship (Bandyopadhyay & Hellum 2014). While various quantitative criteria of coherence have been explored, including enstrophy, some kind of threshold setting is invariably involved due to the closure problem of the Navier–Stokes equations of motion. However, the emphasis should be on phase and not on the amplitude of any variable. With phase emphasized, we want the wave–wave interactions to be central to the dynamics of the vortex bursting which may be a universal process wherever turbulence regeneration is present. In the boundary layer turbulence control over the skins of sharks and dolphins, an external perturbation is imparted primarily to reset the spatio-temporal randomness in phase in the local vorticity environment (Bandyopadhyay & Hellum 2014). In a similarly corresponding manner, when a hand picks up an object, a group of muscles are synchronized in phase, but temporally, by sending an impulse from the inferior olive motion controlling neurons (Kazantsev *et al.* 2004; Bandyopadhyay *et al.* 2008b). The knowledge of the wave properties of helical vortex structures of vortex bursting may have a very broad implication to turbulence control.

Lundgren's (1982) modelling shows that Kolmogorov's $k^{-5/3}$ turbulence energy cascading relationship versus wavenumber k is attributable to the spiralling vortex

structures in an axially straining field. Later, it has been shown experimentally that vortex bursting displays the $k^{-5/3}$ energy cascading relationship (Cuypers, Maurel & Petitjeans 2003). Demonstrating that a unit helical vortex structure is responsible for the fundamental and limiting statistical relationship of turbulence energy cascading, the vortex bursting mechanisms of helical vortex structures are clearly brought into focus.

Ruppert-Felsot, Farge & Petitjeans (2009) have carried out the measurements of the ratio of coherent to non-coherent enstrophies to show that the variable can delineate the three stages of vortex bursting, namely, before, during and after.

Bandyopadhyay, Riester & Ash (1992) have built a trailing vortex apparatus with strong swirl wherein a rotating velocity perturbation, not a mass flow perturbation, could be introduced. A pair of oppositely pitched wings are attached to a small diameter flow aligned cylinder to produce the swirl. The harmonic velocity perturbation device is placed in the boat tail of the cylinder and aft of the wings. The Rossby number of $0.65 \leqslant Ro \leqslant 0.81$, where $Ro = (U_\infty - U_{cl})/V_{\theta max}$ is the ratio of the inertia, measured by the maximum velocity defect, to the Coriolis forces, measured by the maximum azimuthal velocity. Here, U_∞ is the free-stream velocity, U_{cl} is the centreline velocity and $V_{\theta max}$ is the maximum azimuthal velocity. Coarse grids ahead of the model produced $Ro = 0.80$ while fine screens ahead produced $Ro = 0.65$. A lower Ro will promote relaminarization because the restoring effects of the Coriolis force is high when $Ro \ll 1.0$. Considering this result and that of Hopfinger, Browand & Gagne (1982), the value of Ro is estimated to be between 0.20 and 0.65 in the present work, and probably closer to 0.20 since the present flow is critical. The turbulence is affected by Ro but not by Re. Confirming the waveguide nature of the core, the perturbations countering the swirl were found to survive long distances but in the vortex core only where the azimuthal, radial and axial velocity profiles are linear. They even amplified, albeit in a narrow frequency range (80–100 Hz) of the perturbation. However, in the co-rotating case, the perturbations attenuated in that frequency range.

An emerging clarity in the research of the last three decades is the discovery of coherent helical secondary structures in the vortex core and how their interactions are related to vortex bursting. Bandyopadhyay, Stead & Ash (1991), in the apparatus described above, have shown that the core of a long trailing vortex has intermittent patches of turbulent and laminarescent fluids. The shear stress rich core fluid intermittently ejects radially outwards, indicating that there is self-regulating turbulence production in the core. This result suggests that the quasi-periodic vortex bursting in the core is similar to the bursting phenomenon in the wall layers of turbulent boundary layers (Hama, Long & Hegarty 1957; Kline *et al.* 1967; Townsend 1976; Adrian & Marusic 2012). From the control point of view, Einstein & Li (1958) and Bandyopadhyay & Hellum (2014) have modelled this as a self-regulation process. This perspective puts vortex bursting in the broad framework of turbulence regeneration in all shear flows, and even with the mechanisms of swimming and flying in animals (Bandyopadhyay, Leinhos & Hellum 2013; Bandyopadhyay 2015), and how the motion is controlled by olivo-cerebellar dynamics in animals (Kazantsev *et al.* 2004; Bandyopadhyay *et al.* 2008*b*).

Misaka *et al.* (2012) have carried out large eddy simulation of atmospheric aircraft contrails. In certain conditions of stratification and turbulence, vortex reconnection is found to generate helical vorticity structures that travel along the cores. These secondary vortex structures have been found to collide, causing vortex bursting. These results may have some relevance to the present work.

Independent of the type of vortex bursting, namely the bubble type or the helical type, both the flow visualization data trends and similarity analysis show that the

pipe flow Reynolds number of vortex breakdown at a fixed location in a pipe is proportional to the circulation number ($\Omega = \Gamma/(UD)$, where Γ is the circulation of the vortex, U is the average pipe flow velocity and D is the pipe diameter). This number is inversely proportional to the ratio of the inflow radial as well as the tangential velocities (Escudier & Zehnder 1982; Benjamin 1962). In a swirling water jet in a closed chamber without air entrainment and bubble formation, vortex breakdown is found to have hysteresis, secondary motions and precession of the stagnation point with respect to the upstream vortex (Billant, Chomaz & Huerre 1998).

Oscillating grids have been used in a large rotating tank flow, the Rossby number (Ro) being 3 to 33 near the grid. Away from the grid, at a local Ro of 0.2, quite dramatically, a large number of long and concentrated small diameter vortices are formed which rotate parallel to the tank flow and whose core vorticity is much higher than the vorticity of the tank flow. These small vortices sustain travelling helical waves. The interaction of the waves cause bursting and the formation of small scales. The broken cores can reconnect, be destroyed or reconnect at a much larger time scale (Hopfinger *et al.* 1982).

The mechanisms of vortex breaking (with circulation dropping below 5 %) and reconnection help us understand how turbulence becomes three-dimensional. Saffman (1990) has modelled the mechanisms and the time scales of this process. The hypothesis is that when two vortex filaments of equal and opposite strengths touch, viscosity will cancel the vorticity. The centrifugal force in the core will then drop and local pressure will increase. This will create an axial acceleration – a jetting in the core. In the present work, we seek evidence of this jetting since that is amenable to bubble visualization. We also seek evidence as to whether vorticity is carried away from the initial contact point and a reconnection is produced.

Both connection and rejoining times are inversely proportional to circulation (Γ; $m^2 \ s^{-1}$), for constant values of other (geometric) parameters. We expect these times to drop with f^2, where f is frequency of flapping (lift force $L \propto f^2$, and $L = \rho U \Gamma$, where ρ is density and U is velocity). Compared with the measurements of colliding rings (Schatzl 1987), in agreement, Saffman's modelled time for connection is 0.7 s. However, the peak vorticity is not in agreement. The breaking time in the experiments is 0.2 s, and the modelled rejoining time is 0.4 s. These times will be compared with those in the present work.

Tsoy *et al.* (2018) have used cavitation bubbles as vortex markers in a diffuser to visualize the Kelvin modes formed in a vortex tube after reconnection. Kelvin wave modes $m = 0, 1, 2$ were observed to propagate along the axis. The modes observed will be compared with those in the present work.

The low-frequency helical coherent structures observed in the experiments on vortex breakdown bubbles have been difficult to reproduce in stability analysis. The asymptotic stability analysis and direct numerical simulation show that the low-frequency inflow perturbations penetrate the vortex bubble and are amplified to produce the coherent structures while the high-frequency perturbations are convected around the periphery of the bubble (Paterson, Wang & Mao 2018).

The vortex breakdown in a closed cylinder, such as a combustor, produces a recirculating region. Numerical analysis shows that before bursting, the initially longitudinal vortex expands radially and produces two stagnation points within which the recirculation region is produced. The eigensystem of the velocity vector tensor near the points of stagnation has been investigated (Yamada & Suzuki 2016).

Vortex breakdown takes place in adverse pressure gradients. For this reason, in a delta wing, the location of the bursting of the leading edge vortex translates axially

with angle of attack. In pipe flows, the diameter is flared (half-angle of approximately 1.4°, Sarpkaya 1995) to induce an adverse pressure gradient.

In a vortical flow, the axial pressure gradient across the core rises in proportion to the swirl (Hall 1972). As a result, the streamlines diverge and vorticity is convected away from the centreline. Since diffusion is a slow process, the convected vorticity may exceed the centreline vorticity. A bubble of separated flow is produced which is known as vortex bursting (Spall & Gatski 1991).

In slightly flared, non-cavitating and swirling pipe flows, Sarpkaya (1995) has shown that four types of vortex bursting can occur: a double helix type, an axisymmetric type, a helical type and a conical type. The conical type has been observed in a high Reynolds number ($Re = UD/\nu = 225\,000$, where ν is kinematic viscosity of water) turbulent pipe flow. The first three types have been simulated numerically in an unbounded decelerating flow (Spall & Gatski 1991).

Distinct pressure pulse spectra with audible tones, probably related to the swirl, have been measured in the vicinity of the vortex bursting in single- and two-phase pipe flows. The liquid phase flow rate was found to dominate the spectral properties of the vortex breakdown (Hugo & Veer 2003).

In a delta wing, the location of the breakdown of the leading edge vortex can be moved towards the apex of the wing by as much as one wing chord by positioning a thin wire near the leading edge. The wire diameter is one per cent of the vortex core diameter of the pre-breakdown vortex and the wire length equals the distance to the breakdown location from the apex in the absence of the wire (Akilli, Sahin & Rockwell 2003).

Consideration of bursting as the response of a blob of vortex to pressure gradient obscures the building block of the bursting mechanism. Some researchers have implicated both spiralling vortex tubes and their bursting to the limiting trends of turbulence spectra (Lundgren 1982; Cuypers *et al.* 2003). For this reason, the present work on bursting of DH vortices, where length and time scales vary by a factor of 100, may have a basic relevance to turbulence cascading.

Very few wave equation models (Saffman 1990) have considered bursting as the interaction of elementary vortex tubes. A direct side-to-side comparison of how contra- and co-rotating vortex tubes interact, produce waves and burst in pressure gradients has not been done. This work fulfils this need giving direct visual evidence.

We also consider the elastic effects of aeration of the vortex tubes near a free surface. The literature regarding the elasticity of aerated vortices has been difficult to locate. We have an opportunity to visualize the mechanism of how bubbles are formed due to the instability of vortex tubes and bursting.

Spiralling waves propagate in vortices whose diameter is changing. Stretching changes vortex diameter. Here, we examine the role of stretching of aerated vortices in bursting and bubble formation.

1.2. *Background of this work*

An abrupt change in the structure of the core of the vortex due to helical instability is a preliminary indication of vortex bursting. The presence of an axial velocity may be the source of the helical instability. The vortex bursting discovered in the present work has not been previously studied, given the presence of the free surface, the entrainment of a core of air during the formation of the vortex, unsteadiness, the finiteness of the length of the vortex and the self-regulating nature of the imposed wave–wave interaction.

Pumps and turbines in hydraulic plants produce steady air intake vortices when the Froude number $Fr > (0.23–0.30)$. Air-entrained vortices at hydraulic intakes are generally avoided for reasons of cavitation-induced erosion of blades, unsteadiness and noise. Circulation Γ and Froude number Fr determine the submergence depth required to avoid the formation of an intake vortex; the Reynolds number Re and the Weber number We are of less importance (Odgaard 1986; Hite & Mih 1994). Such intake vortices are steady and do not burst. In addition, a root vortex is a source of drag in turbomachinery.

Gordon's (1970) dimensional analysis indicates the dependence of submergence s on intake velocity v and intake tube diameter d as per $s = Cv\sqrt{d}$, where the constant C is 0.3 for a symmetric intake. Limited site measurements indicate that intakes are the source of a problem in cases where $s < 0.3v\sqrt{d}$. In a non-dimensional form, $(s/d) \propto (Fr)^n$, where the Froude number is given by $Fr = v/\sqrt{gd}$ and the exponent $n > 1$. No intake vortex is formed when $Fr < (0.23–0.3)$ (Humphreys, Sigurdsson & Owen 1970). Above that range of Fr, a greater submergence depth, given by a power relationship, is required to avoid the formation of the intake vortex. Otherwise, special swirl mitigation devices are required. A Rankine vortex model of the intake vortex suggests that critical submergence depends on not just Fr but also on the circulation number $(\Gamma/(vd))$; Re and We do not have significant effects (Odgaard 1986). The mechanisms of air entrainment by a vortex at a free surface is not understood beyond the semi-empirical steady case discussed above.

The subject of air entrainment by a surface vortex is important in air–sea interaction and weather forecasting. Bubbles near an oceanic free surface have an effect on thermal flux, optical transmission and biological life while also generating noise. Although the bubble size distribution is important in these effects, their formation mechanism is not well understood (Deane & Stokes 2002).

Modelling shows that the tightening of a spiralling vortex produces a cascade of velocity fluctuations to the smaller scale described by the Kolmogorov $k^{-5/3}$ energy relationship (Lundgren 1982). The smaller scale from such a strained vortex is similar to the small-scale structure of turbulence which is known to be spotty and rod like. Amplification of vorticity and vorticity gradient takes place which concentrates the vorticity into thin sheets and tubes (Batchelor & Townsend 1949; Kuo & Corrsin 1971).

At the sea surface, the naturally produced sound from wind driven breaking waves in the range 200–50 000 Hz comes from the rings of individual resonant bubbles formed in the splashes (Medwin & Beaky 1989; Medwin *et al.* 1992; Nystuen 2002). Upon sudden release, the formation of arrays of bubbles of identical size can be expected when air is entrained by a vortex, and the vortex is strained. The oscillation frequency ranges in the present work and those in the buoy measurements are compared later.

Bubbles amplify noise up to 100–200 Hz (Prosperetti 1988). From 200 Hz to 1 kHz, the collective oscillation of bubbles contributes to noise. Including compressibility effects, Fuster & Colonius (2011) have modelled the radial surface oscillations and the propagation of the surrounding pressure waves in bubbles in a cluster. In the flow here, the presence of the foil wall near the clouds of fine bubbles and the sudden formation of the identical coarse bubbles in arrays from air tubes would provide directionality to the radial oscillations of the bubble surface and to the propagation of the surrounding pressure waves.

1.3. *Problem statement*

The questions are: Why does a vortex burst, what is the role of vortex stretching, how are waves formed and how are the bubbles formed when an aerated vortex bursts? We ask: What are the zones of instability of an aerated vortex? And, how do they relate to bubble formation? Theoretical modelling of vortex breakup (Saffman 1990) and numerical simulations of wave breaking (Lubin & Glockner 2015) and bubble formation mechanisms (Fuster & Colonius 2011) have improved our understanding of vortex bursting, aeration and bubble formation near a free surface. Bursting of aerated vortex tubes involve small scales of time and length. Accurate computations of oscillating interfaces in wide ranges of parameters may be prohibitive. Hence, a visualization experiment of the complex flow field may reveal new insights.

The article describes a flapping foil flow apparatus using a minimum amount of torque input to produce an air-entrained, short transitional vortex causing its bursting in each cycle. The formation of transient small and standing capillary waves in the vortex funnel, to the formation of divergent surface waves seen only at very large scales, are shown in the same laboratory-scale apparatus. The foil pitching produces a short double helix aerated root vortex of contra-rotating circulations $\pm \Gamma$ near the free surface. Down below in the foil boundary layer, pairs of co-rotating vortex tubes of (Γ, Γ) circulations spiral around each other and they are visualized by fine bubbles. Abrupt removal of the pitching obstruction triggers the bursting. The bursting produces bubbles. Sometimes extremely compact DH vortex, buckled to a toroid like Hill's vortex, is formed bursting spectacularly. A nonlinear vortex lift model of the DH for the condition of maximum stretching is given. A force model of bubble formation is given. The ringing frequencies of bursting vortex tubes and bubbles are compared with buoy measurements. The evidence of maximum vortex stretching, breakup, vortex reconnection, post-breaking formation of vortex jets, regimes of bursting and bubble formation are given. The results are compared with the vortex breaking model of Saffman (1990) and the observations of Kelvin waves by Tsoy *et al.* (2018) among others. A simplified buckled vortex model is used to estimate the modulus of elasticity of an aerated vortex.

The following appear in the supplementary information (hereafter cited as SI): (A) Text, (B) Data, (C) Image and (D) Video. The section '(A) Text' gives the perspective of the aerated vortex, of the surface wave and bubble results in sections: A.1 Relationship between the aerated root vortex flow and other vortex dominated flows; A.2 Surface waves (A.2.1 Transient divergence waves; A.2.2 Capillary waves); A.3 Estimation of bubble Re, We and C_d due to the two mechanisms of formation; and A.4 Initial condition dependence: cycle-to-cycle concatenation. Part '(B) Data' gives the background data of the experiment. Part '(C) Image' gives additional examples of the vortices. Part '(D) Video' gives the description of the four videos.

2. Experiments

2.1. *Background of the flow apparatus: wave–wave interaction*

Wave–wave interactions in oceans and olivo-cerebellar control dynamics (Kazantsev *et al.* 2004; Bandyopadhyay *et al.* 2008*b*) have been extensively studied. They are beginning to receive attention in modelling and laboratory fluid dynamic research (Bandyopadhyay *et al.* 2012; Bandyopadhyay & Hellum 2014; Bandyopadhyay 2019). Swimming and flying mechanisms of animals show that the propulsive surfaces undergo orthogonal rolling and pitching oscillations (Bandyopadhyay *et al.* 2012) given by

$$\phi(t) = \phi_o \sin(2\pi f t), \tag{2.1}$$

$$\theta_{root} = \theta_{o,root} \sin(2\pi ft + \psi) + \theta_{bias}, \qquad (2.2)$$

$$\theta_{tip}(t) = \theta_{o,tip} \sin(2\pi ft + \psi) + \theta_{bias}, \qquad (2.3)$$

$$\theta_t = \theta_{tip} - \theta_{root}, \quad \text{and} \qquad (2.4)$$

$$\theta_{to} = \theta_{o,tip} - \theta_{o,root}, \qquad (2.5)$$

where ϕ_o and θ_o are the amplitudes of the roll and pitch oscillations, respectively; f is the frequency of flapping; t is the time; $|\psi|$ is the phase difference between roll and pitch oscillations, usually kept at 90° for optimal efficiency; θ_{bias}, if used, is the pitch bias used for yawing in the horizontal plane; and θ_t is the foil twist angle (figure SI-DA-1). The subscripts *root*, *tip* and *o* refer to the foil root, foil tip and amplitude of the oscillation angle, respectively. Here, ϕ controls the forces produced, θ controls the blockage and the timing of the vortex formation and bursting and θ_t reduces the spanwise variation of the velocity field (Bandyopadhyay *et al.* 2012). Equations (2.1)–(2.5) produce the vorticity spirals – uniform and conical – of Kelvin mode $m = 1$ in axis t and pitch f shown in table 1; for spatial trajectories of a particle obtained using these equations, see figure 2(*d*) in Bandyopadhyay (2019).

The foil velocity is given by $U_{foil}(t) = \dot{\phi}(t)R_{avg}$, where R_{avg} is the average foil span. The angle of attack (AOA) is given by $\alpha(t) = a\tan(U_{foil}(t)/U_\infty) + \theta(t)$. Here, U_∞ is the foil tow speed or induced flow speed when hovering. The vortices shed downstream affect the instantaneous upstream streamlines (Bandyopadhyay *et al.* 2013). The forces produced and efficiency are affected by pitching via the AOA.

When efficiency is optimized for cruising, the frequency, amplitude and velocity of the oscillations of the propulsive surface and of the wake match in phase – a condition called foil-wake 'lock-in'. Efficiency reaches a maximum if the oscillators are resonant and the losses of the foil driving mechanism are minimal. Then, the foil responds to all five dominant harmonics of the wake (Beal & Bandyopadhyay 2007). Theoretically, olivo-cerebellar ionic control has a similar self-regulation mechanism for ion-by-ion control of vortex shedding to control the hydrodynamics of swimming and aerodynamics of flying at all instants of time (Bandyopadhyay 2015, 2016, 2019). If the device producing the wake/jet has a high quality factor ratio (low friction), the foil and wake approach lock-in and self-regulation (Bandyopadhyay 2015). Insect wings approach this condition (Ellington 1999; Bandyopadhyay 2019).

Self-regulation is common to oscillatory natural phenomena. The processes are quasi-steady, low-dimensional and weakly nonlinear. Their features – perturbation by orthogonal waves and resonant oscillation at a critical frequency – are used in an apparatus to examine vortex bursting and bubble formation mechanisms near a free surface. The two-phase vortex bursting reported is new.

In experiments on optimal cruise swimming, the flapping frequency is kept below 1 Hz when the forces are low (1 N). Since force $\propto f^2$, the f should be below 0.5 Hz at higher loads (10 N). A constant value of the Strouhal number, generally between 0.20 and 0.40 – the ideal target being 0.30 in water (Bandyopadhyay 2019) – and a fixed value of ϕ_o are maintained. The cruising criteria are used, although the wave-generating foil device is not towed.

That the apparatus uses close to minimum energy to produce the vortex is proven in a sloshing propulsor where the twisting blades can both roll and pitch (sloshing) in much the same way as here, or spin as in conventional propulsors (Bandyopadhyay 2016). During sloshing, the temporal history of the Bollard thrust (in the hovering mode when it is not towed) at $f = 0.2$ Hz shows that the minimum value is close to 0 N, but never negative (figure 8, Bandyopadhyay 2015). Although $f = 1$ Hz in

the present apparatus when a root vortex is first produced, it is still assumed not to produce a wake at any time.

To make the energy input exactly minimal, the wave-generating foil and the flow should be locked in. This is not possible in the foil drive in figure 1, which has gears causing friction. Our recently developed low-friction hemispherical motor is gear free but is suitable for small forces only (Bandyopadhyay 2019).

2.2. *Flow apparatus*

The experiments were performed in the Low Speed Tow Tank at the Naval Undersea Warfare Center, Newport, Rhode Island. The differences with the apparatus described in Bandyopadhyay *et al.* (2012) are that a surface plate is not used, allowing air entrainment, and the foil root is flush with the free surface. A schematic of the flow and torque arrangement is shown in figure 1(*a*) (top), and a photograph of the foil just submerged in water (the foil root is flush with the free surface) is shown in figure 1(*b*). The lower part of figure 1(*a*) shows the time traces of ϕ and F_x, the force in the forward direction. Thrust is produced twice per cycle of foil oscillation. Torque is at a maximum or minimum at an extreme of the foil excursion, but thrust is at a maximum or minimum in between. Figure SI-DA-2 shows typical time traces of ϕ (deg), the difference between the AOA at the foil root and tip ($\alpha_{root} - \alpha_{tip}$) (deg) (demonstrating uniformity along the span achieved with twist), F_x (N), roll torque (Nm) and hydrodynamic power $P_{hydrodynamic}$ (W) when a top horizontal surface plate is installed to prevent air entrainment caused by the formation of surface waves and a root vortex (Bandyopadhyay *et al.* 2012). The pitch (including twist) torque is 10 % of the sum of the roll and pitch torques. The input roll, pitch and twist torques are assumed to be the same for the foil whether it is exposed to the free surface or not, because there is no feedback from the flow to the foil. The torque sensor measurements without any entrainment, when extrapolated to the case with entrainment, show that 5 % of the total torque is spent to make the surface waves and root vortex.

Figure 1(*c*) is an image of the coarse and fine bubbles in the root and foil regions, respectively. The coarse bubbles are formed away from the foil, and the fine bubbles are formed on the foil. This demarcation shows that the complex flow is a jigsaw puzzle of autonomous instabilities. The schematic (figure 1*a*) shows how the orthogonal oscillating roll (τ_{ϕ_o}) and pitch (τ_{θ_o}) torques are configured with respect to the wavy free surface and how the air intake vortex is situated as a cross-product at an angle (figure 1*b*). There are two paths of air entrainment – one via the root vortex and the other via the foil surface downspan. The foil shows no cavitation erosion or noise (see figure SI-DA-5). The hovering foil sets up an induced jet flow because the Strouhal number of flapping is selected appropriately.

The apparatus is described in Bandyopadhyay *et al.* (2012). The non-dimensional parameters are *Re*, *Fr*, *We*, *Bo*, *Ca* and Γ; figure 1(*a*) shows these parameters as relevant to coarse and fine bubbles. Here, *Fr* is Froude number, *Bo* is Bond number, *Ca* is capillary number, *Re* is Reynolds number, *We* is Weber number and Γ is circulation. The ratios of the destabilizing inertia (F_i) and stabilizing viscosity (F_v), gravity (F_g), and surface tension (F_γ) forces define the ratios as $Re = F_i/F_v$, $Fr = F_i/F_g$, $We = F_i/F_\gamma$, $Bo = F_g/F_\gamma$ and $Ca = F_v/F_\gamma$. Circulation Γ (m^2 s^{-1}) is defined as the product of the velocity (m s^{-1}) and the length (m) scales. Rossby number (*Ro*) and swirl ratio (*S*) are defined to account for the destabilizing inertial (F_i) to Coriolis (F_c) forces as $Ro = F_i/F_c$, and $S = F_c/F_i$; it is more convenient

to define these ratios in terms of axial and circumferential velocities for inertial and Coriolis forces, respectively. The ratio Ro is preferred if F_c dominates as for individual vortices. In the older literature on bursting, S has been used.

2.3. *Relationship between the aerated root vortex flow and other vortex dominated flows*

The similarity among oscillatory transitional vortex flows such as the aerated root vortex, flapping foil propulsion vortex, cylinder self-oscillation induced by wake vortex flows and the delta wing leading edge vortex is discussed in SI-A.1. An overview follows. Delta wings have sharp leading edges like the trailing edge of the present foil. The flapping trailing edge lift mechanism can be compared with the delta-wing lift mechanism in Polhamus (1966),

$$C_L = C_{LP} + C_{LV}, \tag{2.6}$$

where C_L is total lift coefficient, C_{LP} is the potential flow linear component of C_L and C_{LV} is the nonlinear vortex lift coefficient. A similar breakdown appears in figure 5(inset 2) from flapping foil propulsion (Bandyopadhyay *et al.* 2008*a*). The inset is similar to the lift figures in Polhamus (1966). In §3.5, the vortex lift is modelled using equation (2.6) attributing the entire foil lift to the trailing edge vortex.

The entrainment at a given f and other foil kinematic parameters is

$$\overline{Q} = Q_{root} + Q_{foil} = \text{constant}, \tag{2.7}$$

where $\overline{Q}$ is the average of the total entrainment of atmospheric air per cycle of oscillation. In a cycle, Q_{root} is the root vortex entrainment at the trailing edge, and Q_{foil} is the foil boundary layer leading edge entrainment. Since the input torque is the same cycle to cycle, $\overline{Q} = \text{const.}$ When $f = 0.75$ Hz, no root vortex is produced and $\overline{Q} = 0$. Entrainment increases with input torque and $\overline{Q}_{f=1.25 \text{ Hz}} > \overline{Q}_{f=1 \text{ Hz}}$. In figure SI-DA-4, at $f = 1$ Hz, the root and foil apportioning lies near one end of the graph. But at $f = 1.25$ Hz, the cycle to cycle apportioning moves over the entire range of the graph linked by their history. At $f = 1$ Hz, $Q_{root} > Q_{foil}$ in most cycles. At $f = 1.25$ Hz, both $Q_{root}, Q_{foil} > 0$, and can be of similar magnitude due to the role played by translating small secondary surface vortices affecting the orientation and size of the main funnel pierced by the foil. Section 3.10 gives the concatenated apportioning of $\overline{Q}$ into Q_{root} and Q_{foil} since $\overline{Q} = \text{const.}$ The flow has a lower degree of freedom and is less chaotic at $f = 1$ Hz.

Vortex bursting is seen only in the aerated root vortex and the delta wing but not in the leading edge vortex of the flapping foil suggesting influence of Ro over Re in salient edge vortex. Self-regulation (Khalil 1996; Bandyopadhyay & Leinhos 2013) is explained in SI-A-1 by comparing linear and nonlinear oscillators. The departure from self-regulation is a measure of the wasteful friction in an oscillatory flow.

2.4. *Flow parameters*

The foil forces are proportional to f^2 in the fully submerged case. The slanted root vortex is not formed at 0.75 Hz; a transitional vortex is formed at 1.0 Hz; and the vortex is mostly turbulent at 1.25 Hz. With increasing f, the foil needs to be located at greater submergence in order to avoid an intake vortex.

Using the helicopter rotor model, estimate the induced velocity as $U_{ind} = \sqrt{(\overline{F_x}/(2\rho A_s))}$, where $\overline{F_x}$ is the cycle-averaged force (N) in the forward direction, ρ is the density (kg m^{-3}), A_s ($= (1/9)\pi(r_o{}^2 - r_i{}^2)$(m^2)) is the foil swept area (Wakeling & Ellington 1997), r_o is the outer foil radius and r_i is the inner foil radius. Since $\overline{F_x} \propto f^2$, $U_{ind} \propto f$. Because the foil motion creates surface waves, gravity is the stabilizing force and inertia is the destabilizing force. Therefore, their ratio is given by the Froude number $Fr = U_{ind}{}^2/gc$, where g is acceleration due to gravity, and c is the chord of the foil (NACA 0012 section, $c = 0.1$ m, span $= 0.30$ m), which is a measure of the maximum blockage (the maximum thickness of the foil and the stem holding the foil are similar: this dimension gives the minimum blockage). We write $Fr \propto f^2/(gc) \propto f^2$. Since $c = 0.1$ m, $gc = (1$ to $0.12)$ m^2 s^{-2}, for full to minimum blockage. For $f = 0.75$ Hz, 1.00 Hz and 1.25 Hz, Fr is in the multiples of 0.5625, 1.0 and 1.5625, respectively. Movie 2 and figure 5 show that $f = 1.0$ Hz is where the longest and the thinnest tightly wound 'disturbed-laminar' (DL) helical root vortex is formed from the pristine initial condition (a flat free surface without any pre-existing turbulence in the wake) and when the blockage is at its maximum, and it unwinds into a DH when the blockage is reduced to 0.12 of the maximum value of the blockage. No root vortex is formed at $f = 0.75$ Hz, and a generally turbulent vortex is formed at $f = 1.25$ Hz. The applied inertial and the stabilizing gravity forces are in best balance when $f = 1.0$ Hz. The trailing edge rotational velocity and external foil-induced horizontal velocity give estimates of the non-dimensional force ratios.

In all vortices, vortex slants of $0° \leqslant \beta \leqslant 45°$ are stable and unstable thereafter, and bubbles are formed when the vortex is unstable. The DL cases appear in figure 2, and SI-IA-2 to SI-IA-4, all at $f = 1$ Hz. The turbulent cases appear in figures 4(c1,d1), 6(a1) and 6(d1,d5), all at $f = 1.25$ Hz. In tornadoes also, the swirl ratio boundary between the DL and turbulent cases is not sharp (Trapp 2000).

The DH is clear in the DL case after unwinding and when bursting, but it is clear in the turbulent case right when it is formed before bursting (unwinding is not observable). The pitch of the winding is $\geqslant 2c/3$ in the DL case, but is $< 2c/3$ in the turbulent case. The windings of the vortex tubes in the turbulent case has been called the aerated Taylor tubes, which are not formed in the DL case. The bubbles formed from the Taylor tubes are smaller, but they are larger in the DL case. The funnel diameter is $\leqslant$ the root vortex diameter in the above two classifications. The cases where the funnel is larger (figure 9n) do not show any DH but they have Taylor tubes and they have been called turbulent.

The pre-burst turbulent root vortex has these features: the formation of small diameter arrays, aerated and counter-rotating Taylor cells (figure 9e), a sharp conical apex (figure 9i), a lower aspect ratio (length/diameter; figure 9a1) than in the DL case and smaller 'coarse' bubbles formed post-bursting (figure 6 versus figure 9a). Only the root vortex formed in the first cycle at the lowest f of vortex formation, $f = 1$ Hz when $Ro = 0.20$, has been called 'DL' (figure 2, and figures SI-IA-2 to SI-IA-4). The rest fall in the turbulent case. The appearance of the smallest diameter vortices is the prominent feature of the fully turbulent cases: in the Taylor cells (figure 9e) and in the turbulent root vortex DH arms (figures 4c1, 4d1) at the origin of formation $(x, y, z = 0)$. The features of bursting and bubble formation are similar except that the Kelvin modes are not apparent in the DL case. While input $\dot{\theta}$ torque is a constant cycle to cycle, the swirl experienced by the flow (Ω_y) at the origin $(x, y, z = 0)$ may be a determinant of the flow variations (figure 3a). See the flow at $(x, y, z = 0)$ in Movie 3.
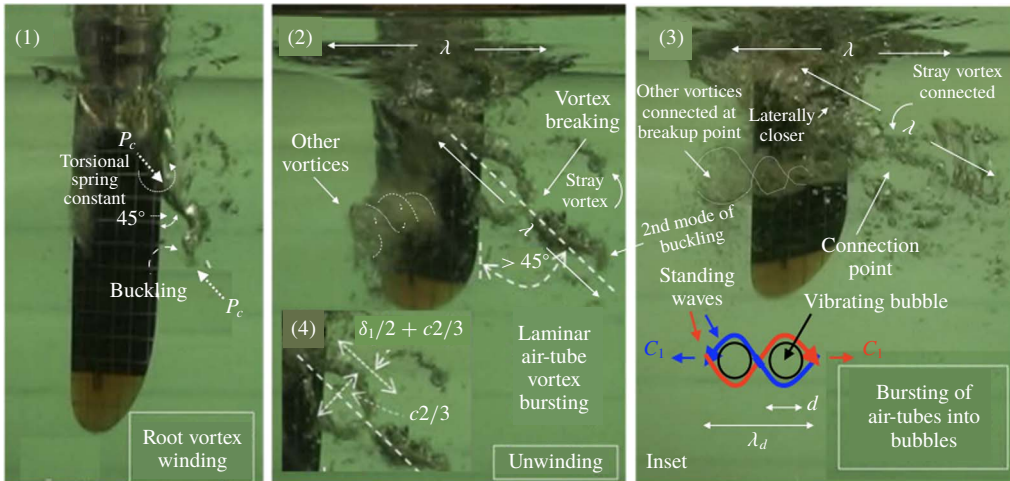
FIGURE 2. Time sequence (1–3) of an example of the elastic behaviour of air-filled, unsteady, 'disturbed-laminar' root vortex. The location of vortex breaking is shown in panel 2. Panel 3 shows that other vortices congregate at the breakup point. Inset (4) shows the scales of the double helix in (2), where c is the foil chord length and δ_1 is the foil stem diameter. Thin double helix lines are added in panels (2) and (3) to aid recognition of the organization of the fine bubbles approaching the breakup point. P_c is compression. The zig-zag buckling in (1) becomes the hook-shaped second mode of buckling of a cantilever beam in (2). The torsional spring constant shown in (1) is a boundary condition resisting the buckling. Relative phase of $\phi = 0°$ (1), $60°$ (2), $105°$ (3). Foil parameters are $\phi_o = 40°$, $\theta_o = 45°$, $\theta_{to} = 75°$, $f = 1.0$ Hz, $\psi = 90°$. Inset in panel 3 shows the mechanism of bubble formation: see text. Panels 2 and 3: when the vortex unwinds, the free surface oscillates vertically extending axially over λ, the double helix wavelength.

Generally, the inertial force is the destabilizing force, while the restoring forces are surface tension, gravity and viscous forces. For the bubbles, the following non-dimensional numbers can be used to measure the ratio of the destabilizing and restoring forces because they can vary with depth or bubble size. The ratio of inertia to surface tension is given by the Weber number $We = (\rho V^2 d)/\sigma$, where ρ is the density of water (kg m^{-3}), V is the velocity (m s^{-1}), d is characteristic length, namely the diameter of the bubble (m) and σ is surface tension (N m^{-1}) (γ in (3.2), and T in capillary wave discussion). This variable is also a measure of the ratio of kinetic energy of impact of formation to the surface energy. The Bond number Bo measures the ratio of the gravity force to the capillary force. It is given by $Bo = (\Delta\rho g d^2)/\sigma$, where $\Delta\rho$ is the density difference of the two phases (kg m^{-3}), and g is acceleration due to gravity (m s^{-2}). Surface tension dominates for $Bo \ll 1.0$, and gravity dominates for $Bo \gg 1.0$, with an intermediate range where both effects are present. Coarser bubbles have higher Bo. The shape of the bubble is characterized by the Morton number, simplified for air bubbles whose density is negligible compared to that of water, as $Mo = g\mu^4/\rho\sigma^3$, where μ is the absolute viscosity of water (Ns m^{-2}). The ratio of the inertial and gravity forces is given by the Froude number $Fr = V^2/gd$, where d is the diameter of the bubble (m). The volume of an irregular bubble, or several bubbles attached together but not coalesced, can be converted to an equivalent spherical bubble. The capillary number Ca, which is the ratio of the
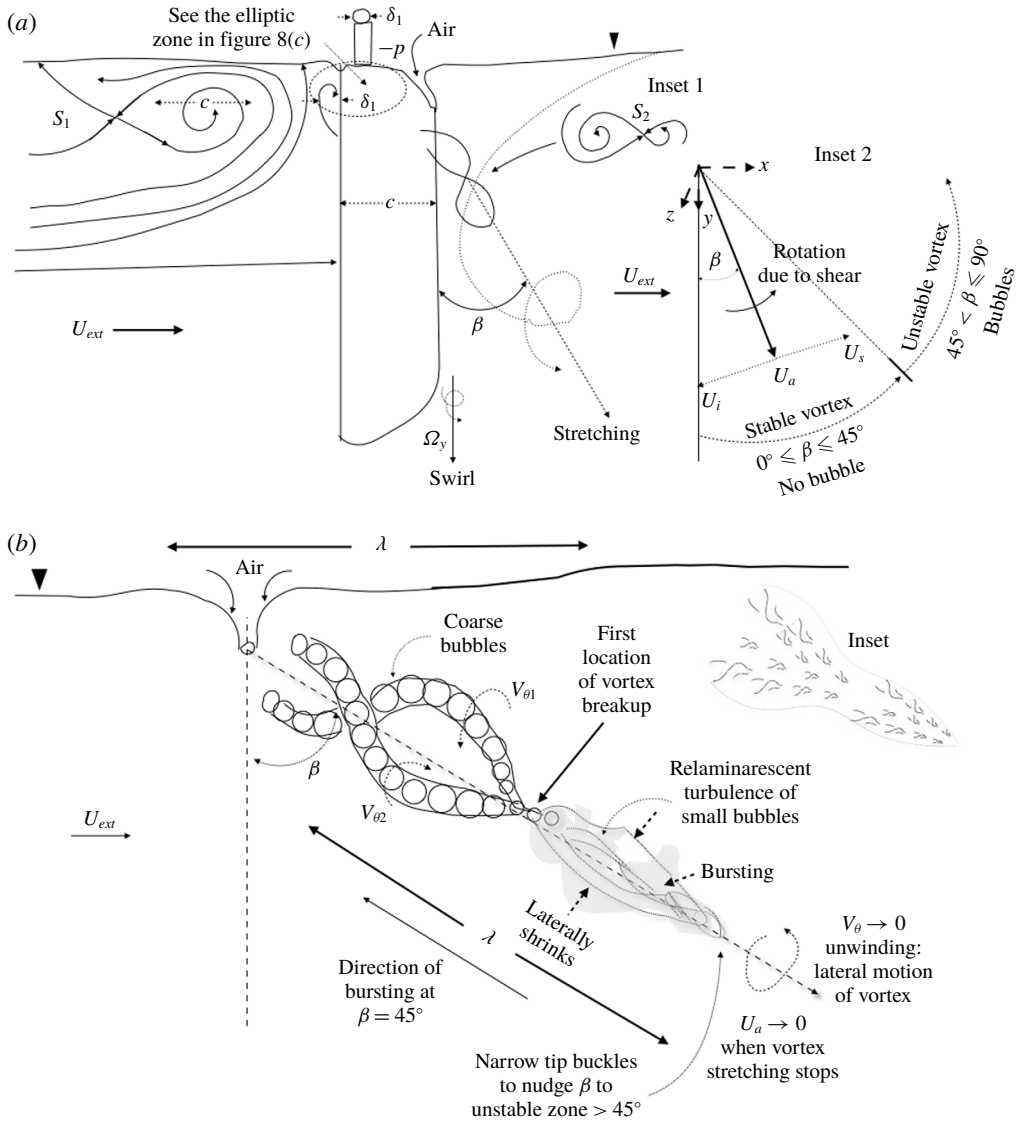
FIGURE 3. Schematics of vortex elasticity and breakdown. (*a*) Synthesis of the formation (winding) of the root vortex; see figure 2(1). (*b*) Unwinding of the root vortex and location where the first vortex breaking takes place (see figure 2(2)); direction of bursting (also see figure SI-IA-4) is shown; foil not shown. In panel (*a*) inset 1: saddle S_2 at vortex crossing; and inset 2: U_a is stretching velocity, U_i is induced velocity of root vortex, U_s is direct shear velocity resisting U_i, (x, y, z) is coordinate system, Ω_y is trailing edge swirl and regions where β is stable and unstable, where bubbles are not formed and formed respectively, are shown. The inset in (*b*) is a representation of the agglomeration of smaller double helix vortex structures in the relaminarescent region post-bursting; also see the burst vortex arrowhead in figures 11(2) and 12.

stabilizing forces – viscous forces and surface tension – is considered later in relation to the formation of fine bubbles over the foil surface where the viscous forces in the boundary layer and the wettability have strong effects.

The above non-dimensional numbers are related as $Mo = We^3/FrRe_d{}^4$. Here, Reynolds number Re_d, the ratio of inertia to viscous forces, is defined as $Re_d = Vd/\nu$, where ν is the kinematic viscosity of water (m^2 s^{-1}). This relationship can be used to check the internal consistency of the estimates of bubble diameter d, which is the common primary variable in all the non-dimensional numbers and is a measure of surface energy.

The diameter of the bubbles formed away from the foil surface increases as depth reduces. Arched ellipsoidal bubbles have also been observed. This occurrence signifies that the bubble drag law changes in the present work (Haberman & Morton 1953). This indicates variations in the organization of the mechanisms of bubble formation. The drag of the fine bubbles may be assumed as the same as the drag of equivalent solid spheres, but that would not be true for coarse bubbles. The internal circulation of the bubbles may be of significance. The water used was filtered. Therefore, the drag is expected to be slightly lower than of tap water. The secular Re_d versus C_d trend, up to the bottom of the drag bucket, is valid for $Re_d < 250$. Since neither the temperature stratification in the tank (figure SI-DA-3) nor the span of the foil is large, the change in the density of air can be neglected. The non-dimensional parameters for the two types of bubbles are estimated in section A.3 in the SI with an overview given in § 3.7.

3. Results

The results are presented in the parts: (i) surface waves, divergent and standing (see section A.2 in the SI for details); (ii) the elastic behaviour of the relaxation and bursting of stretched 'DL' and turbulent root vortices; (iii) a synthesis of the DL vortex bursting; (iv) the progression of the vortex slant to 45° to maximize stretching, vortex breaking, jetting and the formation of Taylor air tubes similar to Taylor–Couette roll cells, all just prior to bursting; (v) an estimation of the maximum nonlinear vortex lift reached prior to bursting; (vi) mechanisms of bubble formation: (a) in root vortex bursting, and (b) in the bursting of the air jacketed foil boundary layer on the suction side (see SI-A.3); (vii) the formation of Kelvin spirals in the foil-tip vortex tubes just prior to bursting; and (viii) initial condition dependence – concatenation in cycle-to-cycle variation in root and foil entrainment that affects lock-in (details appear in SI-A.4). (ix) The existence of a preferred connection point of vortices in proximity is shown. (x) The buckling of an aerated vortex is modelled to estimate the modulus of elasticity. (xi) A summary of the conditions of bursting is given. (xii) In a tabular form, the discussion gives an album of the organized vortex motions and jetting visualized.

3.1. *Surface waves*

The spiralling surface waves provide the initial condition of the formation and bursting of the root vortex. The surface waves are organized and start a domino effect of the fluid dynamics, namely, air entrainment, vortex formation, bursting, bubble formation in two sizes and the apportioning of entrainment between the vortex core and the suction side of the foil, which in turn affects the proportions of the coarse and fine bubbles formed. The detailed results are given in A.2 Surface waves (A.2.1 Transient divergence waves; A.2.2 Capillary waves) in SI-TA. An overview is given below.

3.1.1. *Transient divergence waves*

Figure SI-TA-1 shows an example of Kelvin envelope seen at one instant of time in the oscillation cycle and only at $f = 1.25$ Hz. In figures SI-TA-1(a,b), the caustic lies in one quadrant only and is an arch and not straight, as it would be for a sailboat cruising straight along a channel. The Kelvin envelope angle of 19.5° can be discerned only as a limiting value at the midline of the flow geometry. The surface waves are phase-to-phase quasi-steady, and we have found a variation of the Kelvin waves. This instantaneous example may be compared with the sketch of a photograph (figure SI-IA-1) of the steady hydropower intake at the mountainous lake at Horspranget, Sweden, due to Rahm (1953), where the scales are of geophysical proportions. Both have similar feathered divergent waves and an arched Kelvin envelope.

In figure SI-TA-1, the estimated λ_g is $c(2/3)$. The dispersion relationship, $\lambda_g = 2\pi U^2 (\cos \theta)^2 / g$ gives $U = 1.0$ m s^{-1} for $\theta = 0°$. This is the maximum value of U at $f = 1.25$ Hz. This value of U is close to the maximum foil velocity $V = 2\pi fr$, where for $f = 1.25$ Hz, average foil radius of 0.15 m, $V = 1.18$ m s^{-1}. The value of U would be lower at $f = 0.75$ Hz and 1.00 Hz in the ratio of f^2. Write $Fr = U/\sqrt{(gL)} = \sqrt{(\lambda_g/(2\pi c))}$, where L is a length scaled to c for maximum blockage, λ_g is the wavelength, c is the chord length and U is the longitudinal velocity of the foil had there been no flow. The foil is a point source of pressure, and, theoretically, a sailboat is like a point source of pressure being dragged in a channel at a velocity of U, which gives rise to the Kelvin arch. A Kelvin-arched envelope is produced at $f = 1.25$ Hz only at one instant of time when $Fr = 1.0$.

3.1.2. *Capillary waves*

In figure SI-TA-2, the foil stem is started impulsively. The radially propagating capillary waves emerge at 1.20 s only when pitching is added to the rolling motion. More waves appear with time as in internal gravity waves in stably stratified fluids (equation (10) in Mowbray 1967; Movie 1).

Figure 1(e) shows standing waves in the funnel of the scale of the foil chord growing from the radiating capillary waves. The waves stand because the opposing wave speeds are equal in amplitude (Currie 1993). Many wavelengths are produced, but the apparatus allows the selection of some of them.

A tuning fork in water produces similar capillary waves that do not last beyond a few centimetres (Lighthill 1978, p. 225). The roll motion did not produce these waves. Since the surface waves in figure SI-TA-2 are like ripples (i.e. short wavelength <0.07 m), surface tension is the only force restoring flatness. The capillary waves described here are not purely gravity waves. Still, for sinusoidal waves of wavenumber k, surface tension (T) effects can be replicated exactly by slightly increasing the acceleration due to gravity g by $\rho^{-1}Tk^2$ (Lighthill 1978, p. 223), where $T = 0.074$ N m^{-1}, $\rho = 1000$ Kg m^{-3}. If $k = 1/0.07$ m^{-1} (stem circumference is $0.0254\pi = 0.08$ m, which is at the upper edge of being a ripple), the incremental effect on g is 0.015 m s^{-2} (= 0.1 %). Hence, since the constant phase rays are gravity waves, they agree remarkably with the schlieren pictures of gravity waves (see figure SI-TA-3($c1$–$c3$) in a laboratory stratified brine solution of uniform Väisälä–Brunt frequency (Mowbray 1967; Stevenson 1968)).

3.2. *Bursting of the 'disturbed-laminar' contra-rotating double helix root vortex*

Figure 2 shows an aerated DH of contra-rotating vortices of the DL type at $f = 1.0$ Hz. While winding, first it inclines exactly to 45° to the vertical (β) in panel (1),

the pointed apex being buckled by compression load P_c. In (2), barely higher than 45°, it starts to unwind, spreading immediately laterally in the inner half, but collapsing in the outer half. In (3), it contracts laterally, disintegrating into bubbles. In (2), the pitching motion has removed the foil obstruction in (1). The vortex motion correlates with the axial adverse and favourable pressure gradients imposed by the pitching motion. Measuring from the vertical, the vortex slant increases while the length of the vortex increases between (1) and (2) indicating vortex stretching. There are two stages of bursting: an unwinding and a disintegration into bubbles. Each correlates with the relaxation of the stretching. Comparison of (1) and (2) shows that the sudden vortex relaxation produces amplified vertical oscillations of the free surface. This oscillation occurs prior to the disintegration into bubbles in (3). There is a time delay between the vortex oscillation when released from stretching and the disintegration into bubbles. The vertical oscillation is spread over an axial length of λ, the DH wavelength. The vertical oscillation of the free surface is evidence of vortex oscillation when released of stretching. A monochromatic compression and rarefaction wave train will be produced.

The DH originates from the necklace vortex around the stem (figure 3). Out of the two branches, one dominates (Movie 2). The DH mode does not rotate after unwinding when the effect of pitching is no longer present. It is discussed later that the vortex stretching reaches the maximum value at $\beta = 45°$. The vortex is stable for $\beta \leqslant 45°$, but unstable for $\beta > 45°$. Here and later, the demarcation becomes clear by observing where the bubbles are rare and where there is a preponderance of bubbles, respectively.

The narrow tip of the vortex buckles under compression load P_c (panel 1) because the compression stiffness exceeds the bending stiffness in the aerated elastic vortex. Using the grid on the foil surface, the helix pitch in (2) is $(\delta_1/2 + 2c/3)$, and the helix spread is $2c/3$, where c is the foil chord length and δ_1 is the foil stem diameter (see the inset (figure 2(4)) in figure 2(2)). The helix spread is zero in the outer half in (2) where the bursting has commenced. The bursting spreads later to the inner half in (3) where the helix spread is nearly zero. The foil pitches along the stem axis at a distance of $c/3$ from the foil leading edge. Hence, $2c/3$, the maximum pitch radius, is the length scale of the helical mode of the instability in the root vortex that is amplifying. The effective maximum blockage width is $2c/3$, not c (see examples in figures SI-IA-2 and SI-IA-3). The unwound vortex bursts (panel (3) in figure 2) when the foil starts to increase the blockage again at $\phi = 105°$. The disintegration into bubbles proceeds from the tip of the helix to the foil root (figure SI-IA-4). The bubbles formed have low inertia and show a tendency to remain clustered along the DH. Some spherical bubbles are formed, but they remain coalesced and not fully separated.

The inset in figure 2(3) shows the schematic of the mechanism of bubble formation. The stretched vortex tube is observed as suddenly released. Standing spiralling waves of wavelength λ_d are produced. The red and blue arrows show waves rebounding from the opposite ends of the aerated vortex tube. Ringing bubbles of diameter d are produced. Here, c_1 is the speed of sound in water. Later, it is shown that the vortex inclination rises from 0° to 45° when stretching and turbulence amplification are maximum. The sudden release of the maximally stretched vortex tubes produce three ringings of wavelength λ, λ_d and d. Here, λ is the aerated DH wavelength, λ_d is the wavelength of the standing waves (see the inset in figure 2(3)), and d is the bubble diameter. Since the vortices receive orthogonally oscillating inputs of torque and there are two preferred orthogonal directions of organization in the shear flow

(Head & Bandyopadhyay 1981), the bubbles can be expected to undergo resonant oscillations. The synchronized vertical oscillation of the free surface is an evidence.

Write that the wavelength $\lambda \propto d$ and its values are functions of f (to be modelled later). We estimate that the DH wavelength $\lambda = 20d$–$30d$. One turn of the bubble gives $\lambda_d = \pi d$. We get, $\lambda = 7\lambda_d$ to $10\lambda_d$. The inverse of the time scales (s^{-1}) are c_1/λ, c_1/λ_d and c_1/d, where c_1 is the speed of sound in water, 1435 m s^{-1}. At $f = 1$ Hz, $\lambda = 0.13$ m, $\lambda_d = 0.019$–0.013 m and $d = 0.006$–0.004 m. We expect spectral peaks of sound level at 11, 75 and 239–359 kHz. The lower range overlaps the buoy measurements in sea due to breaking surface waves (figure 1 in Nystuen 2002). The measurements do not extend above 50 kHz. At $f = 1.25$ Hz, the wavelengths and bubble diameter are smaller. The breaking wave sound measurements may be from the ringing of the aerated vortex tubes and the induced oscillations of the free surface and not from the bubbles. Buoy measurements above 50 kHz are needed. The mechanism of bubble formation from the bursting of the aerated root vortex may bear relevance to bubble formation due to breaking waves due to winds of 6–10 m s^{-1}. The upper limit of noise due to the collective oscillation of bubbles of the vortex tube is at least 11 kHz and not 1 kHz (Prosperetti 1988).

Figure 2(2) marks the location of vortex breakup where the opposing vorticities cross. Panel 3 shows that the fine bubble DH pattern from the foil is fusing with the main DH at the location of the vortex breakup. The fusing point is a vortex crossing point of the arms of the $\pm\Gamma$ DH (Γ is circulation).

3.3. *Synthesis of the motion of the 'disturbed-laminar' contra-rotating double helix root vortex*

The physical processes in figure 2 are shown in figure 3. The streamlines, representing convection of vorticity, and the critical points (saddle points S_1, S_2) for figure 2 are sketched in figure 3(a) (Baker 1979; Chong, Perry & Cantwell 1990). The upstream lateral vorticity bends to form two horseshoe vortices of size c (figures 2, 4a, $f = 1$ Hz) and δ_1 (figure 4d1, $f = 1.25$ Hz). Saddles like S_1, are created. The right side of the figure shows the critical point of the cross-section of the dominant wound asymmetric horseshoe vortex in the near wake. The cross-section has saddle points (S_2) where stretching takes place amplifying turbulence. The vortex stretching is due to an axial velocity U_a which is the β-component of U_{ext} that creates the vertical shear in the wake (figure 3a, inset 2, and figure 3b; Bandyopadhyay 1980).

In a cylindrical gas–liquid separator (length L, diameter D) which has a tangential entrance and exit, an aerated core vortex is formed that stands. A rectilinear vortex spirals when the ratio $L/D = \pi$, 2π or 3π (see figure 3 in Bandyopadhyay & Gad-El-Hak 1996). This positioning allows, between the ends, an axial spacing of $L/D = N\pi$, where N is an integer $1, 2, 3, \ldots$. The root vortex is anchored at the root and the other end experiences a compression, making the geometry essentially confined. Hence, the aerated root vortex is also standing. Assume D is spiral diameter and vortex diameter d_v is proportional to D. With increasing Re, if L is constant, then, N will increase with drop in spiral diameter D. Compare figures 9(b) and SI-IA-2 at $f = 1$ Hz with 4(d1) at $f = 1.25$ Hz. For the similar cylindrical lengths of 8 cm, D is 2 cm versus 1 cm, N is 1 versus 2, respectively. The vortex diameter also drops with increasing N.

The aerated vortex has structural properties such as compression (K_c) and bending (K_b) stiffness. If $K_c > K_b$, the vortex will buckle. In both figures 2(1) and 6(b) the buckling moves toward the stable zone of $\beta \leqslant 45°$. In figure 2(1), $f = 1$ Hz and the centrifugal force is lower and the buckling creates a zig-zag shape. However,
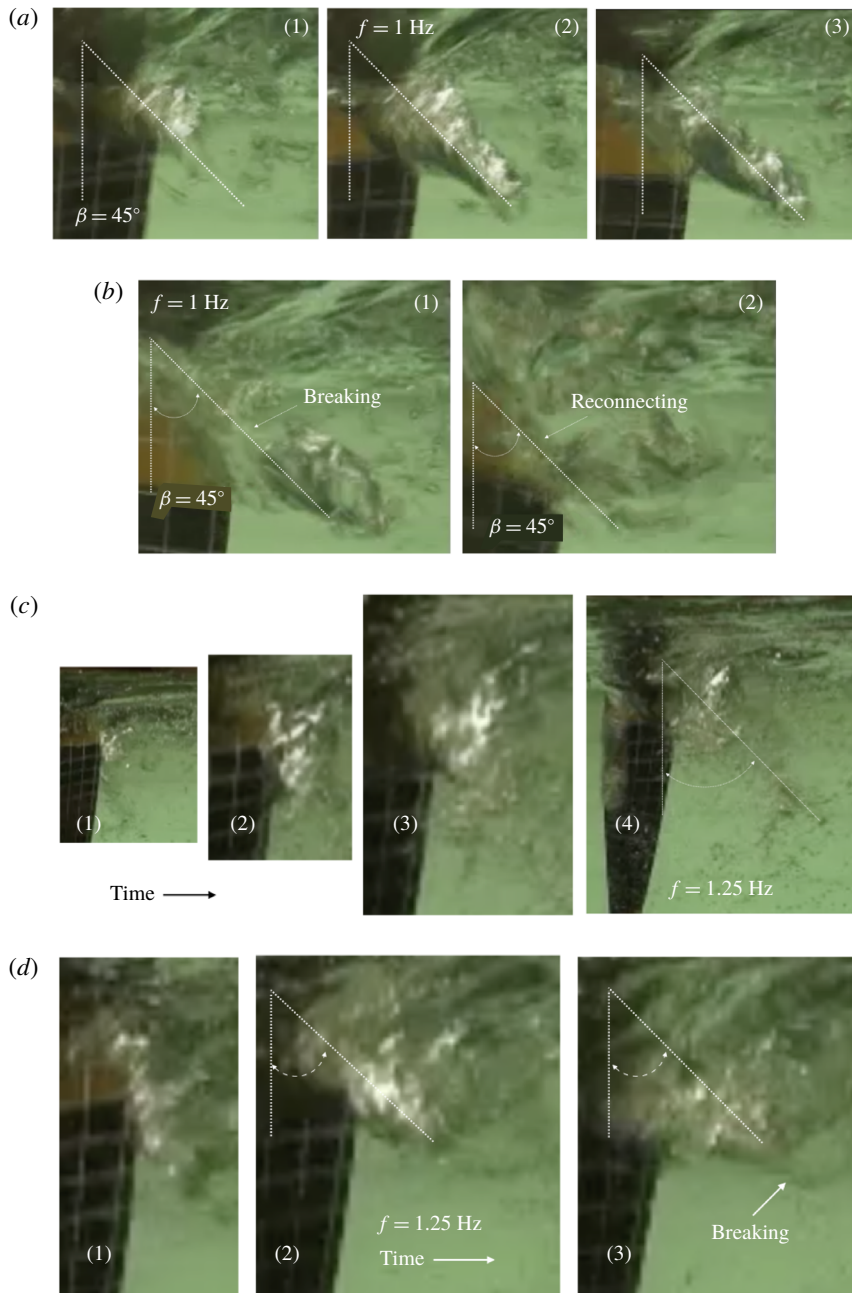
FIGURE 4. Vortex slant β increases to the angle of principal strain (45°) when vortex stretching and turbulence amplification become maximum and the vortex bursts. (*a*) Examples of the maximum vortex stretching just prior to bursting; also see figure SI-IA-3 in SI. (*b*) Vortex slant at the time of (in 1), and after bursting (in 2). (*c*) The increasing slant β of the root vortex before (in 1 to 3) and at the time of bursting (in 4) can be seen. (*d*) A multi pitch thin double helix grows and slants to 45° in the time step of mere 0.03 s (1 and 2) and bursts (in 3). The acute angle subtended by the thin dotted lines represents a slant β of 45° to the vertical direction. The nominal external flow is left to right.

in figure 6(*b*), $f = 1.25$ Hz, the centrifugal force is higher and the buckling makes a toroid. The differences in buckling are due to differences in K_c and K_b. The difference in fact proves that the vortex is an elastic structure. The example of the toroidal buckling for high centrifugal forces will be considered again later in figure 6(*b*2). The compression stiffness increases because surface tension acts to reduce the surface area of the vortex to counter the centrifugal force. At $f = 1$ Hz, the root double spiral has one full turn (of the π-type) in figures 2, SI-IA-2 to SI-IA-4 and 9(*b*). At $f = 1.25$ Hz, the number of full turns may be 2 (of the 2π-type) in figure 4(*c,d*). Therefore, the apex of the vortex is a stagnation point for the wave to be standing. The vortex breakup at the apex is a stagnation point (Saffman 1990). We are seeing evidence of elasticity of an aerated vortex. Therefore, the root vortex is a standing vortex. Extending this result for increasing N, the standing DH appears as contra-rotating Taylor cells (see figure 9*e,g*).

The funnelling and entrainment of air along the stretched vortex axis are shown in figure 3. When the DH in (*a*) unwinds (*b*), the free surface oscillates vertically over an axial length of λ, the wavelength of the unwound DH (figure 2(2)), radiating noise. The lateral oscillations of the vortex tube, that start when the vortex is suddenly released of the axial stretching, also oscillate the local air–water interface radially within the vortex tube to form the bubbles. In figure 2 between panels 2 and 3, the bubbles take 0.125 s to form after the onset of the oscillations of the interface. This time scale is a 40 Hz bubble oscillation if five damped oscillations are present as is common in spring, mass and damper analogues (Bandyopadhyay 2019).

In figure 2(2), there is a narrowing where the two arms of the DH meet with vorticities ($\pm\omega$) that viscosity acts to cancel. The vortex breaks at this location (Saffman 1990). After the pitching blockage begins to relax at $\beta = 45°$, $\beta \rightarrow 90°$, $(V_{\theta 1}, V_{\theta 2}, V_\theta) \rightarrow 0$, $U_a \rightarrow U_{ext}$, and the vortex bursting, indicated by the turbulence of the bubbles, proceeds towards the root. How Kelvin waves produced at the tip initiate the bursting is shown later. The bubbles form in the air tubes when stretching is suddenly released.

Downstream of the intermittent turbulence patches, conical relaminarescent regions have also been reported in the so called 'puffs' of transitional pipe flows (Bandyopadhyay 1986) and in the turbulent trailing vortex cores (Bandyopadhyay *et al.* 1992) just as in the conical relaminarescent vortex tip in figure 2(2). It was shown in Bandyopadhyay *et al.* (1992) that the puff flow and the trailing vortex contain helical motions which certainly is the case in figure 2.

3.4. *The* 45° *vortex slant at the time of bursting*

In figure 2(1) at $f = 1$ Hz, the vortex slope β was 45°. In figure 4, $f = 1$ Hz in (*a,b*) and 1.25 Hz in (*c,d*). Angle β increases to 45° until the root vortex bursts. In the examples from different cycles in figure 4(*a*1–*a*3), $\beta = 45°$. Such well-formed root vortices are not seen for $\beta > 45°$. In figure 4(*b*), the vortex is about to burst in (1), when still at $\beta = 45°$; but in (2), the vortex has burst and the slope $\beta > 45°$.

Figure 4(*c*) shows an example from the same vortex of the time sequence of increasing β until bursting at $\beta = 45°$. Figure 4(*c*1) shows a small diameter DH wound to a nearly vertical cone at $f = 1.25$ Hz. This vortex radially enlarges initially but without increasing β. Its slant increases in (3) while also enlarging. In (4), while still at $\beta = 45°$, the vortex has just burst. Figure 4(*d*) shows a long cylindrical DH of uniform diameter at $f = 1.25$ Hz at a shallow angle of β in (1), rising to 45° in (2) and bursting in (3). In (*c*), the starting DH is conical and shorter in length. There are more modes of DH at the root at $f = 1.25$ Hz.

The root vortex slant β increases to 45° when bursting occurs (figures 4, 6 and 7). The slanting of the Taylor tubes (figure 9) are close to 45° without much variation. In figure 4(*c*,*d*), the Taylor tube slanting approach 45° before the root vortex axis does. The vortex tubes of the foil-tip flow reach a straight slant of 45° to the external stream (figure 11). The knotting of the tip of the DH in the final stages of bursting is also into a cone of 45°, slanted at 45° (figure 7(*a*6), (*a*7), (*b*3)). There is a wide prevalence of the 45° slant of the vortex tubes just prior to bursting.

The vortex inclinations of 45° have been visualized in a wide range of *Re* in turbulent boundary layers by Head & Bandyopadhyay (1981), confirmed by particle image velocimetry by Adrian, Meinhart & Tomkins (2000) and also by direct numerical simulation at low Reynolds numbers by Wu & Moin (2009).

Consider a parallel shear flow invariant with distance. Concentrations of vorticity can appear only when a periodic disturbance is superimposed. As per Theodorsen's thesis (1952), these concentrations of vorticity will die down unless there is some existing three-dimensionality. If the flow is three-dimensional, and some vorticity is present, turbulence can be produced from the vorticity only if it is stretched. In a turbulent boundary layer, which happens to be three-dimensional, Theodorsen (1952) predicted the appearance of horseshoe vortices at 45°. These arguments apply in the present case.

The three-dimensionality introduces a term $\omega_i \omega_j \partial u_i / \partial x_j$ in the vorticity equation which implicitly expresses the effects of stretching which must precede and accompany the production of turbulence (Head & Bandyopadhyay 1981). Multiplying the vorticity equation by ω, a vector in (x, y, z), in tensor notation, we get $D/Dt[1/2 \omega_i \omega_i] = \omega_i \omega_j \partial u_i / \partial x_j + \omega_i \nu \nabla^2 \omega_i$, where ν is kinematic viscosity. If the vorticity vectors in a concentration of vorticity are $(\omega_x, \omega_y, \omega_z)$, since $\partial u / \partial y$ is greater than any other component, the stretching term is approximated to $\omega_x \omega_y \partial u / \partial y$. This term will be a maximum when the component of the vorticity vector in the (x, y) plane is at 45° to the main flow direction. In a horizontal shear flow, the downstream angle of 45° represents the direction of principal axis along which the strain is of pure extension and the rate of stretching is at maximum. The abrupt drop in the external velocity when the foil blockage is removed eliminates the term $\partial U / \partial y$ making the stretching term vanish in the vortex tubes. This event produces axial and radial waves in the tubes precipitating the bursting and bubble formation.

Significantly, in four sets of examples of the present work, the varieties of vortices have this inclination of 45° to the external flow just prior to bursting. The root vortex slope β is given by the opposing effects of axial stretching on the induced velocity and the external shear. See Bandyopadhyay (1980), where this balance accurately gives the slope of the arrays of vortices formed sequentially in a turbulent boundary layer large structure. The velocity balance is shown in figure 3(*a*, inset 2). The wall-normal shear tries to rotate the horseshoe vortex in the boundary layer back, parallel to the wall (see figure 33 in Head & Bandyopadhyay 1981). Similarly, in the present flow, the direct effect of the shear tries to rotate the root vortex horizontally along the flow direction near the free surface. As β increases from 0° to 45°, the stretching increases to the maximum value. The increased induced velocity then resists the direct effect of the shear exactly. At $\beta = 45°$, the vortex is in neutral equilibrium. It is sensitive to disturbances and is prone to breakdown. The root vortex therefore is stable in the range $0 \leqslant \beta \leqslant 45°$. However, for $45° < \beta < 90°$, the stretching drops and there is nothing to resist the shear whereby β rapidly approaches 90° (figure SI-IA-4). In support of this argument, we do see a preponderance of pre-burst root vortices for $0 \leqslant \beta \leqslant 45°$, but no pre-burst vortex is seen at $45° < \beta < 90°$. Since bubbles can form

only where the vortex is unstable, they are confined to $45° < \beta < 90°$ and virtually none will appear where $0 < \beta < 45°$. The regions where β is stable and unstable are shown schematically in figure 3(*a*). The statement on the relationship of bubble formation and vortex instability is confirmed in figures 6(*b*) and 8(*b–d*).

Figure 6(*d*) and Movie 3 at a time stamp of 01:58 (m:s) show that a single coiled vortex, marked V, migrates on the pressure side after formation, shown in panel (1). It shows up over the leading edge from the pressure side in panel (4), stretching at 45° in (5). The pressure side vortex V bursts at the same time as the suction side root vortex. Here also, the 45° slope demarcation of stability exists and the unstable zone is complementary. The movie shows that, over time, the 45° unstable front of the coarse bubble filled region over the foil coming from the pressure side, advances diagonally upward and right toward the standing lower edge of the unstable region of the root vortex closing the bubble-free alleyway shown in figure 6(*b*2). In this manner, the advancing unstable region of the pressure side joins up with that of the suction side obliterating the intervening stable region. Finally, one could also argue conversely that since the bubbles are formed only in certain triangular sectors, the vortex must be unstable only there.

3.5. *Modelling of the nonlinear vortex lift of the root vortex*

Figure 5 draws an analogy between the delta-wing high lift leading edge vortex and the root vortex. Both are produced by salient edge separation. The lift producing the root vortex is estimated in the following manner. The hydrostatic pressure p increases with depth y. Therefore, the vortex grows axially in an adverse pressure gradient $\partial p / \partial y > 0$, the depth acting like a diffuser. The vortex bursting experiments by Sarpkaya (1995) and the Kelvin wave vortex experiments by Tsoy *et al.* (2018) have been carried out in small angle diffusers. While pitching up or down in continuously pitching delta wings, the bursting occurs farther back or forward compared to the steady case, respectively. There is hysteresis in the measurements of lift compared to the steady state case (Heron & Myose 2009). The unsteady measurements of lift force in a flapping foil in the absence of any air entrainment show a similar hysteresis with quasi-steady models (figure 7 in Bandyopadhyay *et al.* 2008*a*). For these similarities, as shown in figure 5, an analogy is drawn between the root vortex and the leading edge vortex of an asymmetric delta wing with salient leading edges. The vortex in the inset in figure 5 is from figure 2(1).

The vortex lift model makes no distinction between the DL and the turbulent root vortices. The root vortex is generally conical with the apex pointing diagonally downward. Since the foil input torque does not change cycle to cycle, the lift values are assumed to be similar to those modelled here. Measurements on flapping foils show that lift force coefficient $C_L \propto f^2$ (Menozzi *et al.* 2008). Equation (2.6) is used to model the linear and nonlinear components of the force, the variation with β, and the nonlinear vortex lift just prior to bursting when $\beta = 45°$.

Unsteady lift measurements in flapping foils can be modelled by assuming the flow to be quasi-steady (Bandyopadhyay *et al.* 2008*a*). Define the aspect ratio (A) of a delta wing as b^2/a_w, where b is the wing span and a_w is the wing area. Theory and measurements of lift forces in steady delta wings in figure 12 in Polhamus (1966) show that the vortex lift in a delta wing is a function of A and the AOA β. Consider using equation (2.6), where the total lift $C_L = C_{LP} + C_{LV}$ where C_{LP} is the linear part of wing lift obtained by potential flow method and C_{LV} is the vortex lift component, which is nonlinear. See inset 2 in figure 5. For $A \to 0$, $C_{LV} \to 0$ and $C_L \to C_{LP}$.
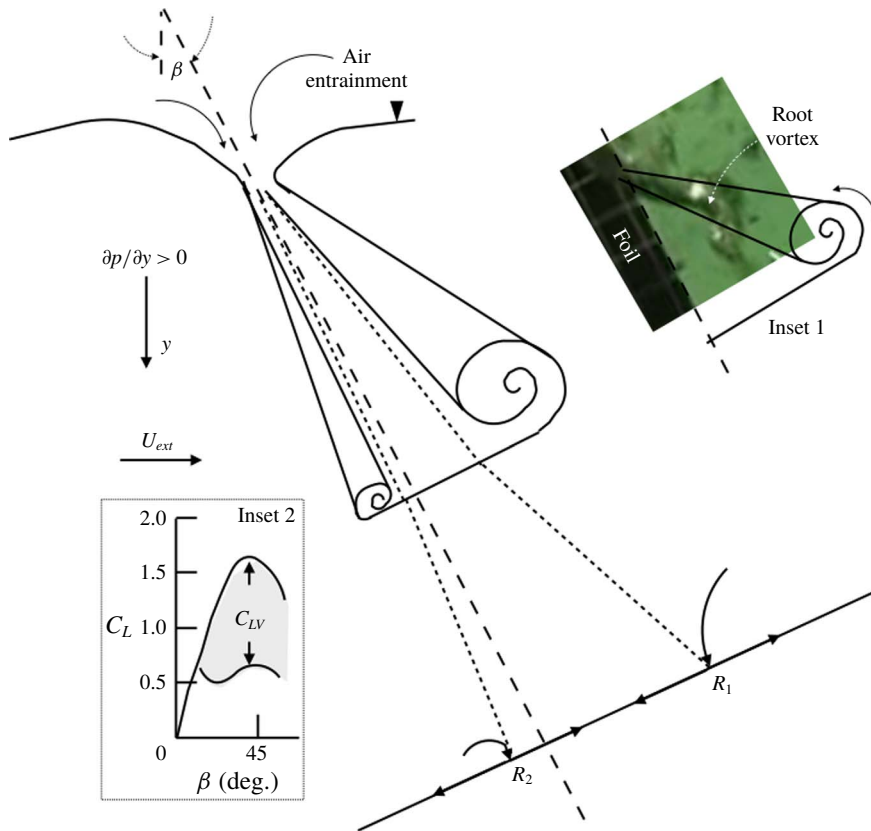
FIGURE 5. Modelling of the root vortex lift based on the analogy of delta wing vortex lift. Inset 1: pre-bursting root vortex in figure 2(1) superimposed on the schematic of the delta wing leading edge vortex. Inset 2: quasi-steady model and measurements showing nonlinear vortex lift C_{LV} (Bandyopadhyay *et al.* 2008*a*).

To make the vortex predominantly one sided, the delta wing in figure 5 is shown asymmetric, since smaller values of A produce lower values of lift. We assume that the asymmetry is large and the entire lift force can be attributed to just one edge. It is assumed that the vortex slant is the same as the angle of attack of the delta wing. The maximum value of C_L and C_{LP} at an angle of attack, say β of 25°, increases with A. But C_{LV} does not change much between the A values at the same AOA. The difference is understandable because the nonlinear vortex lift is not produced by the foil area. It is produced by the salient edge and β. The potential flow lift is produced by the source–sink distributions over A and β. For example, at $A = 0.5$ and $\beta = 25°$, $C_L = 0.7$ and $C_{LP} = 0.24$, giving $C_{LV} = 0.46$. At $A = 1.5$ and $\beta = 25°$, $C_L = 1.1$ and $C_{LP} = 0.62$ giving $C_{LV} = 0.48$. Hence C_{LV} trend with A and β is universal: C_{LV} increases with β, but is independent of A.

The value of A determines C_L, C_{LP} and C_{LV}. In figure 6(*a*1), $b = c$ and $a_w = c^2$, giving $A = 1.0$. For $\beta = 15°$, $C_L = 0.5$, $C_{LP} = 0.35$, giving $C_{LV} = 0.15$. For $\beta = 25°$, $C_L = 0.90$ and $C_{LP} = 0.45$, giving $C_{LV} = 0.45$. The vortex lift due to the root vortex in figure 6(*a*1) is then 0.45 – the linear and nonlinear components of lift are the same. When entrainment is prevented, these values are close to our unsteady flapping foil lift measurements (figure 9 in Bandyopadhyay *et al.* 2008*a*). Hence, to estimate C_{LV} alone,
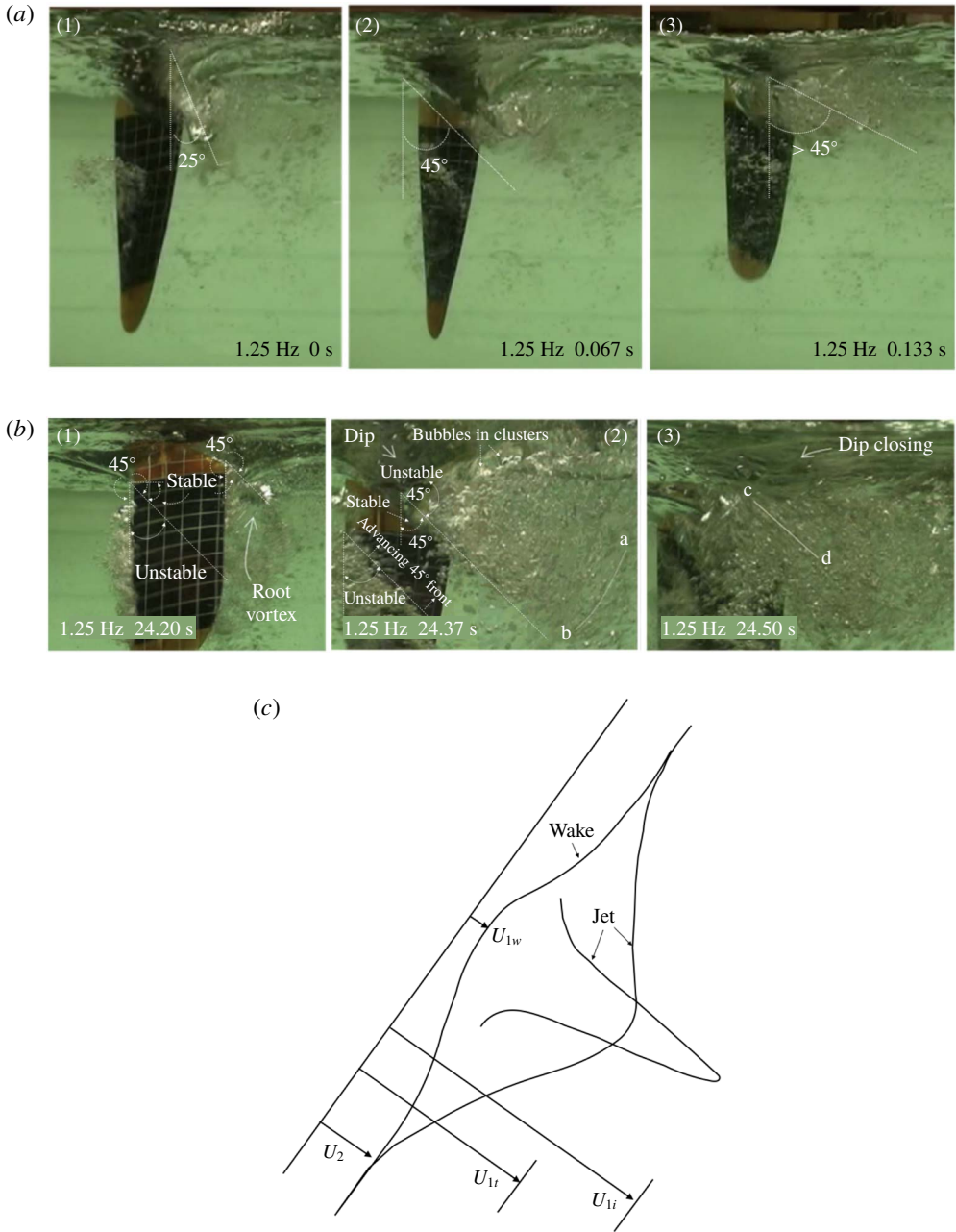
FIGURE 6. For caption see next page.

figure 9 in Bandyopadhyay *et al.* (2008*a*) may be used since the present apparatus uses the same flapping foil and the delta wing analogy need not be invoked. The suction lift analogy gives the origin of the root vortex a theoretical foundation and helps to isolate the origins of the linear and nonlinear lift forces.

As per the measurements in figure 9 of Bandyopadhyay *et al.* (2008*a*), the nonlinear vortex lift in the root vortex of 1.0 would be achievable at $\beta = 45°$ when the vortex
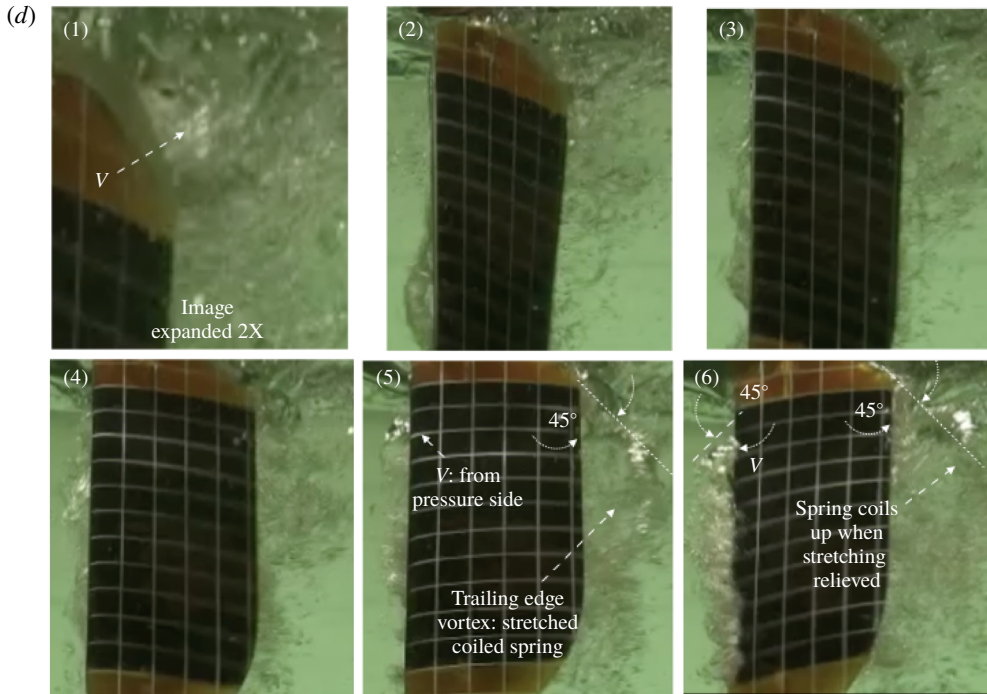
FIGURE 6. (cntd). Sets of three images each of two examples of turbulent vortex bursting (*a*,*b*) and the schematic (*c*) of variations in velocity profiles across the vortex axis from jet to wake with changes in blockage. Panels *b*1 and *b*2: rotational effect (marking a to b); panels *a*2, *a*3 and *b*3: 45° slope shows maximum axial stretching. The tiny aerated Taylor cells in the root vortex are normal to the 25° slope in *a*1, and normal to the 45° slope in *b*1 and in figure 9(*e*). (*d*) Sequence of successive frames explaining how the compact vortex in (*b*) is formed from the stretching and relieving of the trailing edge vertically coiled vortex in panel (5); also shows the migration of the vortex V in the pressure side. In (*a*), relative phase of $\phi = $ (1) 0°, (2) 30°, (3) 60°. In (*b*), relative phase of $\phi = $ (1) 0°, (2) 76.5°, (3) 135°. Foil parameters are $\phi_o = 40°$, $\theta_o = 45°$, $\theta_{to} = 75°$, $f = 1.25$ Hz, $\psi = 90°$.

is about to burst. In figure 6(*a*), $\beta = 25°$ at vortex formation and $\beta = 45°$ at bursting, being horizontal after bursting.

Figure 9 in Bandyopadhyay *et al.* (2008*a*) shows that the scatter in the lift measurements is higher at AOA of 45° and −45° and negligible at other AOA. The $\beta = 45°$ slope of the root vortex, which is the boundary of the stable and the unstable postures, is a neutral equilibrium posture, and cannot be held there for long. Angle β increases rapidly after 45° because shear rotation is not counteracted.

The 'reattachment lines' (R_1 and R_2) of the wound vortices shown in figure 5 would be saddles assuming mirror images of induced flows in the water. Vorticity stretching is taking place along the downward line of the saddle points whereby entrainment and rotational velocity are being accentuated.

The generally tapering shape of the DH root vortex (figures 2(1), 4, 9*g*,*i*,*n*) in the stable region where $0° \leqslant \beta \leqslant 45°$ is set by the balance between the centrifugal force Γ_c of the vortex and the force of radial pressure (difference) gradient P_r. In this region, at a given β, stretching is constant, hence Γ_c is constant with length, but P_r increases

with depth. With increasing depth, a cone is produced. At the point where the DH crosses, Γ_c drops to zero because the opposing vorticities ($\pm\omega$) cancel each other (Saffman 1990) causing vortex breaking and reconnection. In the unstable region $45° > \beta \geqslant 90°$, as Γ_c drops with loss of stretching, $P_r > \Gamma_c$ crushing the vortex radially inwards continuing toward the root. In panels (2, 3) of figure 2, β in panel 3 is greater than in panel 2 which lowers the stretching (by 11 %) and Γ_c. The two arms of the unwound vortex do collapse closer to the axis, first in the outer half in panel 2, and then in the inner half in panel 3. In the vortex, breakdown proceeds toward the root and radially inward.

At $\beta = 45°$, $U_i = U_a$. The velocity of the external flow is set by ϕ and a disc model shows that $U_{ext} = 0.08$–0.09 m s^{-1} (Bandyopadhyay 2015). Taking the component of U_{ext}, the value of U_a and U_i rise to 0.06 m s^{-1} at $\beta = 45°$.

Rossby number Ro is estimated as follows. Ascribe the axial velocity in the vortex to $\dot{\phi}$, which produces the foil load and U_{ext}, and the rotational velocity to $\dot{\theta}$. Define Ro as the ratio of the inertial to the Coriolis force components as $Ro = U_{ext}/V_{\theta max}$. The maximum azimuthal velocity of the vortex $V_{\theta max}$ is $2\pi fr$, where the pitch radius r is $2c/3$. For $c = 0.10$ m and $f = 1$ Hz, $V_{\theta max} = 0.419$ m s^{-1}. If the inertia force is given by 0.085 m s^{-1}, then $Ro = 0.203$. This estimate matches the value of 0.20, the critical value when the 'dramatic' formation and bursting of small vortices occur in a large rotating flow ascribable to the interaction between spiralling waves (Hopfinger *et al.* 1982).

3.6. *Modelling of the bubble diameter*

Consider the scaling law of the bubbles. Movie 3 shows a large drop in the bubble diameter with increasing torque input into the vortices from $f = 1$ Hz (figure 2) to 1.25 Hz (figure 6). The effects can be seen in the reductions in the diameters of the individual arms of the DH vortices in figures 2 and 4($c1,c2$). The DH is formed as the foil undergoes $\partial\theta/\partial t$ motion at the origin of the coordinate system in the inset of figure 6(a) where the foil pierces the surface. Increasing centrifugal force (N) lowers the vortex core pressure p (N m^{-2}). The pressure of the surrounding water at the same depth lowers the diameter of the tube and of the bubbles d (m). Surface tension γ (N m^{-1}) balances the pressure. The length scale of the vortex and bubble diameters is γ/p (m). The scaling parameter (N_b) of the bubbles is

$$N_b = pd/\gamma. \tag{3.1a}$$

The velocity scale (m s^{-1}) is Γ/d (m s^{-1}), where Γ (m^2 s^{-1}) is circulation. The bubble scaling parameter (N_B), in terms of $V_{\theta max}$, is

$$N_B = \rho V_{\theta max}^2 d/\gamma. \tag{3.1b}$$

Here, $V_{\theta max}$ (m s^{-1}) is the maximum rotational velocity in the vortex and ρ (kg m^{-3}) is density. At $f = 1$ Hz, $V_{\theta max} = 0.42$ m s^{-1}, $d = 0.005$ m, $\gamma = 0.072$ (N m^{-1}), $\rho = 1000$ kg m^{-3} and $N_B = 12$. At $f = 1.25$ Hz, $V_{\theta max} = 0.523$ m s^{-1}, $d = 0.003$ m and $N_B = 11.3$. With the limited data and the uncertainties in the estimation of d, $N_B = \rho V_{\theta max}^2 d/\gamma = 11$ to 12.

Figure 6(b) is a limiting case of the model. The vortex of Kelvin mode $m = 0$ has too small a diameter to be visible. (Figure 9(i) shows an example of the abrupt reduction in diameter.) The hydrostatic pressure is larger down span. The vortex core is compressed. The pre-bursting high circumferential velocity is obvious post-bursting.

From the core, the bubbles are thrown out in an arc of 70° at the foil roll velocity of the local span. The bubbles formed are most numerous per unit surface area and also the smallest observed out of all cases. In (3.1*b*), the bubble diameter is inversely proportional to the square of the circumferential velocity. Qualitatively, the model extrapolates to figure 6(*b*).

3.7. *Bursting of contra-rotating turbulent vortex*

Two examples of turbulent vortex bursting at $f = 1.25$ Hz are shown in figure 6 and may be contrasted with the DL case in figure 2 at $f = 1.0$ Hz. A root vortex of shorter length but larger diameter is formed. Along its axis, the tightly wound vortex has an array of small diameter, parallel Taylor–Couette roll cells. (The curved surface of the air tubes acts as a lens producing the white lines.) As shown in figure 6(*a*1,*b*1), these are tubes of air: the conventional cylinders have been substituted by the surrounding rotating water and the inner air core. See the schematic in figure 6(*c*) for the velocity profiles inside and outside the root vortex structure corresponding to figures 6(*a*1–*a*3) and 6(*b*1–*b*3) following Batchelor (1967). The Reynolds number is higher than in figure 2. The DH unwinding is not obvious. The free surface shows a dip as in a funnel, and there is an abrupt breakdown into bubbles aligned in a circumferential trajectory marked 'a–b' in figure 6(*b*2). As the blockage is reduced further, the surface dip closes (figure 6*b*3) and the bubbles become aligned radially at 45° to the flow direction (marked 'c–d'; see figure 6*b*).

Figure 6(*b*) shows that the bubbles formed after bursting lie where $45° < \beta \leqslant 90°$ and hardly any where $0° \leqslant \beta \leqslant 45°$. These coincide with the regions where β is unstable and stable, respectively. Over $45° < \beta \leqslant 90°$, there is a declining force of the induced velocity of the vortex available that counters the shear – a negative feedback loop. The mean shear time scale is $(\partial U/\partial y)^{-1}$, and the vortex time scale of induction is $(\partial V_\theta/\partial r)^{-1}$, where V_θ is the rotational velocity of the vortex and r is the radius. Here, $(\partial V_\theta/\partial r)^{-1} \ll (\partial U/\partial y)^{-1}$, changing to $(\partial V_\theta/\partial r)^{-1} < (\partial U/\partial y)^{-1}$. This change exists because the exiting bubbles are carrying away the compressed elastic energy, which serves as the main source of energy. This mechanism would explain the short time scale of the bursting. The time interval between panels 1 and 2 is 0.17 s, whereas the quarter of the foil oscillation time scale is 0.2 s (= the stretching duration) and the mean $(\partial U/\partial y)^{-1}$ is approximately 1.5 s. There is a cumulative depletion of the reserve vortex kinetic energy remaining over the duration of bursting. Recall equation (1.3) where ν is absent; and dissipation, being a slow process, can be neglected. The bubbles are being released gradually as the β of the weakening vortex approaches 90°. The arc 'a b' in figure 6(*b* panel 2) is created through this process.

The horizontally lying bright groups of individually identifiable tubes near the root are segments of the root vortex which release bubbles later. Over $45° < \beta \leqslant 90°$, the oscillating vortex breaks into axial segments. Bubbles are released, not from the entire length simultaneously, but in about six to ten axial groups over an arc of 70°. (Unlike in the turbulent boundary layer analogy in Bandyopadhyay (1980) where there is a solid wall, here, the vertical oscillation of the free surface allows β to go beyond 90° to 115°.) The time scale of the bubble release is assumed to be given by the time it takes for the vortex to change its slanting by 7°–12°. The bubble release time duration from the compressed aerated vortex is estimated to be $(0.17$ s$)/6 = 0.03$ s to 0.02 s, approximately 1/10th or less of the stretching duration. This release signifies that as the balance between the centrifugal force and the surface tension is disturbed, the bubbles would experience resonant oscillation and radiate sound.

The schematic in figure 6(*c*) shows four velocity (*U*) profiles to relate the vortex state to the changes across the vortex axis from jet to wake with changes in blockage. Also see Movie 3 in the SI. The early understanding of vortex bursting was based on the distribution of velocity profiles as in figure 6(*c*) (Batchelor 1967). Later, it shifted to the mechanisms of vortex breakup and reconnection (Saffman 1990). In both, jetting has roles making them easier to see in visualization. Local vorticity cancellation, reduction of centrifugal forces and pressure build up result in jetting. The present work takes the understanding toward maximum stretching in the direction of principal strain just prior to terminal bursting.

Due to stretching, the root vortex elongates with time and the diameter decreases with axial distance from the root. The aspect ratio (length/diameter) is 2π in the DL vortex case (figure 2) and π in the turbulent case (figure 6). Figure 6(*c*) shows an axial velocity inside the vortex. In figure 6(*c*), U_{1L} is the DL jet velocity when the spread is narrow, U_{1T} is the turbulent jet velocity when the spread is wider, U_2 is the external axial velocity outside the jet, and U_{1w} is the axial velocity along the vortex axis when the jet weakens to a wake. In the short axial length of a cylindrical vortex, consider the ratio U_1/U_2, where $U_1 = U_{1L}$ or U_{1T}. At the roll extremity farthest away from the reader of the images, when the foil starts pitching, generating the vortex at the trailing edge near the free surface, $U_1 > U_2$. When the foil pitches back reducing the obstruction, the funnel dip closes (figure 6(*b*3)), stopping further entrainment of air.

When the fluid outside the vortex decelerates, the vortex diameter increases. The increase causes an additional pressure gradient effect within the vortex which causes further deceleration and thickening of the vortex. Small changes in the velocity outside the vortex cause a large change in U_1 and a (Batchelor 1967, p. 553). A time is reached when the ratio U_1/U_2 crosses a critical threshold value at which the velocity profile becomes unstable and causes the vortex to break. The thickening of the vortex and bursting are rapid in the turbulent cases in figure 6 and cannot be delineated. However, in the DL case in figure 2, they can be delineated as the stages of formation of the DH and the subsequent bursting.

Figure 6(*d*) explains how the compact vortex in (*b*) is formed and why the bubbles are spread in arcs extending over a span equalling the foil span while bursting. The vertical trailing edge vortex in panel (5), not seen in (4), is joined to the slanted root vortex at the kink; the vortex follows the trailing edge geometry in figure 1(*b*) which has a diagonal cut near the root. The entire coiled vortex is experiencing stretching in panel (5). However, in (6), the stretched vortex is suddenly released and the vertical part coils up to the slanted root vortex to form the compact vortex.

Consider a spring, mass and damper system where the mass models the axial compression of the distal end due to the stagnation point against the root. Ignore the damper because the time scales are small in elastic effects as the rapidity of the change between panels (5) and (6) shows. When the mass pulled down is released, it will jump up axially to the uppermost position using the energy of the stretching. The mass will oscillate backdown after that continuing the oscillation. The full vortex is undergoing such axial oscillation and releases the bubbles radially from the root in the process in the unstable range $45° < \beta \leqslant 90°$ only during one half of the oscillation. (In a low-friction mechanical apparatus of small forces (<1 N), up to five damped oscillations have been seen when the mass is released (Bandyopadhyay 2019).) The time period of axial oscillation is 0.067 s, which is two to three times the estimated bubble release time. As per this model, the aerated coil is stretched radially outward in the unstable range, then returns to the root to coil back and the cycle goes on. The bubbles, and the compressed energy are released during the journey of the distal

end back to the root. The radial arrays of bubbles in (b3) do show some lateral spacing. This explains the synchronous lateral discharge of bubbles in figure 8(f) in the boxed area.

In figures 2(2), 6(a1) and SI-IA-2 to SI-IA-4, the ratio of the wavelength (λ) to the lateral spread (Δ) of the double helix is $\pi/2$ to π. If the circulation number $\Gamma/(\upsilon\delta_2)$ remains constant, then the kinetic energy of the vortex is proportional to $\upsilon^2 \propto \Gamma^2/\delta_2{}^2 \propto f^4/\delta_2{}^2$. Hence, from $f = 1.0$ Hz to 1.25 Hz, the kinetic energy rises by a factor of at least 2.44 since the vortex diameter δ_2 drops. If the vortex diameter drops abruptly by a factor of 2 as in Tsoy *et al.* (2018) due to Kelvin mode $m = 0$, the kinetic energy stored increases by a total factor 10. Instead of any $m = 0$ mode, figure 6(d) shows that a vertical coiled vortex does exist connected to the slanted root vortex undergoing stretching (see left panel in figure SI-IA-6 for greater clarity). In figure 6(d5), the vortex diameter does drop by half for at least part of the length. (Compressibility is another mechanism of storing elastic energy, discussed later.) When the stretching is relieved, like a spring–mass system, the vortex jumps up to the root vortex and forms a compacted coil together. This is compacting of vorticity and elastic energy. An oscillation along the vortex axis would ensue. The compacted vortex expands and shrinks axially, bursting and filling up the sector over the span with bubbles where the vortex inclination is unstable. The bubble arrays are radial in figure 6(b3) aligning with the axis of the root vortex. But in earlier time, the arrays are orthogonal circular arcs as seen in figure 6(b2), aligning along the direction of the Taylor axis. The bubble separation from the tubes is incomplete in the inner half of the sector in figure 6(b2), but is complete later in figure 6(b3). Figure 2 also did show that bursting proceeds radially inward. Hence, on relaxation, the vortex coil experiences orthogonal oscillations, along the Taylor and the DH axes, and more complete bubble separation proceeding inward from the distal end. When the turbulent vortex bursts, the energy is immediately spread over sometimes 70° of the quadrant extending over the entire span (figure 6b2).

The foil circulation is sensitive to any air entrainment (figure SI-DA-4), hence variations in the spread of the vortex bursting, particularly in the case when $f = 1.25$ Hz, can be expected. Because of a lack of perfect lock-in between the foil oscillation and the wake, the wake frequency would have a jittering effect, but the foil would have none. The variation in the wake frequency would result in an amplified variation in the kinetic energy of the root vortex which is what is seen cycle to cycle.

Because of fluid rotation, wave motion is possible in the root, the foil leading edge vortices and vortices in the rolled-up flow in the foil tip (to be shown below). The entrainment of air in the core, which is compressible, increases the elasticity (Batchelor 1967, p. 555). The Kelvin mode $m = 0$, energy amplification factors of up to 10 and the post-bursting vortex spread angle of 70° are net measures of the elastic energy in the vortex.

3.8. *Vortex breaking and jetting near the apex of the root vortex just prior to bursting*

The vortex narrowing in figure 7 shows a breaking point where the DH ($\pm\Gamma$) crosses and the vorticities cancel. See figure 3(b) sketch. The breakup point has fragmented or there is no aeration. The growth of a vortex blob after that point and its bursting are shown in figure 7. In figure 7(a), in (1) and (2), the main part of the root is slanted at $\beta = 45°$ meaning that it is undergoing maximum turbulence amplification.

The bottom tip of the vortex shows a breaking, a growth of the vortex beyond and reconnection. In Saffman's (1990) model, viscosity cancels the vorticity at the breakup point, centrifugal forces drop and pressure builds up which produces a jet. The jet convects vorticity away and an 'apparent reconnection' is produced. The breakup point is stretched in the visualization. The visualization shows that the breakup and reconnection do not immediately lead to bursting. There is one more event involved, considered below.

Beyond the breakup, the vortex is radially growing. The tip of the jet in figure 7(a) shows unexpected examples of vortices spiralling on a conical surface: one in panel 2 and one in panels 6 and 7. The concentration of bubbles is inclined. The time interval between panels 1 and 2, and between 5 and 6 is 0.033 s and a higher framing rate than in Movie 3 is needed. The cone becomes upright in panel 7. The surface of the cone is at 45° to the flow direction. The cone is also radially stretching at 45° to the flow direction, but this time in the orthogonal direction. What occurs is a maximum vorticity and turbulence intensification in all possible directions. Due to the finiteness of the lateral rolling excursion, the shear is not confined to the longitudinal plane only. There is shear in the lateral direction also (see the triangular region in figure SI-IA-5). Between panels 6 and 7 in figure 7(a), the cone becomes upright because it is moving to the stable posture of maximum stretching. The DH is spiralling from the base to the apex in one example and from the apex to the base in another. The formation of the cones is modelled below.

Panels 2 and 5 in figure 7(a) show that the tip of the root vortex is jetting twice. The vortex grows radially in between. Figure 7(b) shows breaking in panels 1 and 2, and reconnection in panel 3; the terminal bursting is shown in panel 4.

The root vortex, formed by the pitching motion of the foil, is a pitch vortex. But the vortex formed in figure 7 after the breakup and reconnection has a horizontal axis and is modelled to be produced by the rolling motion. It is a roll vortex. The breakup has eliminated the memory of the initial condition.

Mechanism of the formation of the roll vortex and Kelvin mode $m = 1$. After the breakup point, the vortex in figure 7 develops a swirling jet of velocity U_j. The swirling jet is straight, horizontal and of uniform diameter. It is called a 'vortex rod'. The examples appear in figures 7(a2) and 7(cA); also see figure 9(n). The vortex rod and the conical vortex flows are modelled. See Movie 3 at time stamps 01:10 and 01:12 (m:s) for two examples of the formation of the $m = 1$ vortex.

The rolling (ϕ) 'vortex rod' (see figure 7c) is not expanding. Hence, the local circumferential velocity V_ϕ is $\geqslant U_j$, the local jet velocity, which is subcritical. Assume $V_{\theta max} = V_\phi = 0.43$ m s^{-1}. The transverse boundary layer thickness $\delta_{tr} = 0.5\epsilon$, half of the local vortex rod diameter, where the estimated $\epsilon = 0.0043$ m. Transverse boundary layer Reynolds number $Re_\phi = (V_\phi \delta_{tr})\nu = 921$, a low value. Axially, the jet Re of the vortex rod is $Re_j = U_j\epsilon/\nu = 1843$, taking ν of water (1.003×10^{-6} m^2 s^{-1}), also a low value. The j and ϕ motions, although treated separately, produce a spiral. The air flow can be neglected whereby, on the water side of the interface, the flow is of a stabilizing convex curvature and not of a destabilizing concave curvature air flow. The rod is straight, so longitudinal curvature effects are not present, and the transverse curvature effects are present throughout the transverse water boundary layer. At low Re, such transverse curvature boundary layers are relaminarizing (Piquet & Patel 1999). For these reasons the Taylor number Ta (defined later in the context of figure 9) is subcritical, and the aerated transverse pairs of contra-rotating vortex tubes are not formed, although some striations on the interface are present. This vortex rod is stable and is not a source of bubbles.
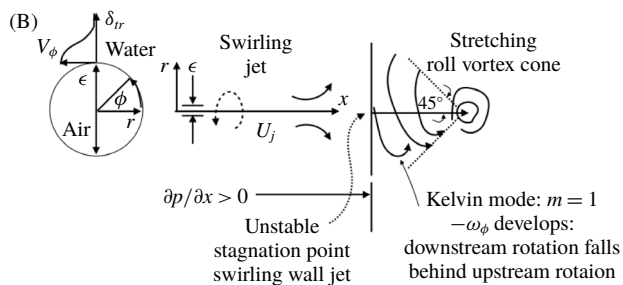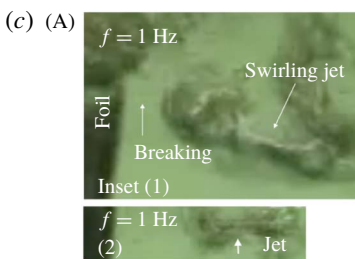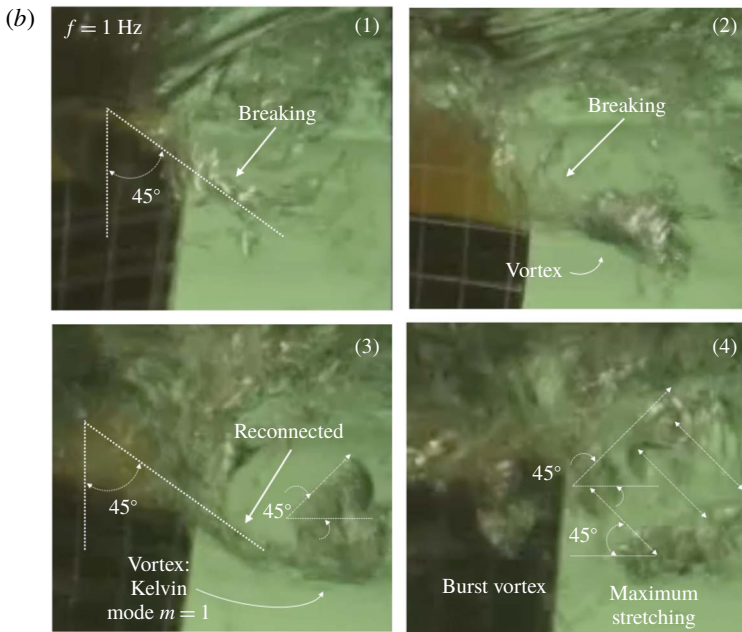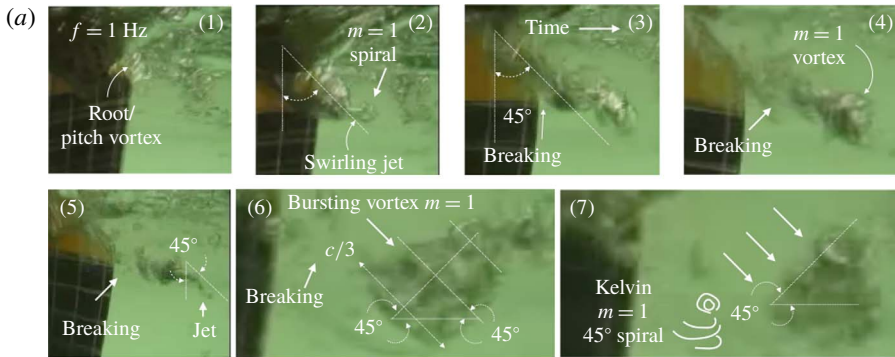
FIGURE 7. Vortex breaking, jetting, reconnection and stretching along 45° to flow direction just prior to terminal bursting (*a,b*), and mechanism of formation of roll vortex at vortex tip (*c*). (*a,b*) These sequences take place after the slant β of the main root vortex reaches 45°; repeated jetting and spiralling at vortex tip are shown, and formation of spiralling cones and stretching along 45° are shown. (*c*) Insets 1 and 2 in (A) show examples of 'vortex rods' which are swirling jets as in (*a*2); (B) schematic of the mechanism of the formation of the roll vortex cones at the tip of the swirling jets shown in (*a,b*).

The mechanism of the Kelvin mode $m = 1$ is shown schematically in figure 7(cB, cC). Define a cylindrical coordinate system (x, r, ϕ). At the terminal stage, the horizontal jet impinges on the cross-stream vortex-free body of water, creating a stagnation point. The swirling jet does not translate horizontally to any significant extent (about 0.02 m) confirming the formation of a stagnation point. Under certain conditions of the Reynolds number $Re_j = U_j \epsilon / \nu$, based on U_j, the vortex diameter ϵ and kinematic viscosity ν, the flow very near the stagnation point becomes unstable to azimuthal foil roll oscillation (ϕ). The DH tip experiences a motion that combines the axial displacement of the jet and the instability of the stagnation point flow which causes a motion in the cross-stream plane. As a result, the tip traverses a conical surface, as seen in figure 7. There is a vertical shear ($\partial U / \partial y$) normal to x. In order to maximize stretching, the vortex is oriented along $45°$ to x (the $-45°$ orientation is also present). Depending on the initial conditions, this $45°$ cone can have a source or a sink type, radially outward or inward flow (figures 7(a6,a7) and 7(b3,b4)). In the cross-stream plane, the equation of a source spiral (growing spiral) can be fitted as $r = K\phi$, and of a sink spiral (damping spiral) as $r = -K\phi$, where K is a constant. The position vector on the cone is $s = (x, r)$. The cone in figure 7(a) shows that K is a constant. Accounting for the axial jet and maximum stretching, $\partial r / \partial x = \tan(\pi/4)$. The mechanism of the elastic vortex (which is more viscous and less elastic) is both similar and dissimilar to the viscoelastic fluid buckling (which is more elastic and less viscous) (Mahadevan, Ryu & Samuel 1998).

The annotation on the right of figure 7(c) mentions that the vorticity in the cross-stream plane develops a negative component ($-\omega_\phi$) with respect to that found in the upstream 'vortex rod'. This negative component causes a spiral to form (Batchelor 1967). The spiral is stretched to the maximum extent, triggering the bursting of the entire articulated vortex. The mechanism is discussed in § 3.10.1 in the context of the formation of similar Kelvin $m = 1$ spirals in the rolled up foil-tip flow.

From figure 7, it is estimated that U_j is 0.13 m s^{-1}, which is less than the maximum foil velocity. Radial velocity $\mathrm{d}r/\mathrm{d}t = 1.5 V_{\theta max}$, and $V_{\theta max} = 4.6 U_j$. The radial velocity (0.9 m s^{-1}) is close to the foil velocity and is 6.9 times U_j. The maximum swirl velocity of the jet may be just below $V_{\theta max}$ of the root vortex, assuming some dissipation, because the diameter ϵ is similar to the root vortex or pitch vortex diameter, as in figure 7(d1).

What happens if two co-rotating vortex tubes (Γ, Γ) come close to one another? Comparison of figures 7 ($\pm\Gamma$) and 11 (Γ, Γ; appears later) show that the vortex breakup is not present in the (Γ, Γ) case. Both flows encounter regions of $\partial p / \partial x > 0$ and develop a stagnation point. The instability of the stagnation point flow leading to the development of a Kelvin $m = 1$ mode single spiral occurs in the (Γ, Γ) case. This case is similar to the spiralling cone in the ($\pm\Gamma$) example. Both undergo stretching along the principal plane direction ($45°$ to x). Finally, the form after bursting is similar: bursting into an arrowhead in the (Γ, Γ) case, and into a cone in the ($\pm\Gamma$) case. In the region of $\partial p / \partial x > 0$, ahead of the stagnation point, the displacement of a vortex line radially outward creates an imbalance between the Coriolis and the viscous components, setting up a resonant oscillation. This event creates the $m = 1$ Kelvin spiral in both.

3.9. *Two mechanisms of bubble formation in turbulent vortex bursting*

Figures 1(c), 8(a) and 10 show that two sizes of bubbles are formed (more examples appear in the SI). The coarse bubbles are formed near the free surface mostly in
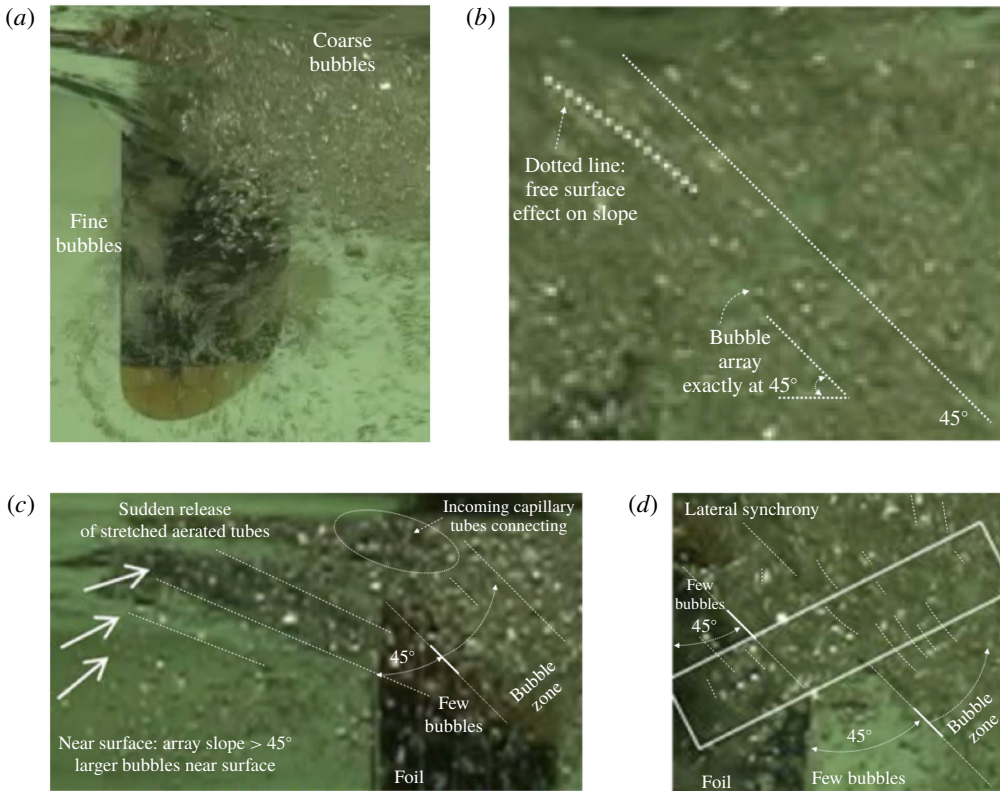
FIGURE 8. Bubbles are formed in clusters: fine bubbles in the foil boundary layer (*a*) and coarse bubbles near the free surface or away from the foil (*b–d*); see figure SI-TA-4 for ranges of *Re* and *We* where coarse and fine bubbles are formed in relation to *Re* versus C_d and *We* versus C_d due to Haberman & Morton (1953) for bubbles rising at terminal velocities in filtered water. Arrays of coarse bubbles are formed when a stretched aerated vortex tube is suddenly released (*b*). All coarse bubbles are formed at the same time.

the foil wake–free surface quadrant. Here, the spiralling tubes (figures SI-TA-1(*a*), 1(*e*), 6(*a*1)) of the capillary surface waves are first stretched into the funnel of the root vortex by the pitch oscillation. Arrays of bubbles of fairly uniform diameter are formed (figure 8*b–d*) when the foil blockage is removed. Fine bubbles form on the foil surface farther from the foil root where the bubble size would be influenced by the wetting properties and viscous drag forces (Lepercq-Bost *et al.* 2008).

3.9.1. *Mechanism of the formation of coarse bubbles: Taylor air tubes of the root vortex*

From the images, the diameters in the DH, where *Re* is lowest, are from 7.0×10^{-3} to 20.0×10^{-3} m. These bubbles are arched and distorted ellipsoids, and the diameter refers to the minor axis. The diameters of the bubbles at higher *Re* are from 1.5×10^{-3} to 20.0×10^{-3} m (Talaia 2007). As shown in figure SI-TA-4(*g,h*), the present work lies in these ranges. The coarse bubbles are in these ranges: $d = 0.0015$–0.02 m, $v_\infty = 0.20$–0.40 m s^{-1}, $Bo = 0.303$–53.82, $Ca = 0.0028$–0.0055, $Fr = 2.72$–0.8155, $Mo = 2.5638 \times 10^{-11}$–$2.5638 \times 10^{-11}$, $Re = 300$–8000 and $We = 0.8239$–44. Because

Bo is close to 1.0 at $d = 0.0015$ m, both surface tension and gravity forces act as stabilizing forces in the Taylor air tube case. But *Bo* is $\gg 1.0$ when d is 0.02 m; hence, only gravity, not surface tension, will dominate as a stabilizing force in the DH case. Repeating the helix experiment at 6 and 49 °C would vary the *Mo* by a factor of 10. The coarse to fine diameter ratio is 10^4–10^5 (see § 3.9.2).

The marked example in figure 8(*b*) shows the presence of an array of coarse bubbles of nearly the same size slanted at precisely 45° to the flow direction. Near the foil, the slant of the bubble array is shallow. But downstream and away from the foil, the slope of the bubble array is largely 45°. The diagonally arrayed bubbles are formed simultaneously in the entire field of view. This idea supports the hypothesis of bubble diameter number (N_B) modelling given earlier, namely that maximum stretching of the vortex at 45° followed by sudden relaxation causes the discrete bubbles to form out of the continuous aerated tube. In the modelling of N_B in § 3.6, the vortex core pressure due to centrifugal effects is balanced by surface tension. Equations (3.2) and (3.3), on the other hand, do not include any property of the vortex.

The elliptic region in figure 8(*c*) is in reference to figure 3(*a*), where there are two scales of foci. Short bubble arrays meet where the foil stem pierces the free surface. These capillary tubes are forming small horseshoe vortices and may be the origin of the small diameter DH root spirals in figure 4(*c*1, *d*1). Future research on the stability of the contra rotating foci in figure 3(*a*) would be useful.

What happens if aerated capillary tubes in proximity are suddenly released *en masse*? Figure 8(*c*,*d*) shows the near-surface bubble arrays upstream and midstream of the foil in (*c*) and in the immediate downstream root region in (*d*). There are few bubbles in the stable region of the root vortex $0° \leqslant \beta < 45°$, but there is a dense cluster of bubbles in the unstable region of the vortex $45° < \beta \leqslant 90°$. The linear bubble arrays upstream are at an inclination of $\ll 45°$ (figure SI-IA-4). A few plausible short segments of dashed lines are shown of bubble arrays originating from the same aerated vortex tube. As marked by the box, the neighbouring tubes discharge the bubbles simultaneously. The neighbouring tubes are oscillating synchronously when suddenly released after stretching.

Figure 9 shows the formation of stacks of aerated tubes whose diameter is similar to the coarse bubbles. Figure 9 has two parts: 9(*a*) and 9(*b*–*n*), with part 9(*b*–*n*) being subdivided into 9(*b*–*h*) and 9(*i*–*n*). Figure 9(*a*) shows an unwound DH where the bubbles, one of them marked by the arrow, are forming at axial intervals ($\lambda_d/2$) approximately equal to half the diameter d of the tube locally. However, λ_d varies axially, and the bubbles do not separate at axial distances of d (figure 2). The interface necks locally because of the sudden loss of the tube stretching and the onset of radial oscillation. Theoretically, in progressive capillary waves, the maximum value of the ratio d/λ is 0.73 (where d is the height of the crest relative to the trough) if g is ignored and γ is the only restoring force on a nominally flat free surface (Crapper 1957).

In figure 9(*b*–*h*), $f = 1.0$ Hz; in figure 9(*i*–*n*), $f = 1.25$ Hz. Figure 9(*b*–*n*) shows the foil root vortex and a stack of air tubes wrapped around. They are arranged in order of increasing complexity. Further examples of air tubes appear in figure SI-IA-6.

Taking centrifugal force as the destabilizing force and viscosity as a stabilizing force, define $Ta = (V_{\theta max}^2/R_1^2)R_1(R_2 - R_1)^3/\nu^2$ for concentric rotation cylinders (White 1994). Here, R_1 is the external radius of the internal cylinder, and R_2 is the internal radius of the external cylinder. Applying to the present case and taking the gap ($R_2 - R_1$) to be d (= 0.006 m), the high value of R_2/R_1 is 0.85. The ratio can vary cycle to cycle from 0.22 to 0.61. In solid cylinders, R_2/R_1 is 0.883 in Andereck *et al.*

(*a*) $\beta > 45°$

Discrete bubble forming

Double helix unwinding

Breakup

(*b*) Root vortex

45°

Inset

One turn

(*c*) Compression

Resistive torsional spring constant

45°

Pitch torque

Compression

Aerated

(*d*)

Air

Folding capillary waves

Air

Water

β

y

Stretching of Taylor tubes

Bubbles of this size form when stretching is relieved

$\partial p/\partial y > 0$

Root vortex not shown

Aerated Taylor tubes

Stretching of root vortex
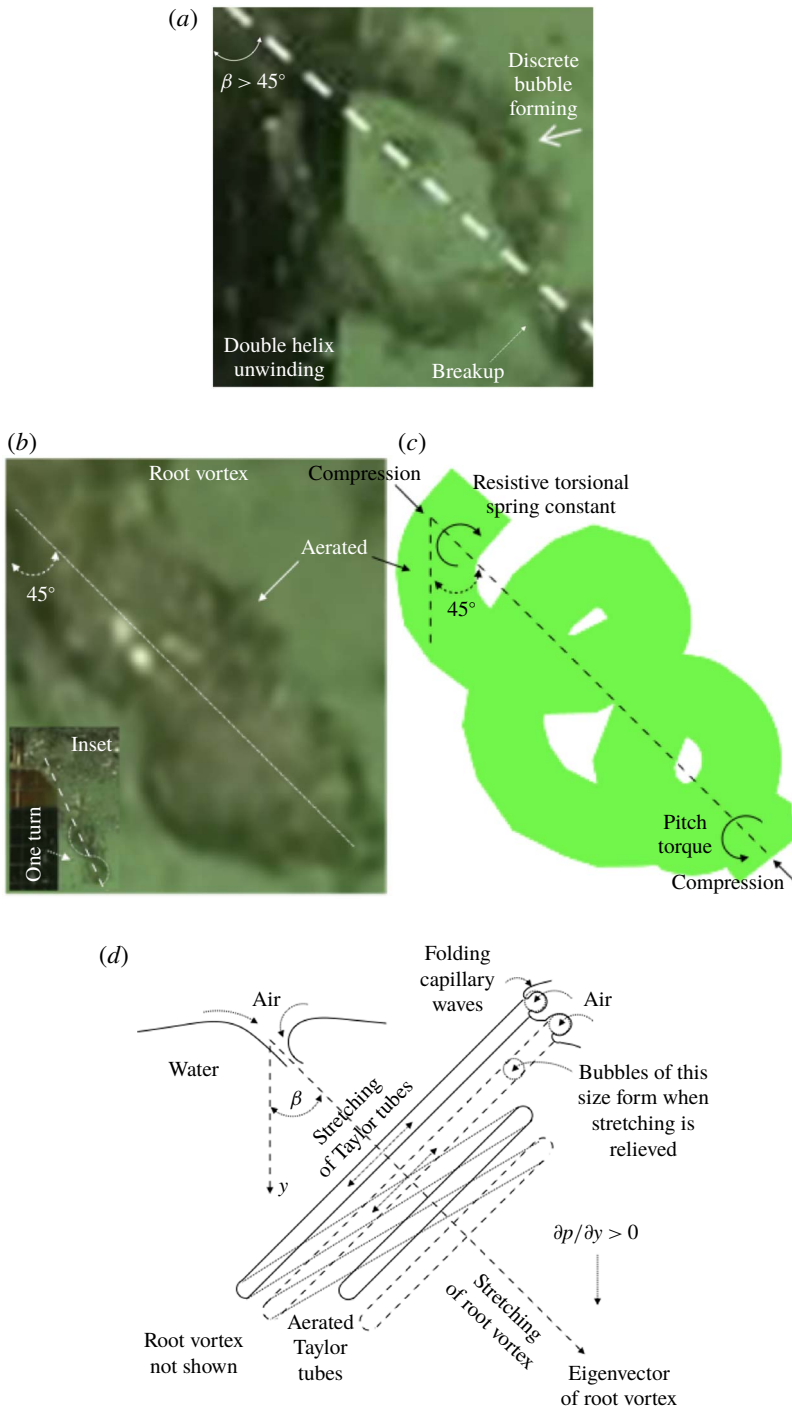
Eigenvector of root vortex

FIGURE 9. For caption see page 41.

(1986). It is easier to measure the diameter of the root vortex, than the diameters of the vortices or bubbles. The critical value of *Ta* is 1700 is taken to calculate the 'cylinder' gap which in the present case is the diameter of a Taylor roll cell or bubble
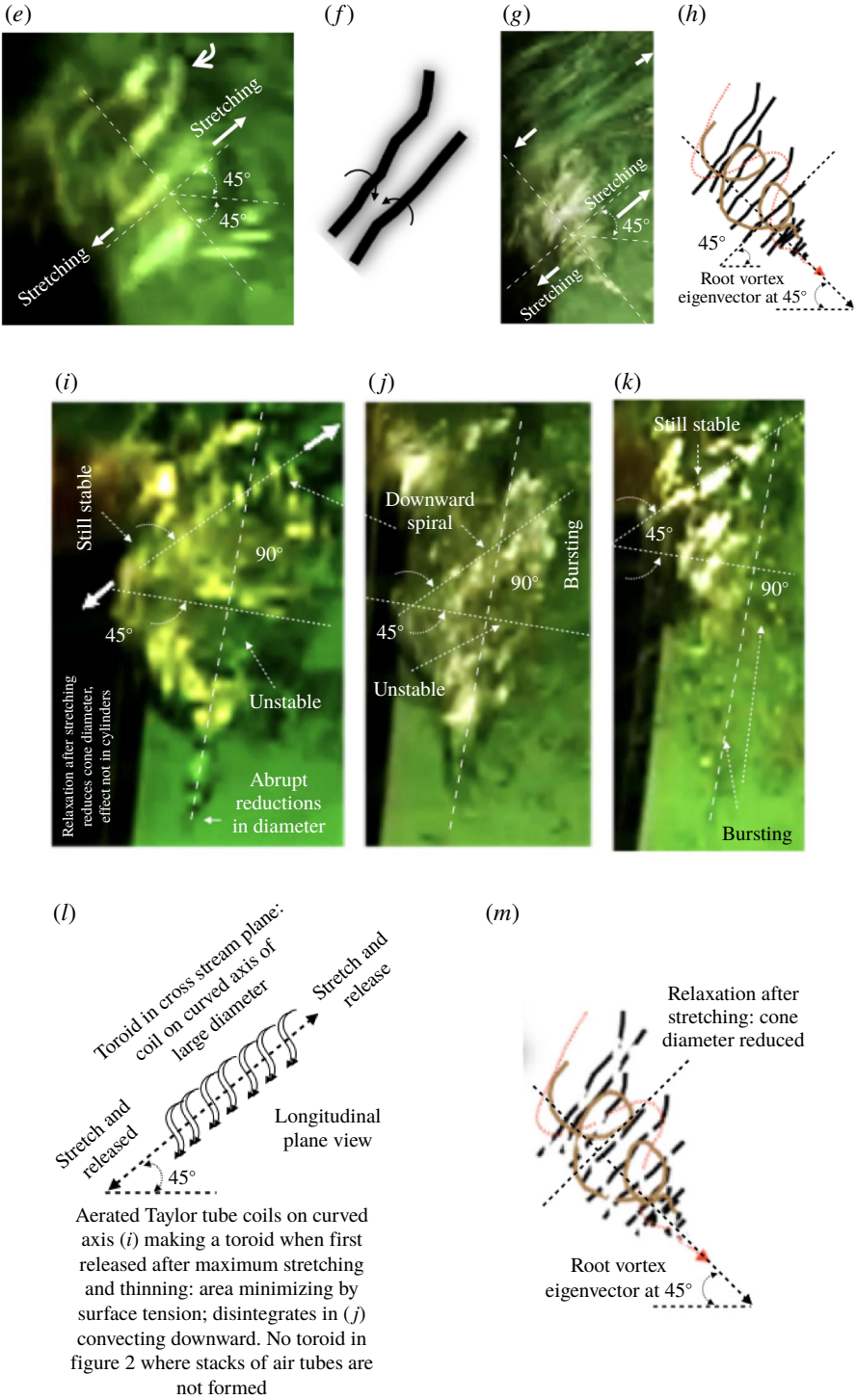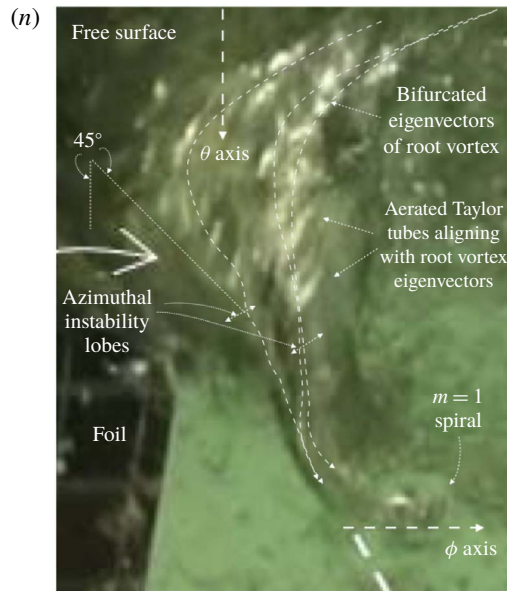
FIGURE 9. For caption see next page.

FIGURE 9 (cntd). Aerated Taylor tubes of the root vortex: $f = 1$ Hz (*a–h*) and $f = 1.25$ Hz (*i–n*). The images are arranged in order of increasing but stable complexity such as the emergence of fine pitch spiralling and patches of disorganization. The increasing complexities are reminiscent of increasing *Re* in Taylor–Couette experiments but with solid cylinders (Coles 1965; Andereck, Liu & Swinney 1986). In the air tubes of the double helix (*a*), the pitching motion has suddenly removed the flow obstruction, and discrete bubbles are forming in the tube but are not separated yet; the necking about one bubble is marked by the arrow. The helical root vortex (*b*), modelled in (*c,d*) has one full turn (the previous panel showing clear one turn appears in the inset, image reduced by half; see figure SI-IA-2) and is experiencing maximum stretching (given by the 45° slope). Organized Taylor roll cells of air tubes (*e*) are shown in contra-rotation in a schematic (*f*). Taylor tubes on a top-like root vortex (*g,i–k*) are modelled in (*h,m*). The flow in (*i,j,k*) is modelled in (*l,m*). A root vortex with multiple azimuthal lobes of instability is shown in (*n*). The curved arrow in (*e*) marks the curl over at the tip of the Taylor tube. The abrupt reductions in diameter at the apex, marked in (*g,i*), indicate the presence of Kelvin mode $m = 0$ (Tsoy *et al.* 2018). The root vortex cone (*i–k*) has just been relaxed after maximum stretching and the cone diameter shrinks; surface tension is reducing the surface area; see notes in (*l*).

diameter (*d*). Taking all cases, the root vortex diameter near the origin is 0.0154 m to 0.08 m. At $f = 1$ Hz, take $2R_2$ as 0.08 m in one example of a large value and $V_{\theta max} = 0.419$ m s^{-1}. For critical *Ta*, these give $d = 0.0008$ m, a reasonable value. Due to high background turbulence, the critical *Ta* may be <1700; $U_\infty c/\nu$ is 750, a transitional value for reverse Kármán jets (Bandyopadhyay *et al.* 2012).

The conical form of the root vortex sets up an internal helical flow toward the apex. Hence, the flow is open axially (Wereley & Lueptow 1999). The spiralling core vortex is represented by the eigenvector shown schematically in figures 9(*c*), 9(*d*), 9(*h*) and 9(*m*). The flow is closed radially because it is rotating. The rotary motion of the air–water interface forms ripples (millimetre scale) creating the air tubes in figure 9(*d–n*). The tubes may also be originating in the free surface when the ripples are drawn into the funnel. In the lowest *Re* case in figure 9(*b*) at $f = 1$ Hz, the Taylor

tubes are incipient and formed in pairs. Hence, the Taylor number (*Ta*) is barely critical (*Ta_c*). Owing to a lack of accurate lock-in, *Re* is slightly higher in figure 9(*g*), although figure 9(*f*) is still at 1 Hz. A model of the top-shaped vortex in figure 9(*g*) is shown in figure 9(*h*), which shows the spiralling eigenvector and an interesting narrowing of the tip where the rotational velocity is high. Stacks of Taylor tubes appear at the interface with some waviness. The nipple in figure 9(*b*) is rounded, but it is conical in figure 9(*g*). In both figures 9(*b*) and 9(*g*), the vortex has a narrowing half-way along the axis, meaning that the mode of the eigenvector has developed a 'coning' in figure 9(*g*). This conical mode of the root vortex is stable because, overall, it is identical at $f = 1.25$ Hz, as shown in figure 9(*i*–*k*). It has been shown earlier that the stability is due to the fact that the vortex is stable for $\beta \leqslant 45°$. In figure 9(*n*), *Re* is higher, and the vortex cross-section has circumferential (but non-axisymmetric) Widnall-type instabilities (Pierrehumbert & Widnall 1982).

In figures 9(*i*–*k*) and 9(*n*), $Ta > Ta_c$ because the number of air tubes is large. In the case of figures 9(*i*–*k*) and 9(*n*), the number of bubbles formed per unit length of the tube would be numerous since the air tube diameter is smaller than in figure 9(*a*).

Compared to figure 9(*e*), as shown schematically in figure 9(*f*), the Taylor tubes in figure 9(*i*–*k*) show breaks that are the twisting of the air tubes. The breaks indicate that spiralling waves are present in the Taylor tube stacks, in figure 9(*i*) an example is marked by a pair of arrows, and the wavelength of the spiral is similar to the tube diameter. The elasticity magnifies the effect. From the standing wave model in an air tube, the local $L/D = N\pi$, where *N* is an increasingly large integer. The bubbles formed would spin in relation to *N*.

Figure 9(*g*) is modelled in figure 9(*h*), and figure 9(*i*–*k*) is modelled in figure 9(*m*). While the vortex eigenvectors are identical, the *Re* of the Taylor tubes has increased, and the tubes are distorting and showing intermittency in the distortion. The dispersed packets of unstable vorticity in the sequence (*i*–*k*) co-exist below the stable stacks of air tubes still being stretched at 45°. The unstable packets appear down below in the increasing adverse pressure gradient region where the root vortex is narrowing. They are already bursting in (*k*). The air tube in the straight part of the root vortex, however, is able to sustain the standing waves by selecting a higher value of *N*. This feature is not seen in the narrowing part. It is suggested that, for instability and bursting to be triggered, the waves must stop standing first due to some larger-scale ($\ll D$) non-uniformity in the boundary condition.

The side-to-side rolling motion of the foil produces an overall horizontal jet flow from left to right in the images in figure 9. In figure 9(*e*,*g*,*i*–*k*), the Taylor tubes are inclined to the horizontal external flow direction at a mean angle of 45° which is the direction of principal strain. A few examples are marked by the pairs of thin arrows in (*e*,*g*,*i*), and the direction of each arrow indicating the direction each stretches. In (*e*), the curved arrow marks an upstream curling over of the tip. The air tubes are expected to be elliptical in the transverse plane. Near the tip, if the induced flow between the legs of a Taylor tube lying in the transverse plane (not visible) is upward, then, in the absence of any external mean flow shear, an upstream curling over would be produced. In turbulent boundary layers, which are jungles of hairpin vortices, in the outer part of the layer and away from the wall, the hairpins also lie at a mean angle of 45° to the flow direction, and at low *Re*, similar upstream curling over do occur (Bandyopadhyay 1980; Head & Bandyopadhyay 1981; Perry & Chong 1982; Adrian *et al.* 2000; Wu & Moin 2009).

The slanting of the Taylor tubes is close to 45° without much variation. We attribute this organization to the external forcing of the flapping foil. In low *Re* turbulent

boundary layers, such a forcing mechanism accurately models the spatio-temporal drag reduction (Bandyopadhyay & Hellum 2014).

Although the no-slip boundary condition of conventional Taylor–Couette cylinders (Taylor 1923) is modified to a slip condition of a rippled free surface, the growth of waviness, spiralling and intermittency of the air tubes with *Re* are similar (Coles 1965; Andereck *et al.* 1986; Tritton 1989). The states of the Taylor air tubes are stable, organized and not turbulent (Gollub & Sweeny 1975). The bubbles from neighbouring tubes would rotate in the opposite directions (figures 9*d*, 9*f* and 9*l*). The rotation helps provide the stable trajectory in figure 9(*b*2). The above is an uncommon example of Taylor–Couette flow.

3.9.2. *Mechanism of the formation of fine bubbles: wall effects*

In the foil boundary layer, with increasing wall shear stress (decreasing viscous sublayer thickness δ_s) with increasing f, the fine bubble diameter would decrease. The capillary number Ca is defined as the ratio of the viscous force to the interfacial tension force and is given by

$$Ca = \mu U / \gamma, \tag{3.2}$$

where μ (Pa s) is the absolute viscosity of water, U (m s^{-1}) is the velocity at the edge of the viscous sublayer and γ is the surface tension (N m^{-1}). The bubble diameter would be smaller than δ_s.

The bubbles would form when the difference in pressure, ΔP, between the surrounding water and the air jacket overcomes the capillary pressure difference. From Young's thermodynamic equation, the minimum pressure difference, P_{min}, is a function of the contact angle (the wetting property), as

$$P_{min} = 4\gamma \cos \theta / d, \tag{3.3}$$

where θ is the contact angle between the water and air on the foil surface, and d is the bubble diameter. Here, γ remains constant, but the head increases with the span of the foil. So, near the foil tip, the water will advance into the air jacket, but, at a shallower span, the air jacket will advance into the surrounding water. Depending on whether the interface on the foil surface is advancing or receding, θ can be acute or obtuse. This mechanism can be called a wall-based mechanism.

Figure 1(*b*,*e*) and SI-TA-3(*c*) show two paths of air entrainment (see Eggers 2001). Figure 10 shows the wall-based mechanism of the formation of fine bubbles. The funnel centre, marked by a point source of pressure $-p$, is moving closer to the fin while air is sucked in jacketing the suction side of the foil. Clouds of bubbles form near the trailing edge of the jacket toward the foil tip. The edge of the fine bubble cloud toward the foil tip is moving upstream. But the trailing edge of the air jacket closer to the root is moving slightly toward the foil trailing edge. Near the foil root, there is an advancing wave front forming bellows in the jacket – the arcs around the centre $-p$, as shown in the schematic in figure 10(*c*). As shown in the elliptical insets in figure 10(*c*), near the root, the air front advances toward the trailing edge, following the arc of the bellows, while the water front advances upstream toward the foil leading edge. Hence, the contact angle on the water side recedes near the root ($\gamma_R < 90°$), while it advances near the foil tip ($\gamma_R > 90°$). The contact angle is at equilibrium near the foil root where the spanwise edge of the cloud is.

The fine bubbles are produced by the bursting of the air-jacketed boundary layer over the suction side of the foil near the outer end of the span where the foil surface velocity is higher (figure 10). The fine bubbles are not formed at $f = 0.75$ Hz.
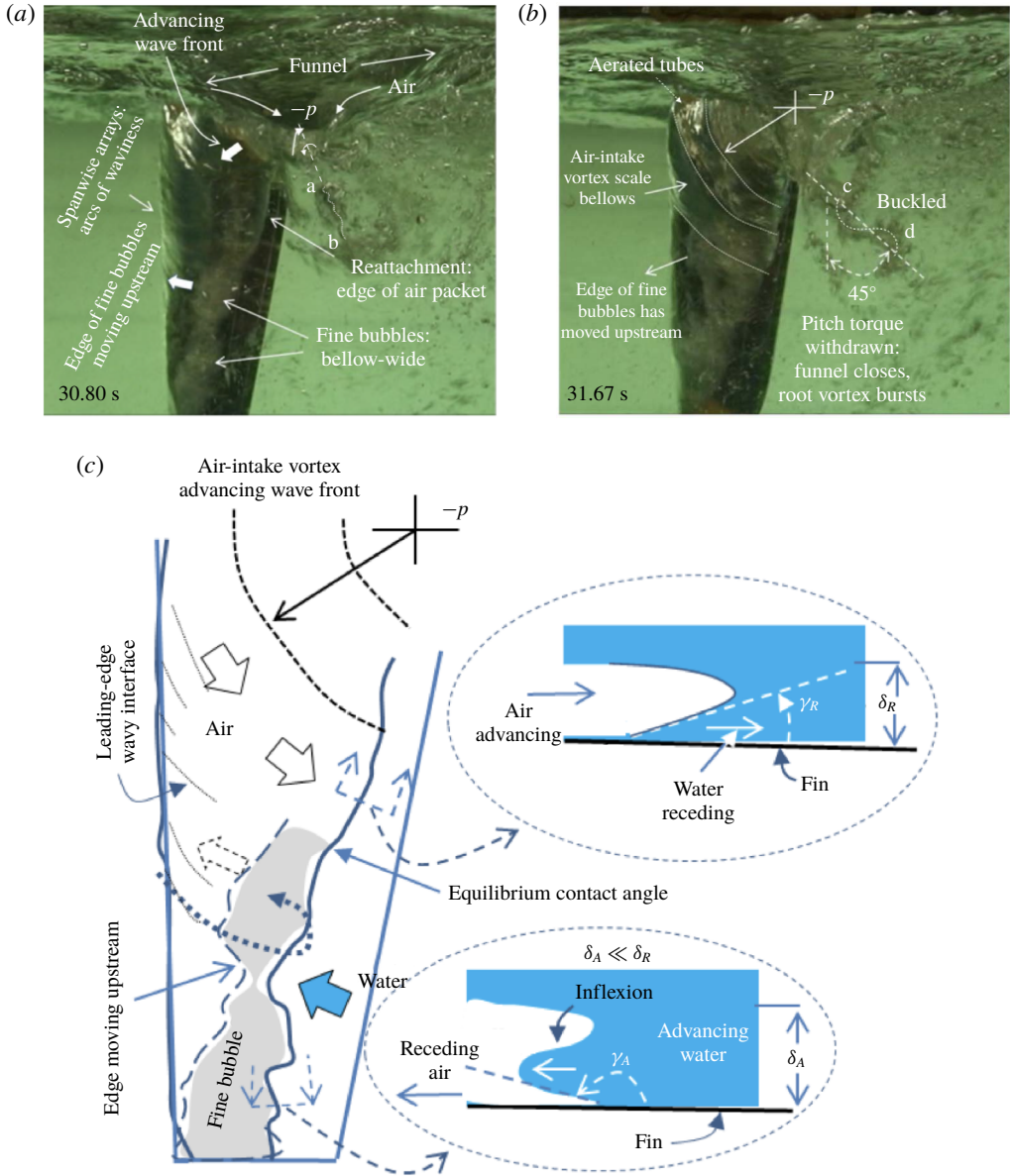
FIGURE 10. Formation of fine bubbles on the foil surface: time sequence of air jacket and regions of clouds of fine bubbles over the suction side of the fin (*a*,*b*); schematic of surface tension mechanism of the formation of fine bubbles (*c*). Two elliptical insets in (*c*) show cross-sections of areas where the foil surface and the air and water interfaces meet. In (*a*), the markings 'a' and 'b' draw attention to an extremely thin aerated vortex with small amplitude waves, aligned with the centre of the funnel; when stretched to the maximum extent due to the 45° slope, this vortex buckles to a sinusoid marked (*c*,*d*) in (*b*).

Assuming a Blasius boundary layer to be developing over the foil, the foil velocity is $V = 2\pi fr$, where r, the average foil span $= 0.15$ m. Assuming a Blasius profile, the boundary layer thickness at the half-chord distance of $l = 0.05$ m from the leading
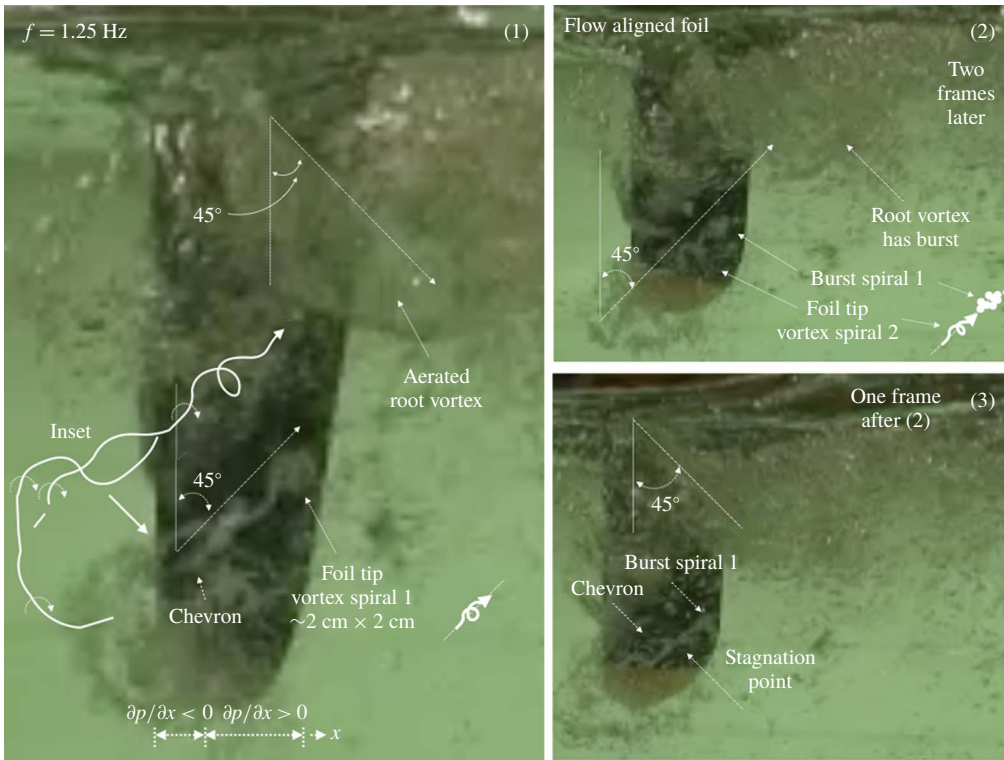
FIGURE 11. Time sequence showing that the foil-tip vortex and the root vortex burst simultaneously at $f = 1.25$ Hz. A row of two spiralling vortices ($m = 1$) from the foil tip is being stretched at 45° to the vertical, moving diagonally upwards. Subsequently, they burst simultaneously with the root vortex. Arrows of the tiny spiral schematics on the right side of the panels in (1) and (2) show the eigenvector of the vortex line. The inset in panel 1 shows how a pair of co-rotating vortex lines spiral to produce the chevron; they then fuse and produce the single spiral bursting eventually as shown in panel 2. Regions of favourable and adverse pressure gradients are marked in (1); x is along foil chord.

edge is $\delta = \sqrt{\nu l/V} = 1.9952 \times 10^{-4}$ m at $f = 1.0$ Hz and $= 1.7846 \times 10^{-4}$ m at $f = 1.25$ Hz. These values are the upper limit of the fine bubble diameters. Use $v_\infty = gd^2(\rho_w - \rho_a)/(18\mu_w)$ (Stokes 1880) to get the terminal $v_\infty = 0.0216$ m s^{-1} at $f = 1.0$ Hz and 0.0173 m s^{-1} at $f = 1.25$ Hz. We estimate these values: at $f = 1.0$ Hz, $Bo = 0.0054$, $Ca = 2.98 \times 10^{-4}$, $Fr = 0.2394$, $Mo = 2.5638 \times 10^{-11}$, $Re = 4.30$ and $We = 0.0013$; at $f = 1.25$ Hz, $Bo = 0.0043$, $Ca = 2.38 \times 10^{-4}$, $Fr = 0.1713$, $Mo = 2.5638 \times 10^{-11}$, $Re = 3.08$ and $We = 7.3487 \times 10^{-4}$. Because $Bo < 1.0$, γ, not g, dominates as a stabilizing force, unlike in the coarse bubbles (see figure SI-TA-4(g,h) to compare).

3.10. *Co-rotating vortex tubes of rolled-up foil tip flow*

The boundary layer flow from the pressure side near the foil tip rolls up to the suction side in a 270° arc, as shown in figures 11, 12, SI-IA-7 and SI-IA-8. The rolled-up foil-tip vortex is marked by fine bubbles. Due to the absence of any breakup, the vortex tubes are inferred to be co-rotating, represented as (Γ, Γ).

In figure 11, the rolled up foil-tip flow has a row of two single spirals (they are not DH) that are being stretched at 45° to the horizontal external flow direction as the DH

root vortex does. The spirals, 2 cm × 2 cm in size, are larger than the local boundary layer thickness. In figure SI-IA-7, the formation, bursting and the continued motions of the two spirals downstream of the foil are tracked frame by frame (see Movie 3, time stamp 01:38 (m:s)). Due to the passage over the accelerating part of the foil boundary layer, the spirals 1 and 2 in figure 11 form beyond the chord location of maximum foil thickness after the vortex tube has thinned. The spiral 1 bursts into an arrowhead form (see figure 3*b*), first seen in panel (2), where the external flow velocity has dropped in conformity with Batchelor (1967).

Panels 3 to 6 in figure SI-IA-7 show two sequences of the formation of a single spiral, bursting into an arrowhead and the formation of chevron in the rear. The rear end of the burst arrowhead does not move over the time step of one frame indicating, the presence of a stagnation point.

The inset in panel 1 of figure 11 clarifies that the chevron in the rear of the spiral is actually the helical interaction of two co-rotating vortex tubes. On entering the adverse pressure gradient boundary layer, the chevron widens laterally, the two vortex tubes subsequently fuse and a single spiral (or coil) is produced which eventually bursts. Spirals form when vorticity becomes negative (figure 7(*c*B)). The spirals in figure 11(1) exist outside the Blasius layer which is only 2 mm thick. The spirals and the chevrons are not associated with any externally imposed perturbation, such as boundary layer injection, and do not trigger any boundary layer transition and thickening over the foil (Perry, Lim & Teh 1981).

Apart from providing direct experimental evidence in support of Batchelor's (1967) theoretical statements on vortex elasticity, we show that vortex bursting requires a necessary condition to be satisfied, namely, that the vorticity amplification needs to be maximized prior to bursting by bringing the alignment of the vortex to the direction of principal strain. Cross-stream views of principal strain may be explored in vortex bursting where the maximum vortex stretching has not yet been reported. In future research, turbulent boundary layer over the underside of a horizontal plate in water would subject the hairpin vortices to both principal strain stretching and adverse pressure gradient.

The foil-tip rolled up flow has signs (Γ, Γ) because it originates from the boundary layer vorticity on the pressure side where there is no separation. The stretching along the 45° inclination intensifies the vorticity bringing the two vortex cores closer. The vortex tubes fuse into one (2Γ), and do not cancel their vorticities as in the contra-rotating DH $(\pm\Gamma)$. The fused tube (2Γ) develops Kelvin instability of mode $m = 1$ (Tsoy *et al.* 2018) in the adverse pressure gradient region of the foil boundary layer. The foil-tip single spiral (2Γ) bursts simultaneously with the root vortex DH $(\pm\Gamma)$.

3.10.1. *Formation of single spirals of Kelvin mode $m = 1$ and bursting*

In a vortex tube, in the cylindrical coordinates (x, r, ϕ), let (u, v, w) be the respective velocities, $(\omega_x, \omega_r, \omega_\phi)$ be the vorticity components and a and b represent the radii in the accelerating and decelerating zones of the foil boundary layer. In a swirling flow, the relationship of w with (u, v), produce unexpected changes. Using the steady, linear and axisymmetric analysis of Batchelor (1967, §§ 7.5 and 7.6), the formation of the spirals, the bursting and the origin of waves and chevrons are explained. These are the properties of a vortex, and including the origin of waves in a vortex, the explanations do not need the vortices to be aerated, although that could enhance elasticity.

In the accelerating leading edge of the foil, as the vortex tube is stretched, the components $(u, w, \omega_x, \omega_\phi)$ increase and the radius a is reduced $(a < b)$. As the vortex tube enters the decelerating region of the foil boundary layer, the radius b increases

and $(u, w, \omega_x, \omega_\phi)$ drop. Since $wr_v = \text{const.}$ (r_v is radius), a vortex line going around the centreline of the vortex tube would be pushed outward in the transition zone. While going around, compared to the upstream zone, the vortex line will fall behind and a spiral with $(-\omega_\phi)$ will result because this component was (ω_ϕ) in the accelerating zone. This produces a positive $\partial u/\partial r$ in the downstream region so that a minimum value of u is produced at the centre of the tube. Across the vortex tube, the velocity profile changes from a jet to a wake (figure 6c).

In a pipe flow, Brown & Lopez (1990) have shown the development of a negative component of vorticity as the reason for bursting attributing this to tilting and stretching. We give direct evidence of $(-\omega_\phi)$, including that for tilting which produces maximum stretching. We give visual evidence of bursting. We have seen similar evidence in the root vortex post-breakup, making the evidence sufficiently broad. We have interpreted these orderly spirals as Kelvin mode $m = 1$. The understanding of the vortex bursting mechanism is now unifying some key elements scattered in the literature.

The sudden increase in the vortex diameter into a confused arrowhead shape flow, seen in figure 11(2), is called vortex breakdown or bursting. This event happens at the critical or minimum value of U_2/U_1, where U_2 is the external velocity and U_1 is the axial velocity in the vortex centreline. There are other explanations, such as a hydraulic jump by Benjamin (1962). In contrast, we find that spiralling precedes bursting which is not stated in Batchelor (1967), although spiralling and bursting are discussed separately.

Due to the presence of the restoring forces in the vertical direction, there are several possible mechanisms that could lead to a self-oscillation of the vortex tube and the generation of waves that travel along the vortex axis. The bubbles in the vortex tube are subjected to gravity, buoyancy forces and viscous resistance. If they are perturbed vertically, a damped self-oscillation can ensue about a neutral position. Other sources of self-oscillation can be coalescence and interactions between the bubbles. The bubbles can also bounce over the foil surface. Since the streamlines in the vortex tube are not spreading apart and the tube is largely remaining tube like, $Ro \to 0$. When a vortex line in the vortex tube is displaced radially due to the pressure gradient, the Coriolis forces will try to restore the displacement. As a result, a self-oscillation would ensue. The degree of freedom of the vortex tube is large because the number of bubbles is large. Hence, the bubble filled vortex tube will behave like a continuous medium. The oscillation of the vortex tube will manifest as many waves which will travel. However, the presence of the spirals and vortex bursting are evidence of resonant waves in the vortex tubes, which scale with the diameter of the vortex tube (Bandyopadhyay *et al.* 1992; Bandyopadhyay & Hellum 2014).

The Kelvin wave spiral (mode $m = 1$) appears along the 45° slope to U_{ext} when the vortex tube is stretched and the radial spread of the foil-tip vortex agglomeration is a maximum (figure SI-IA-8; the foil roll velocity $(\partial \phi/\partial t)$ reaches its maximum value). The increase in the centrifugal force destabilizes the balance with resistive viscous force and an oscillation in the vortex tube ensues creating the spiral.

3.10.2. *Modelling of chevrons of co-rotating vortex tubes*

Waves form past the stagnation points of vortex crossings in both types $(\pm\Gamma)$ and (Γ, Γ). In (Γ, Γ), we look for waves in the chevrons in figure 12 ahead of the vortex fusion. The chevron is spread apart further when the co-rotating tubes in figure 11 enter the adverse pressure gradient region of the foil. The spread out

FIGURE 12. Kelvin divergent wave model of a foil-tip chevron; $f = 1.25$ Hz. The model is empirical. A pair of co-rotating spiralling vortex tubes are coming from the pressure side of the foil tip. While being stretched at 45°, the combined vortex tube bursts into an arrowhead shape. This panel appears in between the panels in figure 11(1 and 2). Curved big arrow represents the bundle of streamlines of the rolled up flow of the foil tip. Regions of favourable and adverse pressure gradients are marked; x is along the foil chord, U_{ext} is the external flow velocity.

chevron, resisting fusing, is modelled below as experiencing trains of Kelvin divergent waves. This example is similar to what is briefly seen on the surface in figure SI-TA-1 also at $f = 1.25$ Hz. The chevron has symmetrical branches lying in a plane. This occurrence is consistent with that for $Ro \ll 1$, where the waves are planar and at an angle to the axis of rotation of the upstream vortex (Batchelor 1967). Assume that the stagnation point at the apex of the chevron and upstream of the burst vortex is translating along the 45° slope, producing a divergent wave train. Figure 12 shows a plausible empirical explanation that the plane waves divide symmetrically at angles of $\pm 19°$ to the upstream vortex axis. The agreement is good. The transverse waves being weak are not seen. The pressure point in the parlance of divergent waves (say, a sailboat is being dragged in a channel), or the stagnation point, also match.

We use the dispersion relationship $\lambda_g = 2\pi U^2 (\cos \theta)^2 / g$ to estimate the wavelength λ_g. The stagnation point moves at an estimated velocity of 0.14 m s^{-1}. For $\theta = 45°$,

$\lambda_g = 0.006$ m. This value is in agreement with figure 12. The pitch of the spirals is similar to λ_g. Independent verification of the hypothesis is required. The stretched aerated vortex line at 45° slope sustains waves and is elastic.

3.11. *Initial condition dependence: cycle-to-cycle concatenation*

Like equation (2.7), the sum of roll (τ_ϕ), pitch (τ_θ) and twist ($\tau_{\theta t}$) torques introduced is conserved cycle to cycle. If the sharp leading edge of the foil at its root penetrates the funnel, entrainment by the foil leading edge takes place. The funnel oscillates. The root vortex may spawn small funnels in the large funnel above it (figure 13c,d, SI, Movies 1 and 4). A concatenation model of this variation is given below.

The entrainment at the root (Ω_{root}) and the foil (Ω_{foil}) shown in figure SI-DA-4 are given by

$$\Omega_{root} = \operatorname{erf}(x) = \frac{2}{\sqrt{\pi}} \int_0^x e^{-t^2} \, dt, \quad \text{and} \tag{3.4}$$

$$\Omega_{foil} = \operatorname{erf} c(x) = 1 - \operatorname{erf}(x). \tag{3.5}$$

Here, t is time, and x is the surplus or deficiency in entrainment (mass or volume of air) from a long time average. In figure SI-DA-4, the total normalized entrainment of 1.0 is given by the applied torque.

Figure 13 shows vertical secondary DL and turbulent surface vortices on the lee side, translating horizontally. Figures 13(a) and 13(b) show that the funnel mouth, of diameter q, indicated by the dark spot on the free surface – an indentation on the surface – is small and translates with the air-entrained vortex below it, at a depth of p. Due to a pressure difference with the vortex core, the cusp of the tiny funnel sends air to the vortex through a very thin (invisible) tube. The elastic vortex is pinned between the unstable stagnation point below and the free surface as it pushes against the pressure gradient downwards. A leeward shear of the stagnation point buckles the vortex producing a standing Kelvin wave. A third mode of buckling – a two wavelength long dashed and dotted line – is fitted. Since $p \gg q$, the unstable elastic vortex has an abrupt drop in the diameter as in Kelvin mode $m = 0$. For $p \leqslant q$, there is nothing to buckle as in (d). The $m = 0$ mode does not undergo maximum stretching because it is not aligned to the direction of principal strain and is not active in the production of visible bubbles. In the turbulent case in figures 13(c) and 13(d), the funnel is wider. The funnel oscillations and the secondary surface vortices in the near wake control the apportioning of the air entrainment between the foil and the root vortex.

3.12. *Modelling of the modulus of elasticity of an aerated vortex*

Figure 10(a) shows a thin vortex with small amplitude waves, aligned with the centre of the funnel, later buckling to a sinusoid in (b) when stretching reaches the maximum level due to the mean vortex slope of 45°. Below, a buckling model of the modulus of elasticity E of the vertical elastic vortex tube, near the free surface in figure 13(a,b), is given. Added mass effects are ignored. The vortex length in (a) allows a spiral of two turns; see figure 3 in Bandyopadhyay & Gad-El-Hak (1996). Ignoring the spiralling, this is simplified to a planar buckling and aerated 'bar' of third mode. Two wavelengths lying between the stagnation point and the free surface (the dashed and dotted lines) can be fitted to the elastic vortex in (a).
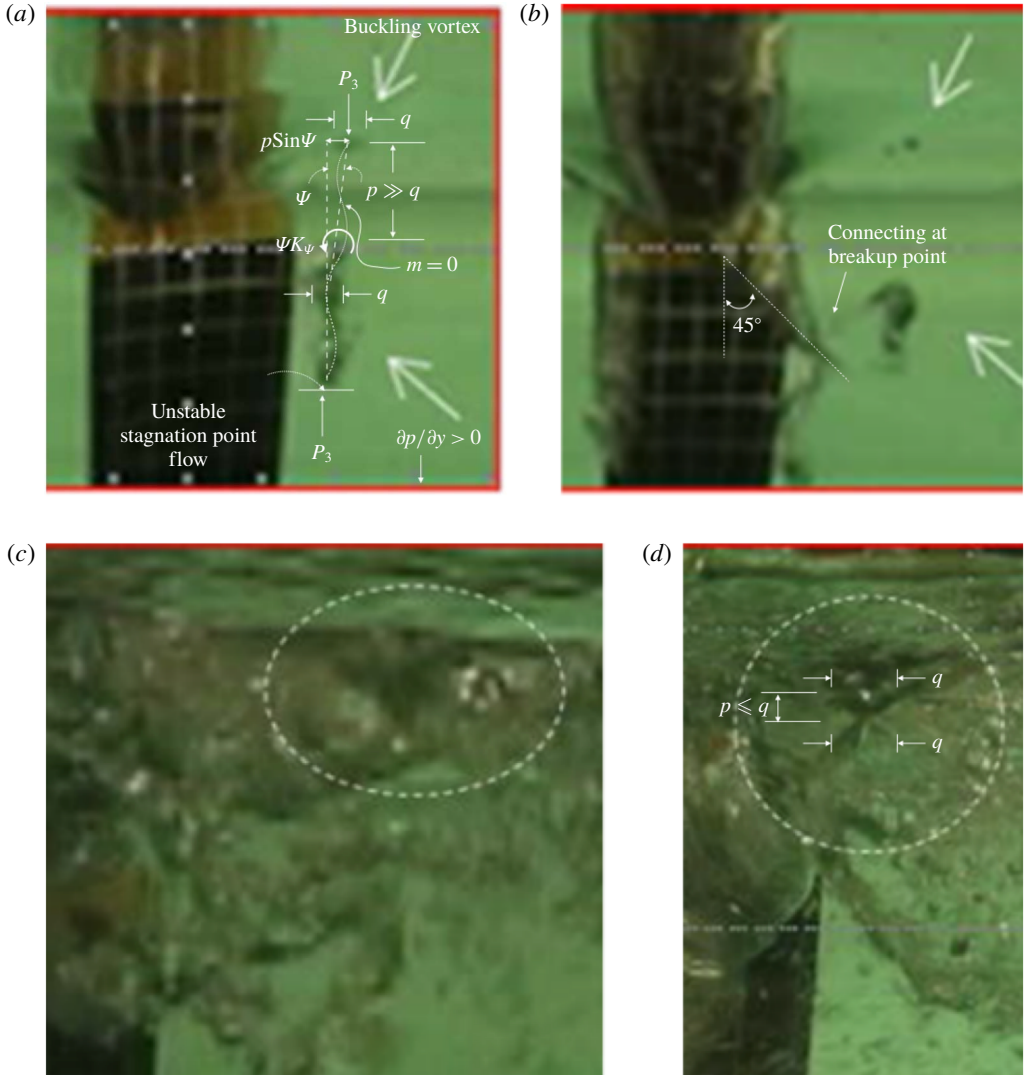
FIGURE 13. Time frames of lee-side air-entrained secondary surface vortices: 'laminar' (*a,b*) and turbulent (*c,d*). In (*a,b*), the upper arrow marks a surface indentation that is the funnel mouth of diameter *q*. This funnel translates down with the air-entrained vortex, as marked by the lower arrow, at a depth of *p*; $p \gg q$. The Kelvin mode $m = 0$ is formed, shown by the dotted line part (the upper wave of buckling). The vortex in (*a*) is a spiral of two turns (see figure 3 in Bandyopadhyay & Gad-El-Hak 1996). Ignoring the spiralling, this is simplified to a buckling aerated 'bar' of third mode. That is, a wave of two wavelengths lying between the stagnation point and the free surface (the dashed and dotted lines) can be fitted to the elastic vortex in (*a*). K_Ψ is torsional spring constant. In (*c,d*), the dashed perimeters enclose the turbulent secondary surface vortex; $p \leqslant q$ in (*d*). Coordinate *y* is downwards from the free surface; P_3 is axial load for the third mode of buckling.

The deflection of an elastic solid bar undergoing the third mode of buckling is given by $P_3 = 9\pi^2 EI/p^2$, where P_3 is axial load (N), and *p* is the length (m) $= 1.2c$, where *c* is the foil chord, and *I* is the second moment of area $= \pi(q/2)^4/4$. For critical

buckling, I should be from the minimum value of the diameter q (m). The value of the visible q varies from 0.01 m at the axial location where the deflection is zero to just under 0.02 m where the deflection is the maximum. Take $P_3 = \rho g p (\pi q^2/4)$ (N). Ignoring the reduction in the vortex diameter, $P_3 = 0.37$ (N) for $q = 0.02$ m, and $P_3 = 0.0924$ (N), for $q = 0.01$ m. For $P_3 = 0.37$ N, $E = 7.6 \times 10^3$ N m^{-2}. For $P_3 = 0.0924$ N, $E = 3.05 \times 10^4$ N m^{-2}. For comparison, E for gelatin gels is 1×10^3 N m^{-2} (Lucas *et al.* 2015), and for water, E is 2.2×10^9 N m^{-2}.

The above simplification holds for the lower wavelength since the axis remains vertical where the foil trailing edge effect is uniformly felt. For the upper wavelength, the foil trailing edge effect is less due to a foil truncation (figure 1*a*). There is a resistance of torsional spring constant K_Ψ due to the effects of the lower trailing edge vortex, and this applies at the lower boundary condition. See figure 13(*a*). A net lateral buckling displacement of $p \mathrm{Sin}\,\Psi$ is produced. Since Ψ is small, the critical value of the compression load is $P_{cr} = K_\Psi/p$. Assuming $P_{cr} = P_3 = 0.0924$ N, the estimated spring constant K_Ψ is 0.011 Nm rad^{-1}.

A force of 0.0924 N is 1/10th of the lowest load in air in a small flapping fin produced in our gearless hemispherical motor drive, which is the lowest-friction drive built by us (Bandyopadhyay 2019). Say, the root vortex in figure 6(*b*) oscillates axially 10 to 20 times while discharging bubbles in the unstable zone. Assume that such loss of energy due to release of compressed air in the form of bubbles is similar to the frictional losses in the flapping mechanism of flying insects, and that the number of natural damped oscillations in the spring–mass–damper system is equal to the quality factor Q. Then the Q of the damped oscillation of the bursting root vortex is similar to that of fruit fly, hawkmoth and bumblebee (Ellington 1999).

4. Discussion

Examples are shown of aerated vortices undergoing changes in cross-section near a free surface. Table 1 is a listing of the new vortex flows observed in the swirling surroundings. They show the breakup clearly where the double helix crosses near the apex and the jetting at the apex of the cone, as postulated by Saffman (1990). Kelvin mode of 1 is shown to be present; the presence of mode 0 is limited.

The root vortex is composed of contra-rotating vortices ($\pm\Gamma$) but the foil-tip vortex spiral is composed of co-rotating vortices (Γ, Γ). In the absence of a theory of instability explaining vortex bursting and bubble formation near a free surface, and to minimize the number of assumptions, a simplified overview is given. The flow has shear and an adverse pressure gradient. After formation, induced velocity cones down both vortices to a crossing. In the shear, both vortices are stretched causing turbulence and vorticity amplification until the maximum level is reached in the plane of principal strain. The vortex crossing causes the ($\pm\Gamma$)-type to break up reconnecting later, while the (Γ, Γ)-type is fused. Both types undergo Kelvin wave instabilities first of mode $m = 0$, followed by $m = 1$ spiralling. It is assumed that the uniform diameter 'vortex rod', and the abrupt diameter reductions in the ($\pm\Gamma$) type, as well as the straight section of fused vortex tube between the chevron and the $m = 1$ spiral in the (Γ, Γ)-type, represent the $m = 0$ waves. In both types after the $m = 1$ mode is formed, the entire vortex family stretched optimally bursts creating smaller scales. Extending Theodorsen's (1952) and Lundgren's (1982) theories relating structures to scales, the elements of the energy spectrum is present in the concatenating vortex instabilities.

(*a*) *Summary conditions of vortex bursting*: in the rotating flow near a free surface, several organized vortex structures with an air core are produced. Exhibiting elastic

properties, they buckle and sustain waves. The stretching and bursting properties are common whether the vortex structure is a double helix at the root or is a single spiral originating near the foil-tip boundary layer. After the formation, the progression of the DH root vortex to bursting is given by

$$\beta \rightarrow 45°, \quad \text{and} \tag{4.1}$$
$$C_{LV} \rightarrow 1.0. \tag{4.2}$$

The vortex bursts when these limits are crossed,

$$\beta = 45°, \quad \text{and} \tag{4.3}$$
$$C_{LV} = 1.0. \tag{4.4}$$

Strictly speaking, $C_{LV} = 1.0$ is due to both the root and the leading edge vortices. However, due to large span/chord, only one vortex is strong. Near the free surface, the leading edge contribution is smaller.

The stages of bursting observed can be compared with theory noting that: (a) the vorticity form of the Navier–Stokes equations gives the effect of stretching in shear and shows that vorticity becomes a maximum when the stretching is along the principal strain; and (b) bursting can be seen as vortex breaking, modelled by hyperbolic equations. When two vortex cores cross, the vortices break. Vortex breaking is seen only after the vortex has been maximally stretched. The effect of external strain is given by $r = \pi \alpha bh / \Gamma$ (equation (2.12), Saffman 1990), where b, h are minor and major axes of the elliptic cross-section of the vortex core, Γ is circulation at time t and α is a function of the initial geometry of the vortex and circulation Γ_o. The axial strain reaches a maximum value just before Γ becomes negligible. By then $A = bh$ drops by 75 %, causing the vortex breakup. In the present experiments, $\Gamma \approx 0$ and $A \approx 0$ when no bubble is seen locally along the vortex axis, and yet there are vortex lines and a blob aligned downstream. Our results are in agreement with the mechanisms of Saffman's model of vortex breakup in case of $(\pm \Gamma)$ type. In case of the (Γ, Γ) type, wave equation modelling is required. The following is a summary of the related aspects of the flow.

(i) Due to vorticity cancellation by viscosity, the DH breaks where the tapering opposite helix touch farthest from the root, creating a stagnation point, pressure build up and a swirling jet. By pulling in vorticity from the DH, the jet reconnects the breakup. The swirling jet is a vortex tube with a remarkably uniform diameter, and is horizontal, experiencing no stretching. The jet strikes the water, creating a spiralling vortex cone of Kelvin mode $m = 1$ of negative vorticity because it falls behind the rotation in the upstream swirling jet. The conical aerated vortex is stretched along multiple 45° slants while bursting.

(ii) Spatially separated from the root vortex, co-rotating vortex tubes of the rolled-up foil-tip flow spiral around one another over the foil. They also proceed along an inclination of $\beta = 45°$ to the vertical whereby the vorticity is stretched to the maximum extent. These vortex tubes fuse but do not break as in the co-rotating case. Over the adverse pressure gradient region of the foil, an $m = 1$ mode of negative vorticity is produced, but this vortex spiral is small and is of uniform diameter – not conical, as in the contra-rotating case. This small vortex spiral bursts simultaneously with the root vortex.

(iii) Pinned between the free surface and the breakup point, the DH spiral stands, appearing as stacks of Taylor tubes as in Taylor–Couette flows, although aerated. The

Taylor tubes are radially closed, albeit not with the wall boundary condition. This perspective contrasts with past Taylor–Couette experiments with solid cylinders.

(iv) The wavelengths of the bursting aerated vortex tubes are compared with the sound measurements in oceanic breaking waves.

(v) While coarse bubbles form in the root vortex away from the foil, fine bubbles form only in the foil boundary layer owing their origin to the instability of the contact interface.

(vi) Since the water is thermally stratified, an impulsive initiation of the foil pitching motion (not rolling) creates capillary waves induced by surface tension emanating radially from the surface piercing foil stem, with the number of rays increasing with time. Impulsive disturbances produce similar waves in stably stratified salt solutions of constant Brunt–Väisälä frequency. Here, the impulse is resolved into orthogonal waves.

(b) *Comparison of terminal spirals with large structures of turbulent boundary layer separation*: consider the similarities between the post-breakup vortex formation in figure 7(a) and the breakdown of the sublayer vorticity causing incipient separation in a nominally two-dimensional flat plate turbulent boundary layer (TBL) where a series of large structures (LSs) forms; each LS consists of several hairpin vortices. Both are adverse pressure gradient flows where $\omega \to 0$. The apex of the vortex cone is similar to the point of separation and the vortex cone is similar to the LSs of the separating TBL. Let x, y, z be the longitudinal, surface-normal and transverse distances in the wall over which the TBL is developing. The vorticity equation (1.1) can be simplified in the viscous sublayer of the nominally two-dimensional (0, 0, ω_z) flat plate TBL (Bandyopadhyay 1995). Here, ω_z is the transverse vorticity given as $\omega_z = -\partial U/\partial y$ where U is the longitudinal velocity. The velocity and vorticity gradients in the longitudinal and lateral directions are small compared to those in the surface-normal direction. The vorticity equation then simplifies to $(1/\rho)\partial p/\partial x + \nu \partial \omega_z/\partial y = 0$ which can be solved for ω_z if $\partial p/\partial x$ is measured at an instant of time. The equation shows that the longitudinal pressure gradient and vorticity in the normal direction are related near the wall ($y \to 0$) where there is a powerhouse of vorticity waiting to be ejected in the normal direction (Tritton 1989, p. 142; Lighthill 1963, p. 69). Measurements from closely spaced temporal wall-pressure sensors applied to the simplified vorticity equation show that in the boundary layers, the vorticity flux lines are inclined at a mean slope of $45° \pm 5°$ (Andreopolous & Agui 1996). The vorticity flux lines are similarly inclined in the conical vortices in figure 7 also. Extending the two-dimensional argument, the vortex cone, free to rotate in (x, r, ϕ), has a 3×3 matrix of torque and strain with a set of mutually perpendicular principal axes. A converse argument can also be made.

(c) *Comments on stretching*: in (Γ, Γ), maximum stretching along the principal strain direction, spiralling between tubes, merging and bursting are seen. However, vortex breaking is not seen in the rolled-up foil-tip flow and the bursting is not as catastrophic. Due to a lack of entrainment and bubble formation, the elastic energy is much lower. The bursting of aerated vortices can scatter more than bubble type does.

In the rare example in figure SI-IA-9 at $f = 1.25$ Hz, there are two DH root vortices: one DH is slanted at $45°$ and has Taylor tubes, as common for $f = 1.25$ Hz, but the other is at a shallower angle and has a DH without Taylor cells as seen at $f = 1$ Hz, exactly as in figure SI-IA-2. While the former bursts, the latter merely expands radially due to the loss of stretching. This behaviour may be due to a lack of lock-in. Only vortices experiencing maximum turbulence amplification broaden the energy spectrum.
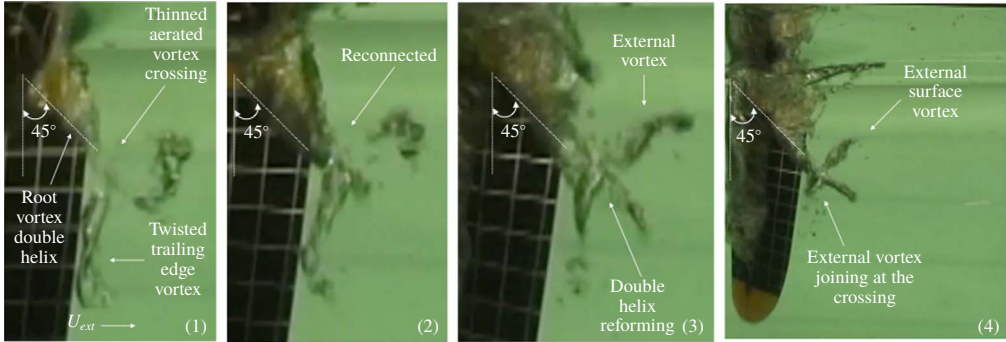
FIGURE 14. Example of preferred connection point of several aerated vortices in proximity in a relatively pristine surrounding at $f = 1.25$ Hz. The vortex undergoing maximum stretching, given by the 45° slope, is experiencing a breakup at the tip where the arms of the double helix with opposing circulations ($\pm\Gamma$) cross. This breakup point in panel 1 becomes the reconnection point later in panel 2. The neighbouring vortices fuse at this reconnection point as shown in panels 3 and 4. The aerated connection point manifold with multiple vortices is 0.01 m in diameter.

(d) *Preferred connection point of multiple vortices in proximity*: How would the vortices in proximity in figures 2 and 14 interact? Figure 14 shows an example at $f = 1.25$ Hz of vortices connecting at the same point (panel 4). Figure 2 shows two examples at $f = 1$ Hz both connecting at the breakup point. The initial free surface is flat. In figure 14 panel 1, there are three vortices: a DH root vortex, a twisted trailing edge vortex down below and a surface vortex on the right (unmarked) formed first (Movie 3). The vortices are formed in the same cycle. As per Kelvin's theorem, their circulation must have been connected to start with. The root vortex is undergoing maximum turbulence intensification because it is slanted at 45°. The root vortex is also undergoing breakup (panel 1) and reconnection (panel 2) near the apex where the arms of the DH ($\pm\omega$) must be crossing. Panels 3 and 4 show that all three vortices have fused at this breakup point of the most stretched vortex. Moreover, figure 2(3) shows that the connection takes place only at the vortex crossing points in each DH; even the stray vortex also meets there although disintegration into bubbles has taken place. As per Biot–Savart's law, vorticity intensification enlarges the induced velocity field to make this possible. The rule of vortex congregation and connection is as follows. In a random agglomeration of vortices in a swirling shear flow, the vortices will congregate near the vortex undergoing maximum stretching, fusing at the point where the crossing of opposing circulation is causing a breakup. Saffman's (1990) positive feedback loop accelerates this process.

(e) *Flow dimension*: examine the dimensions and the stability of the flow. Consider the Cartesian roll, pitch and yaw angles (ϕ, θ, ψ) as in figure 1, where the rate of separation of the neighbouring fluid motion trajectories is measured by the Lyapunov exponents (λ_ϕ, λ_θ, λ_ψ). Since $\theta_{bias} = 0°$ in the foil (equations (2.2) and (2.3)), there is no yawing motion (Menozzi *et al.* 2008) making $\lambda_\psi \leqslant 0$. The flow is stable in ψ. Hence the flow is low-dimensional. Compare the capillary waves due to (ϕ and θ) as in figure 1(*d*) and SI-TA-(2, 3). The fluid trajectories on the surface remain periodic in ϕ and do not grow, hence $\lambda_\phi = 0$. But they do grow in θ, hence $\lambda_\theta \nleqslant 0$. Figure SI-IA-9 shows two periodic aerated double helix vortex flows of different pitches co-existing

and growing simultaneously – uncommon occurrences. Hence the flow is chaotic in θ and $\lambda_\theta > 0$. The periodicity restricts the dimensions of the instabilities making the flow weakly nonlinear. The root vortex system has some dependence on initial condition but only in θ.

(f) *Breaking and reconnection time scales*: for the geometric parameters of initial vortex core radius and the radius of a ring vortex, equations (3.8) and (3.9) of Saffman (1990) give connection and rejoining times (T) as $\Gamma T = $ constant, where Γ is circulation. His model equations are hyperbolic (wave equations). Take the Kelvin wavelength λ, a property external to the aerated vortex core, as a length scale. Therefore, the vortex breaking and rejoining time scales can be modified non-dimensionally as $\Gamma T/\lambda^2 = $ constant.

In the foils flapping at f, the lift force L, and also for equivalent orthogonal oscillatory surface waves, $f^2 \propto L = \rho U \Gamma$, $\Gamma \propto f^2/U$, where ρ is density. Changing the constant of proportionality by multiplying by λ^3 to balance the dimension m^2 s^{-1}, $\Gamma \propto f^2 \lambda^3/U$. Therefore, equations (3.8) and (3.9) in Saffman (1990) represent Strouhal numbers writing $\Gamma T/\lambda^2 \propto (f^2 \lambda^3/U)(T/\lambda^2) = f\lambda/U = $ a constant if $fT = $ const. which relates the foil oscillation time scale with the time scales of vortex breaking and reconnection. With increasing f, T is lower, a correct trend.

At $f = 1$ Hz, the time for vortex breaking and rejoining is 0.13–0.26 s. This range is lower than in Schatzl's (1987) experiment on colliding ring vortices where it is (0.2 s + 0.4 s). This trend is in the right direction since the foil circulation is likely higher than the ring vortex circulation (Saffman 1990).

Saffman (1990) mentions the 'significant' discrepancy between his model and Kerr & Hussain's (1989) simulation on one hand, and Schatzl's (1987) measurements on the other. The former groups expected a doubling of the maximum vorticity during core merging, whereas the measurements obtained none. The vortex stretching until maximization that we observe prior to bursting would also lead to increase in vorticity in agreement with the former two groups.

(g) *Future work on vortex elasticity*: the Deborah number *De* measures the relative fluidity and elasticity of a medium – how Newtonian or non-Newtonian a medium is. Measuring the time scales of adjustment to applied stresses, define $De = t_c/t_p$, where t_c is the relaxation time and t_p is the time scale of the process. The value of *De* is low for fluids and high for solids. Pipe & Monkewitz (2005) have shown that the vortex shedding behind a cylinder is stabilized in a polymer solution even at very low *De*. Water temperature near 0 °C or addition of a polymer may affect the storage and release of elastic energy.

Evidence of spring–mass-like oscillation of aerated vortex tubes subjected to stretching and relaxation appears in figure 6(*d*), supported by equations (1.1) and (1.2). Evidence of buckling of aerated vortex has been given. If the vortex slope of 45° is a state of neutral equilibrium, then what nudges the vortex to the unstable zone of $\beta > 45°$? Figure 2(1,2) suggests that buckling is the nudge that tilts the vortex, tip first, to the unstable zone. In (1), initially, the buckling is in the stable zone. Here, the upper boundary condition has a torsional spring of constant κ_Ψ resisting the lateral buckling displacement $L_v \mathrm{Sin}(\Psi)$. Here L_v is the vortex length and Ψ is the angle subtended by the displacement at the root. For small Ψ, the critical compression for buckling is $P_c = P_{cr} = \kappa_\Psi/L_v$. The zig-zag buckling in (1) moves to the unstable zone of β in (2), bursting and developing into the Euler–Bernoulli mode 1 of cantilever beams.

The vortex in figure 6(*b*1) has aerated Taylor air tubes around the toroidal axis. Following Moore & Pullin (1998), if the vorticity of the Taylor tube is ω, density is ρ

and radial distance from the toroidal axis is r_c, then $\omega/(\rho r_c)$ is a constant. This ratio captures the countering effects of centrifugal force and the area reducing compressive effects of surface tension. Those authors remark: 'We know of no existence theorems relevant to transonic rotational flow with compact vorticity. The question of existence of this type of vortex flow for non-trivial boundary conditions remains an open question'. The present work does give the example of an aerated compact vortex with elastic properties that is kind of a Hill's vortex. During compaction and bursting, the aerated vortex probably does go locally sonic. High-speed schlieren video at $f \geqslant 1.25$ Hz may reveal the mechanism of vortex buckling, compaction and release of elastic energy.

Acknowledgements

Declaration of interests

The author reports no conflict of interest.

Supplementary material and movies

Supplementary material and movies are available at https://doi.org/10.1017/jfm.2019.1075 or, alternatively, at https://drive.google.com/drive/folders/1h8OBpE0W0wCMco9THfWmyUNpmnN168ND?usp=sharing.

REFERENCES

ADRIAN, R. J. & MARUSIC, I. 2012 Coherent structures in flow over hydraulic engineering surfaces. *J. Hydraul. Res.* **50** (5), 451–464.

ADRIAN, R. J., MEINHART, C. D. & TOMKINS, C. D. 2000 Vortex organization in the outer region of the turbulent boundary layer. *J. Fluid Mech.* **422**, 1–54.

AKILLI, H., SAHIN, B. & ROCKWELL, D. 2003 Control of vortex breakdown by a coaxial wire. *Phys. Fluids* **15** (1), 123–133.

ANDERECK, C. D., LIU, S. S. & SWINNEY, H. L. 1986 Flow regimes in a circular Couette system with independently rotating cylinders. *J. Fluid Mech.* **164**, 155–183.

ANDREOPOLOUS, J. & AGUI, J. 1996 Wall-vorticity flux dynamics in a two-dimensional turbulent boundary layer. *J. Fluid Mech.* **309**, 45–84.

BAKER, C. J. 1979 The laminar horseshoe vortex. *J. Fluid Mech.* **95** (2), 347–367.

BANDYOPADHYAY, P. R. 1980 Large structure with a characteristic upstream interface in turbulent boundary layers. *Phys. Fluids* **23** (11), 2326–2327.

BANDYOPADHYAY, P. R. 1986 Aspects of the equilibrium puff in transitional pipe flow. *J. Fluid Mech.* **163**, 439–458.

BANDYOPADHYAY, P. R. 1995 A low-dimensional model of an intermittently separating turbulent boundary layer. In *ASME Symp. on Separated and Complex Flows, FED*, vol. 217, pp. 75–82. American Society of Mechanical Engineers.

BANDYOPADHYAY, P. R. 2015 A novel large slosh-or-spin low-speed underwater propulsor bridges the unsteady and steady propulsion mechanisms of nature and engineering. *IEEE J. Ocean. Engng* **41** (4), 868–881.

BANDYOPADHYAY, P. R. 2016 Highly maneuverable biorobotic underwater vehicles – Part B: 11.1 Autonomous ocean vehicles, subsystems and control. In *Springer Handbook of Ocean Engineering* (ed. M. R. Dhanak & X. I. Nikolas), pp. 281–300. Springer.

BANDYOPADHYAY, P. R. 2019 A hemispherical motor oscillator for experiments on swimming and flying of small animals. *Trans ASME J. Fluids Engng* **141**, 021102.

BANDYOPADHYAY, P. R., BEAL, D. N., HRUBES, J. D. & MANGALAM, A. 2012 Relationship of roll and pitch oscillations in a fin of low aspect ratio and rounded leading edge flapping at transitional to high Reynolds numbers. *J. Fluid Mech.* **702**, 298–331.

BANDYOPADHYAY, P. R., BEAL, D. N. & MENOZZI, A. 2008a Biorobotic insights into how animals swim. *J. Expl Biol.* **211** (Pt 2), 206–214.

BANDYOPADHYAY, P. R. & GAD-EL-HAK, M. 1996 Rotating gas-liquid flows in finite cylinders: Sensitivity of standing vortices to end effects. *Exp. Fluids* **21**, 124.

BANDYOPADHYAY, P. R. & HELLUM, A. M. 2014 Modeling how shark and dolphin skin patterns control transitional wall-turbulence vorticity patterns using spatiotemporal phase reset mechanisms. *Sci. Rep.* **4** (1), 6650.

BANDYOPADHYAY, P. R. & LEINHOS, H. A. 2013 Propulsion efficiency of bodies appended with multiple flapping fins – when more is less. *Phys. Fluids* **25**, 041902.

BANDYOPADHYAY, P. R., LEINHOS, H. A. & HELLUM, A. M. 2013 Handedness helps homing in swimming and flying animals. *Sci. Rep.* **3**, 1128.

BANDYOPADHYAY, P. R., LEINHOS, H. A., HRUBES, J. D., TOPLOSKY, N. & HANSEN, J. 2011 Turning of a short-length cable using flapping fin propulsion. *IEEE J. Ocean. Engng* **36** (4), 571–585.

BANDYOPADHYAY, P. R., RIESTER, J. E. & ASH, R. L. 1992 Helical-perturbation device for cylinder-wing vortex generators. *AIAA J.* **30** (4), 988–992.

BANDYOPADHYAY, P. R., SINGH, S. N., THIVIERGE, D. P., ANNASWAMY, A. M., LEINHOS, H. A., FREDETTE, A. R. & BEAL, D. N. 2008b Synchronization of animal-inspired multiple fins in an underwater vehicle using olivo-cerebellar dynamics. *IEEE J. Ocean. Engng* **33** (4), 563–578.

BANDYOPADHYAY, P. R., STEAD, D. J. & ASH, R. L. 1991 Organized nature of a turbulent trailing vortex. *AIAA J.* **29** (10), 1627–1633.

BATCHELOR, G. K. 1967 *An Introduction to Fluid Dynamics*. Cambridge University Press.

BATCHELOR, G. K. & TOWNSEND, A. A. 1949 The nature of turbulent motion at large wave-numbers. *Proc. R. Soc. Lond.* A **199**, 238–255.

BEAL, D. N. & BANDYOPADHYAY, P. R. 2007 A harmonic model of hydrodynamic forces produced by a flapping fin. *Exp. Fluids* **43**, 675–682.

BENJAMIN, T. B. 1962 Theory of the vortex breakdown phenomenon. *J. Fluid Mech.* **14**, 593.

BILLANT, P., CHOMAZ, J. & HUERRE, P. 1998 Experimental study of vortex breakdown in swirling jets. *J. Fluid Mech.* **376**, 183–219.

BOERSMA, I. & WOOD, D. H. 1999 On the self-induction of a helical vortex. *J. Fluid Mech.* **384**, 263–279.

BOULTON-STONE, J. M. & BLAKE, J. R. 1993 Gas bubbles bursting at a free surface. *J. Fluid Mech.* **254**, 447–466.

BROWN, G. L. & LOPEZ, R. M. 1990 Axisymmetric vortex breakdown. Part 2. Physical mechanisms. *J. Fluid Mech.* **221**, 553–576.

CHONG, M. S., PERRY, A. E. & CANTWELL, B. J. 1990 A general classification of three-dimensional flow fields. *Phys. Fluids* **2** (5), 765.

COLES, D. 1965 Transition in circular Couette flow. *J. Fluid Mech.* **21**, 385–425.

CRAPPER, G. D. 1957 An exact solution for progressive capillary waves of arbitrary amplitude. *J. Fluid Mech.* **2** (6), 532–540.

CUYPERS, Y., MAUREL, A. & PETITJEANS, P. 2003 Vortex burst as a source of turbulence. *Phys. Rev. Lett.* **91** (19), 194502.

CURRIE, I. G. 1993 *Fundamental Mechanics of Fluids*, 2nd edn. McGraw-Hill.

DEANE, G. B. & STOKES, M. D. 2002 Scale dependence of bubble creation mechanisms in breaking waves. *Nature* **418**, 839–844.

EGGERS, J. 2001 Air entrainment through free-surface cusps. *Phys. Rev. Lett.* **86** (19), 4290–4293.

EINSTEIN, H. A. & LI, H. 1958 The viscous sublayer along a smooth boundary. *Trans. Am. Soc. Civil Engng* **123**, 293–313.

ELLINGTON, C. P. 1999 The novel aerodynamics of insect flight: applications to micro-air vehicles. *J. Expl Biol.* **202** (23), 3439–3448.

ESCUDIER, M. P. & ZEHNDER, N. 1982 Vortex-flow regimes. *J. Fluid Mech.* **115**, 105–121.

FALER, J. H. & LEIBOVICH, S. L. 1977 Disrupted states of vortex flow and vortex breakdown. *Phys. Fluids* **20** (9), 1385–1400.

FIEDLER, B. H. 2009 Suction vortices and spiral breakdown in numerical simulations of tornado-like vortices. *Atmos. Sci. Lett.* **10**, 109–114.

FUENTES, O. V. 2018 Motion of a helical vortex. *J. Fluid Mech.* **836**, R1.

FUSTER, D. & COLONIUS, T. 2011 Modelling bubble clusters in compressible liquids. *J. Fluid Mech.* **688**, 352–389.

GOLLUB, J. P. & SWEENY, H. L. 1975 Onset of turbulence in a rotating fluid. *Phys. Rev. Lett.* **35**, 927.

GORDON, J. L. 1970 Vortices at intakes. *Water Power* **22** (4), 137–138.

HABERMAN, W. L. & MORTON, R. K. 1953 An experimental investigation of the drag and shape of air bubbles rising in various liquids. *Report* 802, U.S. Navy Department: The David W. Taylor Model Basin.

HALL, M. G. 1972 Vortex breakdown. *Annu. Rev. Fluid Mech.* **4**, 195–218.

HAMA, F. R., LONG, J. D. & HEGARTY, J. C. 1957 On transition from laminar to turbulent flow. *J. Appl. Phys.* **28**, 388–394.

HEAD, M. R. & BANDYOPADHYAY, P. 1981 New aspects of turbulent boundary-layer structure. *J. Fluid Mech.* **107**, 297–338.

HERON, I. & MYOSE, R. Y. 2009 Delta wing vortex-burst behavior under a dynamic freestream. *J. Aircraft* **46** (5), 1500–1512.

HILL, M. G. 1977 Vortex breakdown. *Annu. Rev. Fluid Mech.* **4**, 195–218.

HITE, J. E. & MIH, W. C. 1994 Velocity of air-core vortices at hydraulic intakes. *J. Hydraul. Engng* **120** (3), 284–297.

HOPFINGER, E. J., BROWAND, F. K. & GAGNE, Y. 1982 Turbulence and waves in a rotating tank. *J. Fluid Mech.* **125**, 505–534.

HUGO, R. & VEER, C. 2003 An experimental investigation of vortex breakdown in multiphase pipe flow. In *33rd AIAA Fluid Dynamics Conference and Exhibit*. American Institute of Aeronautics and Astronautics.

HUMPHREYS, H. W., SIGURDSSON, G. & OWEN, J. H. 1970 Model test results of circular, square, and rectangular forms of drop-inlet entrance to closed-conduit spillways. Illinois State Water Survey, Urbana, *Rep. Investigation* 65.

JOUKOWSKY, N. E. 1912 Vihrevaja teorija grebnogo vinta. *Trudy Otd. Fiz. Nauk Mosk. Obshch. Lyub. Estest.* **16**, 1–31 (French translation in Théorie tourbillonnaire de l'hélice propulsive (Gauthier-Villars, Paris, 1929), 1–47).

KAZANTSEV, V. B., NEKORKIN, V. I., MAKARENKO, V. & LLINAS, R. 2004 Self-referential phase reset based on inferior olive oscillator dynamics. *Proc. Natl Acad. Sci. USA* **101** (52), 18183–18188.

KERR, R. M. & HUSSAIN, F. 1989 Simulation of vortex reconnection. *Physica* D **37**, 474–484.

KHALIL, H. K. 1996 *Nonlinear Systems*. Prentice-Hall.

KHOO, B. C., YEO, K. S., LIM, D. F. & HE, X. 1997 Vortex breakdown in an unconfined vortical flow. *Exp. Therm. Fluid Sci.* **14**, 131–148.

KLINE, S. J., REYNOLDS, W. C., SCHRAUB, F. A. & RUNSTADLER, P. W. 1967 The structure of turbulent boundary layers. *J. Fluid Mech.* **30**, 741–773.

KONNO, A., WAKABAYASHI, K., YAMAGUCHI, H., MAEDA, M., ISHII, N., SOEJIMA, S. & KIMURA, K. 2002 On the mechanism of the bursting phenomena of propeller tip vortex cavitation. *J. Mar. Sci. Technol.* **6**, 181–192.

KUO, A. Y.-S. & CORRSIN, S. 1971 Experiments on internal intermittency and fine-structure distribution functions in fully turbulent fluid. *J. Fluid Mech.* **50**, 285–319.

KWAY, J. H. L., LO, Y.-S. & CHAN, E.-S. 1998 Laboratory study of deep-water breaking waves. *Ocean Engng* **25** (8), 657–676.

LEIBOVICH, S. 1978 The structure of vortex breakdown. *Ann. Rev. Fluid Mech.* **10**, 211–240.

LEIBOVICH, S. 1984 Vortex stability and breakdown: survey and extension. *AIAA J.* **22**, 1192–1206.

LEPERCQ-BOST, E., GIORGI, M., ISAMBERT, A. & ARNAUD, C. 2008 Use of the capillary number for the prediction of droplet size in membrane emulsification. *J. Membr. Sci.* **314**, 76–89.

LIGHTHILL, M. J. 1963 Introduction (to) boundary layer theory. In *Laminar Boundary Layers* (ed. L. Rosenhead), pp. 46–113. Dover Publishers.

LIGHTHILL, M. J. 1978 *Waves in Fluids*. Cambridge University Press.

LUBIN, P. & GLOCKNER, S. 2015 Numerical simulations of three-dimensional plunging breaking waves: generation and evolution of aerated vortex filaments. *J. Fluid Mech.* **767**, 364–393.

LUCAS, M. C., MARÍA, S. F., PATRICIA, P. S., LAURA, M. F. & FASCE, A. 2015 Determination of elastic modulus of gelatin gels by indentation experiments. *Procedia Materials Sci.* **8**, 287–296.

LUCA-NEGRO, L. & O'DOHERTY, T. 2001 Vortex breakdown: a review. *Prog. Energy Combust. Sci.* **27** (4), 431–481.

LUGT, H. J. 1989 Vortex breakdown in atmospheric columnar vortices. *Bull. Am. Meteorol. Soc.* **70**, 1526–1537.

LUNDGREN, T. S. 1982 Strained spiral vortex model for turbulent fine structure. *Phys. Fluids* **25**, 2193.

MAHADEVAN, L., RYU, W. S. & SAMUEL, A. D. T. 1998 Fluid 'rope trick' investigated. *Nature* **392**, 140.

MEDWIN, H. & BEAKY, M. M. 1989 Bubble sources of the Knudsen sea noise spectrum. *J. Acoust. Soc. Am.* **83**, 1124–1130.

MEDWIN, H., NYSTUEN, J. A., JACOBUS, P. W., OSTWALD, L. H. & SNYDER, D. E. 1992 The anatomy of underwater rain noise. *J. Acoust. Soc. Am.* **92**, 1613–1623.

MENOZZI, A., LEINHOS, H., BEAL, D. N. & BANDYOPADHYAY, P. R. 2008 Open-loop control of a multi-fin biorobotic underwater vehicle. *IEEE J. Ocean. Engng* **33** (2), 59–68.

MISAKA, T., HOLZÄPFEL, F., HENNEMANN, I., GERZ, T., MANHART, M. & SCHWERTFIRM, F. 2012 Vortex bursting and tracer transport of a counter-rotating vortex pair. *Phys. Fluids* **24**, 025104.

MOET, H., LAPORTE, F., CHEVALIER, G. & POINSOT, T. 2005 Wave propagation in vortices and vortex bursting. *Phys. Fluids* **17** (5), 054109.

MOORE, D. W. & PULLIN, D. I. 1998 On steady compressible flows with compact vorticity; the compressible Hill's spherical vortex. *J. Fluid Mech.* **374**, 285–303.

MOWBRAY, D. E. 1967 The use of schlieren and shadowgraph techniques in the study of flow patterns in density stratified liquids. *J. Fluid Mech.* **27**, 595–608.

NOLAN, D. S. 2012 Three-dimensional instabilities in tornado-like vortices with secondary circulations. *J. Fluid Mech.* **711**, 61–100.

NYSTUEN, J. A. 2002 Using ambient sound to passively monitor sea surface processes. In *Keynote speech, Pan Ocean Remote Sensing Conference (PORSEC 2002), Bali, Indonesia 3–6 September 2002*, special vol. 9–14.

ODGAARD, A. J. 1986 Free-surface air core vortex. *ASCE J. Hydraul. Engng* **112**, 610–620.

PATERSON, O., WANG, B. & MAO, X. 2018 Coherent structures in the breakdown bubble of a vortex flow. *AIAA J.* **56** (5), 1812–1817.

PAULEY, R. L. & SNOW, J. T. 1988 On the kinematics and dynamics of the 18 July 1986 Minneapolis tornado. *Mon. Weath. Rev.* **116**, 2731–2736.

PECKHAM, D. H. & ATKINSON, S. A. 1957 Preliminary results of low speed wind tunnel tests on a Gothic wing of aspect ratio 1.0. Aero. Res. Counc. *Tech. Rep.* CP-508, TN no. Aero. 2504.

PERRY, A. E & CHONG, M. S. 1982 On the mechanism of wall turbulence. *J. Fluid Mech.* **119**, 173–217.

PERRY, A. E., LIM, T. T. & TEH, E. W. 1981 A visual study of turbulent spots. *J. Fluid Mech.* **104**, 387–405.

PHILLIPS, W. R. C. 1985 On vortex boundary layers. *Proc. R. Soc. Lond.* A **400**, 253–261.

PIERREHUMBERT, R. & WIDNALL, S. 1982 The two-dimensional and three-dimensional instabilities of a spatially periodic shear layer. *J. Fluid Mech.* **114**, 59–82.

PIPE, C. & MONKEWITZ, P. A. 2005 Experiments investigating the effects of fluid elasticity on laminar vortex shedding from a cylinder. EPFL Lausanne. doi:10.5075/epfl-thesis-3347.

PIQUET, J. & PATEL, V. C. 1999 Transverse curvature effects in turbulent boundary layer. *Prog. Aerosp. Sci.* **35** (7), 661–672.

POLHAMUS, E. C. 1966 A concept of the vortex lift of sharp-edge delta wings based on a leading-edge suction-analogy. *NASA Tech. Note* D-3767.

PROSPERETTI, A. 1988 Bubble-related ambient noise in the ocean. *J. Acoust. Soc. Am.* **84** (3), 1042–1054.

RAHM, L. 1953 Flow problems with respect to intakes and tunnels of Swedish hydroelectric power plants. Bulletin no. 36, Hydraulic Institute, Swedish Royal Institute of Technology, Stockholm.

ROTUNNO, R. 2013 The fluid dynamics of tornado. *Annu. Rev. Fluid Mech.* **45**, 59–84.

RUPPERT-FELSOT, J., FARGE, M. & PETITJEANS, P. 2009 Wavelet tools to study intermittency: application to vortex bursting. *J. Fluid Mech.* **636**, 427–453.

SAFFMAN, P. G. 1990 A model of vortex reconnection. *J. Fluid Mech.* **212**, 395–402.

SARPKAYA, T. 1971 On stationary and travelling vortex breakdowns. *J. Fluid Mech.* **45**, 545–559.

SARPKAYA, T. 1995 Vortex breakdown and turbulence. In *33rd Aerospace Sciences Meeting*. AIAA-95-0433. American Institute of Aeronautics and Astronautics.

SCHATZL, P. R. 1987 An experimental study of fusion of vortex rings. PhD thesis, California Institute of Technology, Pasadena, CA.

SIBULKIN, M. 1962 A note on the bathtub vortex. *J. Fluid Mech.* **14** (1), 21–24.

SMITS, A. J. & LIM, T. T. (Eds) 2012 *Flow Visualization: Techniques and Examples*, 2nd edn. World Scientific.

SPALL, R. E. & GATSKI, T. B. 1991 A computational study of the topology of vortex breakdown. *Proc. R. Soc. Lond.* A **435**, 321–337.

STEVENSON, T. N. 1968 Some two-dimensional internal waves in a stratified fluid. *J. Fluid Mech.* **33**, 715–720.

STOKES, G. G. 1880 *Mathematical and Physical Papers*, vol. 1. Cambridge University Press.

TALAIA, M. A. R. 2007 Terminal velocity of a bubble rise in a liquid column. *World Acad. Sci. Engng. Tech.* **28**, 264–268.

TAYLOR, G. I. 1923 Stability of a viscous liquid contained between two rotating cylinders. *Phil. Trans R. Soc. Lond.* A **223**, 289–343; Containing Papers of a Mathematical or Physical Character.

THEODORSEN, T. 1952 Mechanisms of turbulence. In *Proceedings of the 2nd Midwestern Conference on Fluid Mechanics, Ohio State University, Columbus, Ohio*. Ohio State University.

TOWNSEND, A. A. 1976 *The Structure of Turbulent Shear Flow*. Cambridge University Press.

TRAPP, R. J. 2000 A clarification of vortex breakdown and tornado genesis. *Mon. Weath. Rev.* **128**, 888–895.

TRICOCHE, X., GARTH, C., KINDLMANN, G., DEINES, E., SCHEUERMANN, G., RUETTEN, M. & HANSEN, C. 2004 Visualization of intricate flow structures for vortex breakdown analysis. In *IEEE Visualization '04 Proceedings*, pp. 187–194. Institute of Electrical and Electronics Engineers.

TRITTON, D. J. 1989 *Physical Fluid Dynamics*. Oxford Science Publications.

TSOY, M. A., SKRIPKIN, S. G., KUIBIN, P. A., SHTORK, S. I. & ALEKSEENKO, S. V. 2018 Kelvin waves on helical vortex tube in swirling flows. *IOP J. Phys.: Conf. Ser.* **980**, 012003.

WAKELING, J. M. & ELLINGTON, C. P. 1997 Dragonfly flight. III. Lift and power requirements. *J. Expl. Biol.* **200**, 583–600.

WERLE, H. 1984 On vortex bursting. *NASA-TM*-77587, NASA Technical Reports Server.

WERELEY, S. T. & LUEPTOW, R. M. 1999 Velocity field for Taylor–Couette flow with an axial flow. *Phys. Fluids* **11**, 3637–3649.

WHITE, F. M. 1994 *Fluid Mechanics*, 3rd edn. McGraw-Hill.

WU, X. & MOIN, P. 2009 Direct numerical simulation of turbulence in a nominally zero-pressure-gradient flat plate boundary layer. *J. Fluid Mech.* **630**, 5–41.

YAMADA, K. & SUZUKI, K. 2016 Dynamical system analysis on the onset of recirculating flow region associated with vortex breakdown. In *46th AIAA Fluid Dynamics Conference*. American Institute of Aeronautics and Astronautics.